Università degli Studi di Padova

Sede Amministrativa: Università degli Studi di Padova

Dipartimento Territorio e Sistemi Agro-Forestali

SCUOLA DI DOTTORATO DI RICERCA IN: Territorio, Ambiente, Risorse e Salute

XXVIII CICLO

PROCESSES SPACE-TIME VARIABILITY AND HYDROLOGICAL RESPONSE OF HEADWATER CATCHMENTS: ROLE OF RAINFALL, VEGETATION AND ANTECEDENT CONDITIONS

Direttore della Scuola: Ch.mo Prof. MARIO ARISTIDE LENZI

Supervisore: Ch.mo Prof. MARCO BORGA

Co-supervisore: Dott.ssa ILJA VAN MEERVELD

Dottorando: GIULIA ZUECCO

Dedicated to my family

TABLE OF CONTENTS

ABSTRACT 15

RIASSUNTO 17

1. INTRODUCTION 21

1.1. Objectives 23

1.2. Structure of the thesis 24

2. STATE OF THE ART 27

2.1. Temporal stability of soil moisture and throughfall patterns 27

2.2. Subsurface hillslope-stream connectivity 31

2.3. Hysteresis between hydrological variables at the runoff event timescale 35

3. STUDY AREAS AND MATERIALS AND METHODS 39

3.1. Analysis and modeling of soil moisture spatial variability 39

3.1.1. Soil moisture measurements at the plot scale in Grugliasco 39

3.1.2. Soil moisture dynamics model 40

3.2. Temporal stability of throughfall and soil moisture patterns 42

3.2.1. Study area: Ressi catchment 42

3.2.2. Throughfall measurements 45

3.2.3. Soil moisture measurements at the plot scale in Ressi catchment 48

3.2.4. Analysis of temporal stability of throughfall and soil moisture 49

3.2.5. Estimation of vegetation characteristics in the throughfall plot 50

3.2.6. Evaluation of the controls on temporal stability of near-surface soil moisture ... 51

3.3. Quantification of subsurface connectivity in five headwater catchments 57

3.4. Development of a hysteresis index for hydrological variables at the runoff event timescale 61

3.4.1. Development of the index 61

3.4.2. Instrumentation and datasets used to test the hysteresis index 64

4. ANALYSIS AND MODELING SOIL MOISTURE SPATIAL VARIABILITY AT THE PLOT SCALE 71

4.1. Observed soil moisture variability 71

4.2. Modeling soil moisture spatial variability 75

5. COMPARING TWO DIFFERENT TYPES OF THROUGHFALL COLLECTORS 81

6. ANALYSIS AND MODELING OF TEMPORAL STABILITY OF THROUGHFALL AND SOIL MOISTURE 87

6.1. Relation between throughfall and rainfall characteristics 87

6.2. Temporal stability of throughfall and relation with vegetation characteristics.....90
6.3. Variability of near-surface soil moisture data 92
6.4. Temporal stability of near-surface soil moisture.....95
6.5. Factors controlling the temporal stability of near-surface soil moisture patterns 97
7. COMPARING SUBSURFACE CONNECTIVITY IN FIVE HEADWATER CATCHMENTS 107
8. APPLICATION AND TESTING OF THE HYSTERESIS INDEX FOR HYDROLOGICAL VARIABLES AT THE RUNOFF EVENT TIMESCALE 117
8.1. Application to synthetic data.....117
8.2. Application to field data: identification of the different hysteretic relations 120
8.3. Temporal variability in the hysteretic relation between soil moisture and streamflow 121
8.4. Sensitivity to the temporal resolution of the data 124
8.5. Sensitivity to noise in the data.....126
8.6. Comparison with previous indices.....128
8.7. Potential use and limits of the hysteresis index 130
CONCLUSIONS 133
REFERENCES 137
List of publications 150
Author contributions and acknowledgements 151

LIST OF FIGURES

Fig. 1.2.1. Relation between spatial and temporal scales for various hydrological processes (modified from: Grayson and Blöschl, 2000). The red dashed rectangle indicates the temporal and spatial scales considered in the thesis. 25
Fig. 3.1.1. Map of the experimental site in Grugliasco. 40
Fig. 3.2.1. Map of Ressi catchment showing the location of the field measurements and the sampling locations. GW: groundwater; SW: soil water; SM: soil moisture. The location of Ressi catchment in Italy is shown in the inset. 43
Fig. 3.2.2. Outlet of the Ressi catchment. 44
Fig. 3.2.3. Location of the throughfall plot in Italy and the spatial distribution of the trees and the two types of throughfall collectors in the plot (BK: buckets; RG: rain gauges). 46
Fig. 3.2.4. Buckets and rain gauges installed in the experimental plot. 46
Fig. 3.2.5. Location of the trees in the throughfall plot. 47
Fig. 3.2.6. TDR probe used for the soil moisture measurements at the throughfall plot. 49
Fig. 3.2.7. Picture of the canopy above BK 13, taken with a 24 mm lens on 16/09/2013. 51
Fig. 3.2.8. Picture of the canopy above BK 13, taken with a fisheye lens on 19/06/2014. 51
Fig. 3.2.9. Cumulative frequency distributions of simulated saturated hydraulic conductivity with a mean of 50 mm/d and different values of standard deviation (logarithmic scale). 52
Fig. 3.2.10. Cumulative frequency distributions of simulated saturated hydraulic conductivity with a mean of 1600 mm/d and different values of standard deviation (logarithmic scale). . 53
Fig. 3.2.11. Example of ranked MRD of throughfall measured by buckets (all 24 sampling times were considered) with indication of the percentiles of the distribution. 55
Fig. 3.2.12. Relation between percentiles (i.e., 5th, 10th, 25th, 50th, 75th, 90th and 95th) of the observed and the simulated MRD distributions of throughfall. The simulated values shown in the plot are the averages obtained from 200 simulations, while the error bars represent the standard deviations. The black solid line represents the 1:1 line. 55
Fig. 3.2.13. Relation between percentiles (i.e., 5th, 10th, 25th, 50th, 75th, 90th and 95th) of the observed and the simulated SDRD distributions of throughfall. The simulated values shown in the plot are the averages obtained from 200 simulations, while the error bars represent the standard deviations. The black solid line represents the 1:1 line. 56
Fig. 3.3.1. Locations of the piezometers in the five catchments and directed graphs of piezometers-stream networks. 59
Fig. 3.4.1. Examples of hysteretic relations between streamflow and soil moisture representing the four main hysteresis classes where the dependent variable increases during an event (column *a*) and the main steps in the computation of the hysteresis index (columns *b*-*e*). The circles and diamonds in column *c* represent the selected points (u) delimiting the intervals of integration on the rising and the falling limb, respectively. The symbol colors change from yellow to dark red to cyan during a runoff event. The horizontal black line in column *e* represents $\Delta A = 0$. 64
Fig. 3.4.2. Location of Alta Val de La Mare, Ressi and Bridge Creek catchment in Italy. 65
Fig. 3.4.3. Normalized hysteretic loops between streamflow and soil moisture in the Ressi catchment (*a*: clockwise; *b*: anti-clockwise), depth to water table in a piezometer in the

Bridge Creek catchment (*c*: eight-shaped; *d*: anti-clockwise), δ^2H in the Ressi catchment (*e*: eight-shaped), and EC in the Alta Val de La Mare catchment (*f*: anti-clockwise). Values of $\Delta Amin$, $\Delta Amax$ and h are reported in Table 8.2.1. Circles and diamonds represent selected points delimiting the 0.05 intervals of integration on the rising and the falling curve, respectively. The symbol colors change from yellow to dark red to cyan during a runoff event. See Fig. 3.4.4 for the time series. 66
Fig. 3.4.4. Time series of streamflow, soil moisture (a, b), depth to water table (c, d), δ^2H of streamwater (e) and stream water EC (f) for the hysteretic loops shown in Fig. 3.4.3. 67
Fig. 4.1.1. Time series of spatial mean soil moisture, rainfall and potential evapotranspiration (PET). The purple line in the upper plot is the moving average of PET. 72
Fig. 4.1.2. Boxplots of the spatial mean soil moisture for 2006-2008. The statistics are reported for the meadow and the vineyard at both depths, for the growing season (April to September) and the dormant season (October to March). The boxes indicate the 25th and 75th percentile, the whiskers indicate the 10th and 90th percentile, the horizontal line within the box marks the median. 73
Fig. 4.1.3. Boxplots of the spatial standard deviation of soil moisture for 2006-2008. The statistics are reported for the meadow and the vineyard at both depths, for the growing season (April to September) and the dormant season (October to March). The boxes indicate the 25th and 75th percentile, the whiskers indicate the 10th and 90th percentile, the horizontal line within the box marks the median. 74
Fig. 4.1.4. Relation between the spatial mean soil moisture at 0-30 cm and at 0-60 cm depth.. 74
Fig. 4.1.5. Relation between the spatial mean soil moisture and the coefficient of variation..... 75
Fig. 4.2.1. Time series of rainfall and spatial mean soil moisture for the year 2008 for (a) meadow and (b) vineyard at 0-30 cm depth. 77
Fig. 4.2.2. Boxplots of the spatial mean soil moisture and standard deviation for the period June-September in 2008. The boxes indicate the 25th and 75th percentile, the whiskers indicate the 10th and 90th percentile, the horizontal line within the box marks the median and the dash line marks the mean. 78
Fig. 5.2. The relation between gross rainfall and optimum sample size computed for buckets (BK) and rain gauges (RG). 83
Fig. 5.3. The relation between gross rainfall and the difference between standard errors (SE) of throughfall measured by the buckets (BK) and rain gauges (RG) (*a* and *d*) and the relation between the standard deviation (*b* and *e*) and interquartile range (*c* and *f*) of throughfall measured by the buckets (BK) and the rain gauges (RG). The measured throughfall is expressed as amount (mm) (*a*-*c*) and as a fraction of precipitation (%) (*d*-*f*). A negative difference indicates larger standard errors for rain gauges than for buckets. Symbols represent different event size classes; the pink solid line represents the 1:1 line (*b*, *c*, *e* and *f*). 84
Fig. 6.1.1. Relation between gross rainfall and throughfall spatial mean. The red dashed line represents the mean throughfall computed for 24 measurements using the buckets, while the error bars are the standard errors. 87
Fig. 6.1.2. Relation between mean rainfall intensity and throughfall spatial mean computed for 24 measurements using buckets. The error bars represent the standard errors. 88

Fig. 6.1.3. Relation between gross rainfall and spatial coefficient of variation of throughfall.....89
Fig. 6.1.4. Frequency of buckets with throughfall amount > 105% and < 65% for each sampling date, in relation to gross rainfall and mean rainfall intensity. 90
Fig. 6.2.1. Time series of throughfall spatial mean and correlation coefficients between pairs of throughfall sampling times. 91
Fig. 6.2.2. Ranked MRD of throughfall measured by buckets (all 24 sampling times were considered). Error bars are SDRD computed for each sampling site, the red solid line represents MRD = 0. 91
Fig. 6.3.1. Time series of spatial mean soil moisture at 0-7 and 0-12 cm depth, rainfall and potential evapotranspiration (PET). 93
Fig. 6.3.2. Relation between the spatial mean soil moisture at 0-7 cm and at 0-12 cm depth....93
Fig. 6.3.3. Relation between the spatial mean soil moisture and the coefficient of variation. at 0-7 cm and at 0-12 cm depth.....94
Fig. 6.4.1. Time series of soil moisture spatial mean at 0-7 and 0-12 cm depth and correlation coefficients between pairs of soil moisture sampling times. 95
Fig. 6.4.2. Ranked MRD of soil moisture measured at 0-7 and 0-12 cm depth. Error bars are SDRD computed for each sampling site, the red solid line represents MRD = 0. 96
Fig. 6.5.1. Relation between percentiles (i.e., 5th, 10th, 25th, 50th, 75th, 90th and 95th) of the observed and the simulated MRD distributions of post rainfall event soil moisture at 0-7 cm. The simulated values shown in the plot are the averages obtained from 200 simulations, while the error bars represent the standard deviations. The black solid line represents the 1:1 line. The vegetation was simulated as spatially homogeneous, while the mean ks was 200 mm/d and σks was 0.2.....98
Fig. 6.5.2. Relation between percentiles (i.e., 5th, 10th, 25th, 50th, 75th, 90th and 95th) of the observed and the simulated SDRD distributions of post rainfall event soil moisture at 0-7 cm. The simulated values shown in the plot are the averages obtained from 200 simulations, while the error bars represent the standard deviations. The black solid line represents the 1:1 line. The vegetation was simulated as spatially homogeneous, while the mean ks was 200 mm/d and σks was 0.2.....99
Fig. 6.5.3. Frequency of the Spearman correlation coefficients computed between the simulated MRD distributions of throughfall and post rainfall event soil moisture measured at 0-7 cm depth. The red vertical line represents the observed correlation. The vegetation was simulated as spatially homogeneous, while the mean ks was 200 mm/d and σks was 0.2. .99
Fig. 6.5.4. Frequency of the Spearman correlation coefficients computed between the simulated SDRD distributions of throughfall and post rainfall event soil moisture measured at 0-7 cm depth. The red vertical line represents the observed correlation. The vegetation was simulated as spatially homogeneous, while the mean ks was 200 mm/d and σks was 0.2.100
Fig. 6.5.5. Relation between percentiles (i.e., 5th, 10th, 25th, 50th, 75th, 90th and 95th) of the observed and the simulated MRD distributions of post rainfall event soil moisture at 0-7 cm. The simulated values shown in the plot are the averages obtained from 200 simulations, while the error bars represent the standard deviations. The black solid line represents the 1:1 line. The vegetation was simulated as spatially heterogeneous and correlated with ks, the mean ks was 400 mm/d and σks was 0.8. 101

Fig. 6.5.6. Relation between percentiles (i.e., 5th, 10th, 25th, 50th, 75th, 90th and 95th) of the observed and the simulated SDRD distributions of post rainfall event soil moisture at 0-7 cm. The simulated values shown in the plot are the averages obtained from 200 simulations, while the error bars represent the standard deviations. The black solid line represents the 1:1 line. The vegetation was simulated as spatially heterogeneous and correlated with ks, the mean ks was 400 mm/d and σks was 0.8. 101
Fig. 6.5.7. Frequency of the Spearman correlation coefficients computed between the simulated MRD distributions of throughfall and post rainfall event soil moisture measured at 0-7 cm depth. The red vertical line represents the observed correlation. The vegetation was simulated as spatially heterogeneous and correlated with ks, the mean ks was 400 mm/d and σks was 0.8. 102
Fig. 6.5.8. Frequency of the Spearman correlation coefficients computed between the simulated MRD distributions of throughfall and post rainfall event soil moisture measured at 0-7 cm depth. The red vertical line represents the observed correlation. The vegetation was simulated as spatially heterogeneous and correlated with ks, the mean ks was 400 mm/d and σks was 0.8. 102
Fig. 6.5.9. Relation between the median of 200 Spearman correlation coefficients, computed between the simulated MRD of throughfall and soil moisture at 0-7 cm depth, and the standard deviation of ks (σks). Colors of the dots were grouped by the mean ks. The red solid line represents the value of the observed Spearman correlation coefficient computed between the MRD of throughfall and soil moisture at 0-7 cm depth. The vegetation was simulated as spatially homogeneous. 103
Fig. 6.5.10. Relation between the median of 200 Spearman correlation coefficients, computed between the simulated MRD of throughfall and soil moisture at 0-7 cm depth, and the standard deviation of ks (σks). Colors of the dots were grouped by the mean ks. The red solid line represents the value of the observed Spearman correlation coefficient computed between the MRD of throughfall and soil moisture at 0-7 cm depth. The vegetation was simulated as spatially heterogeneous. 104
Fig. 6.5.11. Relation between the median of 200 Spearman correlation coefficients, computed between the simulated MRD of throughfall and soil moisture at 0-7 cm depth, and the standard deviation of ks (σks). Colors of the dots were grouped by the mean ks. The red solid line represents the value of the observed Spearman correlation coefficient computed between the MRD of throughfall and soil moisture at 0-7 cm depth. The vegetation was simulated as spatially heterogeneous and correlated with ks. 105
Fig. 7.1. Time series of rainfall, streamflow and subsurface connectivity (area-weighted) for BCC. Green dots represent time steps during which gatekeepers control connectivity. 107
Fig. 7.2. Relation between connectivity (area-weighted) and streamflow during rainfall-runoff events (red dots: rising limb of the hydrograph; blue dots: falling limb of the hydrograph). 108
Fig. 7.3. Frequency distribution of the hysteresis classes for the five catchments. 109
Fig. 7.4. Relation between sum of rainfall amount and antecedent precipitation in the previous two days (P+AP2) and maximum connectivity and between P+AP2 and stormflow of rainfall-runoff events. 111

Fig. 7.5. Relation between maximum connectivity and stormflow of rainfall-runoff events.....112
Fig. 7.6. Frequency of total time that a piezometer was active in BCC, LCC, C1, C2 and C3 catchment.....113
Fig. 7.7. Frequency of total time that a piezometer was connected to the stream in BCC, LCC, C1, C2 and C3 catchment.....114
Fig. 8.3.1. Values of the hysteresis index (h) computed for the streamflow-soil moisture relations at four different locations (SM1: riparian zone; SM2: footslope; SM3: midslope; SM4: upper hillslope) in the Ressi catchment. The horizontal black line represents the threshold between mainly clockwise (> 0) and anti-clockwise (< 0) loops. Shaded bars indicate eight-shaped or complex loops. 122
Fig. 8.3.2. The hysteresis classes for the 30 rainfall-runoff events for the relation between streamflow and soil moisture at four different locations along the riparian-hillslope transect in Ressi (SM1: riparian zone; SM2: footslope; SM3: midslope; SM4: upper hillslope; I = clockwise loop; II = eight-shaped or complex loop with a predominant clockwise loop; III = eight-shaped or complex loop with a predominant anti-clockwise loop; IV = anti-clockwise loop).....123
Fig. 8.3.3. Relation between the value of the hysteresis index (h) for the relation between streamflow and soil moisture and ASI+P for the different locations along the riparian-hillslope transect at the Ressi catchment. The horizontal black line represents the threshold between the mainly clockwise (> 0) and anti-clockwise (< 0) loops. 124
Fig. 8.5.1. Simulated and observed values of h for the relation between streamflow and soil moisture at the midslope (SM3 location) at Ressi catchment for the 30 studied rainfall-runoff events. Random instrumental noise was simulated 1000 times with a scaling factor of 1% (left) and 5% (right). The dots represent the median of the 1000 simulations, the error bars the interquartile range. 127

LIST OF TABLES

Table 3.2.1. Characteristics of rainfall events for the 21 throughfall measurements considered for the comparison of the two types of throughfall collectors. 48
Table 3.2.2. Mean and standard deviation values of logarithmic ks used in the simulations. 53
Table 3.2.3. Parameter values used in the simulations. 54
Table 3.3.1. Main characteristics of the catchments. 58
Table 3.3.2. Main characteristics of the connectivity network in the five catchments. 60
Table 3.4.1. The eight main hysteresis classes for independent variables that increase from the initial state, reach a peak and then decrease, with the corresponding minimum ($\Delta Amin$) and maximum ($\Delta Amax$) values of the difference between the integrals $\Delta Ai,j$ (equation (3.4.5)) and their sum, h. 62
Table 4.1.1. Summary of soil moisture statistics over the two land uses for 2006-2008 (only common sampling times are considered). 71
Table 4.2.1. Indexes of performance between observed and simulated mean soil moisture data. NS: Nash-Sutcliffe efficiency index; RMSE: Root Mean Square Error. 76
Table 4.2.2. Parameter values used in the simulation. 76
Table 4.2.3. Summary of soil moisture statistics over the two land uses (0-30 cm depth) for 2006-2008. 78
Table 6.2.1. Spearman correlation coefficients computed for the relation between MRD and SDRD and vegetation characteristics (Section 3.2.5). 92
Table 7.1. Significant Spearman rank correlation coefficients ($p < 0.05$) computed between stormflow and maximum connectivity and characteristics of the rainfall-runoff events. 110
Table 7.2. Significant Spearman rank correlation coefficients ($p < 0.05$) computed between the frequency of total time during which piezometers were responding and topographic characteristics of piezometers and significant Spearman rank correlation coefficients computed between the frequency of total time during which piezometers were connected to the stream and topographic characteristics of piezometers. 115
Table 8.1.1. Synthetic loops with a different area (A, B, C) and direction (clockwise: black solid line and loop name in black; anti-clockwise: red dashed line and loop name in red) used for testing the hysteresis indices and the corresponding values of h (equation 3.4.6), the H index developed by Langlois et al. (2005), the $HImid$ and $HImean$indices of Lawler et al. (2006), and the HI index of Aich et al. (2014). 118
Table 8.1.2. The synthetic eight-shaped loops used for testing the hysteresis indices with the values of h, the index developed by Langlois et al. (2005), H, the indices developed by Lawler et al. (2006), $HImid$, and its modified version $HImean$, and the index of Aich et al. (2014), HI. The arrows indicate the starting points of the loops: for values of x close to 0 on the rising limb, the black solid loops have larger values of y compared to the red dashed loops. 119
Table 8.2.1. Independent and dependent variables, sign of the dependent variable, hysteresis classes (see Table 3.4.1), and values of $\Delta Amin$, $\Delta Amax$ and h for the examples shown in Fig. 3.4.3. 120

Table 8.2.2. Values for H (Langlois et al., 2005), $HImid$ (Lawler et al. (2006) and HI (Aich et al., 2014) with notes about the interpretation of the direction of hysteretic loops for the examples shown in Fig. 3.4.3. The indices were applied without additional conditional statements or normalizations of the data. The values for $\Delta Amin$, $\Delta Amax$ and h are shown in Table 8.2.1. 121

Table 8.4.1. Frequency of the 30 rainfall-runoff events belonging to the four hysteresis classes (I-IV) for the observed data (columns) and for data with a 10- (*a*), 15- (*b*), 20- (*c*) and 30-min (*d*) temporal resolution (rows). The inner squares show the percentage of loops from a certain class that were reclassified to that class when the temporal resolution of the data was changed. For instance, 83.3% of the type III loops based on the original 5-minute data were still characterized as a type III loop when using 10-minute, 15-minute or 20-minute data (panel a, b and c, respectively), while 16.7% of the type III loops were reclassified as a type II loop using 10-minute, 15-minute or 20-minute data (panel a, b and c, respectively). See Table 3.4.1 for the definition of hysteresis classes. 126

Table 8.5.1. Frequency of the hysteresis classes (I-IV) for the 1000 simulations with noisy data for each rainfall event (left: 1% scaling factor; right: 5% scaling factor). Gray squares represent the hysteresis class for the observed data, bold values indicate the most frequently assigned hysteresis class with the noisy data for each rainfall event. See Table 3.4.1 for the definition of the hysteresis classes.....128

ABSTRACT

This thesis aims to enhance the understanding of the hydrological functioning of headwater catchments by focusing on *i)* how rainfall patterns controls spatial and temporal variability of soil moisture, and *ii)* how the soil moisture variability provide a control to the catchment response.

A first analysis of the spatial variability of soil moisture was carried out for data at 0-30 and 0-60 cm depth collected on a plot in Grugliasco (Po Plain, Northern Italy), characterized by two land uses (meadow and vineyard). Results showed that the differences in spatial mean and variability of soil moisture for the meadow and the vineyard are likely due to the different vegetation cover. Evaluation of the main physical controls on the spatial mean and the variability of soil moisture was carried out by using a simple bucket model. The model was calibrated by using spatial mean soil moisture and it had a relatively good prediction capability. The model was also shown to be able to capture the main differences between the two sites in terms of spatial variability of soil moisture.

The spatial and temporal variability of soil moisture was also analyzed in relation to throughfall spatial patterns in plot on a forested hillslope in the Italian pre-Alps. Throughfall was measured using two types of throughfall collectors: buckets and rain gauges. The collectors differed in size, number and spatial arrangement. Results showed that buckets and rain gauges measured similar throughfall amounts during rainfall events. However, findings indicate that different collectors can lead to differences in the quantified spatial variability of throughfall and presence of local clusters and outliers.

Near-surface soil moisture was measured upslope of each bucket, at 0-7 and 0-12 cm depth before and after rainfall events. Throughfall and soil moisture spatial patterns were not significantly or only weakly correlated, likely due to the lateral and vertical redistribution of water in the soil profile during the 2-36 hour period between the end of the rainfall event and the start of the soil moisture measurements. The temporal stability of soil moisture was larger than the temporal stability of throughfall and they were also not significantly correlated. The patterns of temporal stability were also not related to canopy characteristics (i.e., canopy openness and leaf area index). The application of the simple bucket model revealed that a large spatial variability in saturated hydraulic conductivity that is correlated with the spatial variability in leaf area index and root fraction weaken the correlation between throughfall and soil moisture patterns. The analysis of field data combined with the model application suggests

that in this specific forested hillslope the spatial organization of soil moisture is dominated by a combination of soil properties and vegetation characteristics, rather than by the throughfall spatial patterns.

Saturation at the soil-bedrock interface or the rise of shallow groundwater into more permeable soil layers results in subsurface stormflow and can lead to hillslope-stream connectivity. Networks of spatially-distributed piezometers in five small headwater catchments in the Italian Dolomites and the Swiss pre-Alps were used to quantify and compare the spatial and temporal variability of subsurface connectivity and its relation to streamflow dynamics. Results showed that the time that piezometers were connected to the stream was significantly correlated to the topographic wetness index, for two Swiss pre-alpine catchments, or to the distance to the nearest stream, for the dolomitic catchment with the largest riparian zone. During rainfall events, mainly anti-clockwise hysteretic relations between streamflow and the area that was connected to the stream were observed. Threshold-like relations between maximum connectivity and total stormflow and between maximum connectivity and the sum of total rainfall plus antecedent rainfall were more evident for the dolomitic catchments, where the riparian zone is characterized by a groundwater table near the soil surface. These preliminary results suggest that the delayed increase in subsurface connectivity relative to streamflow is likely not affected by the presence of a riparian zone. However, further analyses are needed to determine if morphology of the catchments affect the observed relations between subsurface connectivity and total stormflow.

Finally, this thesis attempted to develop an index for the quantification of hysteretic loops between hydrological variables at the runoff event timescale. The index provides information on the direction, the shape and the extent of the loop. The index was tested with synthetic data and field data from experimental catchments in Northern Italy. Hysteretic relations between streamflow and soil moisture, depth to water table, isotopic composition and electrical conductivity of stream water were correctly identified and quantified by the index. The sensitivity of the index to the temporal resolution of the measurements and measurement errors was also tested. The index can successfully quantify hysteresis, except for very noisy data or when the temporal resolution of the measurements is not well suited to study hysteresis between the variables. Overall, this metric can be used to test if models reproduce temporal variability in hysteresis or to compare hydrological responses in different catchments or at different spatial scales.

RIASSUNTO

Questa tesi ha lo scopo di migliorare la comprensione del funzionamento idrologico di bacini di testata analizzando *i)* come la precipitazione controlli la variabilità spaziale e temporale dell'umidità del suolo e *ii)* come quest'ultima a sua volta eserciti un controllo sulla risposta idrologica di bacino.

Una prima analisi della variabilità spaziale dell'umidità del suolo è stata effettuata su dati raccolti a 0-30 e 0-60 cm di profondità in una griglia sperimentale presso Grugliasco (Provincia di Torino), caratterizzata da due diversi usi del suolo (prato e vigneto). I risultati hanno evidenziato che le differenze nella media e nella variabilità spaziale dell'umidità del suolo sono probabilmente dovute alla diversa copertura vegetazionale su prato e su vigneto. Un semplice modello a serbatoio (*bucket*) è stato usato per valutare i fattori principali che controllano l'umidità media del suolo. Il modello, calibrato sulle serie temporali di umidità media, ha dimostrato una relativamente buona capacità predittiva. Inoltre, il modello è stato in grado di rappresentare le differenze principali nella variabilità spaziale dell'umidità del suolo dei due usi del suolo.

La variabilità spaziale e temporale dell'umidità del suolo è stata analizzata anche in relazione con i campi spaziali di precipitazione sottochioma determinati in una griglia sperimentale presso un versante forestato delle Prealpi Vicentine. La precipitazione sottochioma è stata misurata con due tipi di campionatori volumetrici di tipo manuale: secchi e pluviometri totalizzatori. I campionatori differivano per numerosità, superficie di campionamento e distribuzione spaziale. Questo confronto metodologico ha evidenziato che secchi e pluviometri totalizzatori misurano quantità simili di precipitazione sottochioma. Nonostante ciò, i risultati indicano che esistono delle differenze nella variabilità spaziale e nella determinazione di *clusters* e *outliers* di precipitazione sottochioma da parte dei due tipi di campionatori.
L'umidità del suolo è stata misurata a 0-7 e 0-12 cm di profondità, poco a monte di ciascun secchio, prima e dopo gli eventi piovosi. I campi spaziali di precipitazione sottochioma e umidità del suolo sono risultati poco o per nulla statisticamente significativi, probabilmente a causa della redistribuzione laterale e in profondità dell'acqua nelle 2-36 ore comprese tra la fine dell'evento piovoso e l'inizio dei campionamenti dell'umidità del suolo. È stata osservata una maggiore stabilità temporale dell'umidità rispetto alla precipitazione sottochioma e anche in questo caso la correlazione è risultata non significativa. La copertura delle chiome e l'indice di area fogliare non sono risultate correlate con la stabilità temporale della precipitazione

sottochioma. L'applicazione del modello a serbatoio ha mostrato che un'elevata variabilità spaziale della conducibilità idraulica a saturazione in correlazione con l'indice di area fogliare e la frazione di radici nel profilo di suolo tende a far diminuire la correlazione tra campi spaziali della precipitazione sottochioma e dell'umidità del suolo. I risultati ottenuti con l'integrazione dell'analisi dei dati osservati con l'applicazione modellistica fanno ipotizzare che, in questo specifico versante forestato, l'organizzazione spaziale dell'umidità sia dominata da una combinazione delle proprietà del suolo e delle caratteristiche vegetazionali piuttosto che dai campi spaziali della precipitazione.

Il deflusso sottosuperficiale è in genere innescato dallo sviluppo di una zona satura presso l'interfaccia suolo-roccia madre o dalla risalita della falda effimera in orizzonti di suolo più permeabili. Lo sviluppo di deflusso sottosuperficiale condiziona, quindi, la connettività versante-torrente. Reti di piezometri spazialmente distribuiti in cinque bacini nelle Dolomiti e nelle Prealpi Svizzere sono state usate per quantificare e confrontare la variabilità spazio-temporale della connettività sottosuperficiale e la sua relazione con i deflussi alla sezione di chiusura. I risultati hanno evidenziato che il tempo totale durante il quale i piezometri erano connessi con il torrente è risultato significativamente correlato con l'indice topografico di saturazione, in due bacini svizzeri, o con la distanza minima dal corso d'acqua, nel caso del bacino dolomitico con l'area riparia più estesa. Durante gli eventi afflussi-deflussi sono state rilevate relazioni isteretiche principalmente antiorarie tra il deflusso alla sezione di chiusura e la superficie del bacino connessa con il torrente. Inoltre, relazioni a soglia più marcate sono state osservate tra connettività massima e deflusso diretto e tra connettività massima e somma della precipitazione totale con quella dei giorni antecedenti, per i due bacini dolomitici, caratterizzati da livelli di falda nella zona riparia più vicini alla superficie del suolo. Questi risultati preliminari indicano che un ritardo nell'aumento della connettività rispetto all'incremento dei deflussi non è probabilmente riconducibile alla presenza di una zona riparia. Nonostante ciò, ulteriori analisi sono necessarie per stabilire se la morfologia dei bacini condizioni le relazioni tra connettività sottosuperficiale e deflussi alla sezione di chiusura.

Infine, in questa tesi è stato proposto un indice per la quantificazione dell'isteresi tra variabili idrologiche a scala di evento afflusso-deflusso. L'indice fornisce informazioni sulla direzione, la forma e l'area dell'isteresi. Test sull'indice sono stati eseguiti con dati sia sintetici che osservati da bacini sperimentali nell'Italia Settentrionale. Le relazioni isteretiche tra portata e umidità del suolo, livello di falda, composizione isotopica e conducibilità elettrica dell'acqua di torrente

sono state correttamente identificate e quantificate dall'indice. Inoltre, sono stati effettuati test di sensibilità alla risoluzione temporale e agli errori di misurazione. L'indice ha quantificato l'isteresi in modo soddisfacente, tranne in presenza di dati affetti da rumore o quando la risoluzione temporale delle misurazioni non è risultata accettabile per lo studio dell'isteresi. Nel complesso, l'indice qui proposto può essere adottato per valutare la capacità dei modelli idrologici di identificare la variabilità temporale dell'isteresi o per confrontare la risposta idrologica di bacini differenti o a diverse scale spaziali.

1. INTRODUCTION

Every catchment has its own distinct fingerprint or set of characteristics. The interactions between structural characteristics, such as topography, geology, soil and vegetation, greatly influence how a catchment responds to the driving forces (rainfall, snowmelt and evapotranspiration). Understanding the controls on the hydrological response is fundamental to elucidate and make predictions on floods, erosion and sedimentation processes and dispersion of nutrients and pollutants. Furthermore, improving our knowledge of catchment hydrology allows for a better identification of the effects of climate, anthropogenic and natural geomorphic changes on the catchment hydrological behavior. Assessing the relation between the hydrological response and the factors controlling it, as well as the identification of similarities in runoff generation mechanisms and the structural attributes of different catchments, are also important to predict the response of ungauged catchments to the hydrometeorological forces.

The comprehension of the hydrological behavior is possible because catchments are organized systems (e.g., Dooge, 1986) and are not governed by random processes (Sivapalan, 2005). However, our knowledge is still limited because the level of heterogeneity in catchment properties determines process variability at different spatial and temporal scales (McDonnell et al., 2007; Tetzlaff et al., 2008). The observed heterogeneity is due to the variability in spatial and temporal patterns (i.e., observations reflecting the level of organization of hydrological systems). While patterns can be detected by accurate measurements, measuring or inferring hydrological processes (i.e., the interactions between different properties of a system) and functions (i.e., the mechanisms from which patterns and processes emanate) (Sivapalan, 2005) has proven to be a more difficult task. The need to overcome studies on small-scale variability to understand catchment dominant processes has led hydrologists to formulate a unified theory (Sivapalan, 2005; McDonnell et al., 2007) based on the examination of patterns, processes and function. McDonnell et al. (2007) and Sivapalan (2005) pointed out that advances in catchment hydrology studies will be possible by insightful analyses of process complexity, the understanding of catchment function and the exploration of the underlying principles connecting patterns and processes with function.

In catchment hydrology, understanding the variations in water storage in the unsaturated and saturated zone is fundamental for the interpretation and prediction of runoff generation in

relation with the hydrometeorological forcing. In this context, soil moisture and groundwater represent the key variables for the comprehension of the hydrological response of a catchment. Soil moisture plays a major role in controlling the partitioning of water and energy fluxes at the ground surface and is the physical linkage between soil, climate and vegetation (Albertson and Montaldo, 2003; Rodríguez-Iturbe and Porporato, 2004). Moreover, soil moisture controls infiltration (Bronstert and Bárdossy, 1999; Raats, 2001), vegetation dynamics (Porporato et al., 2004), flood formation processes (Borga et al., 2007) and water distribution by feedback mechanisms between land surface and atmosphere (Koster et al., 2004). Soil moisture is characterized by a large variability in space and time: at the small scale this variability is controlled by topography, soil and vegetation properties, while at the large scale spatial and temporal patterns of soil moisture are driven by precipitation and evapotranspiration (Entin et al., 2000). The study of the spatial and temporal variability of soil moisture at the small scale (plot, hillslope or small catchment) is of particular interest because it improves our understanding of how the structural attributes, such as topography, soil type and permeability and vegetation, influence infiltration processes and lateral redistribution of soil moisture.

At the catchment scale the relation between soil moisture and runoff generation is strongly non-linear (e.g., Tromp-van Meerveld and McDonnell, 2005; James and Roulet, 2007; Penna et al., 2011) and, particularly, hysteretic relations have been found between streamflow and soil moisture at the rainfall-runoff event timescale. This non-linearity is associated with the catchment state (antecedent wetness conditions) and the magnitude of rainfall events. During dry conditions, soil moisture is characterized by a spatial disorganization (large spatial variability) led by local controls, while the storm runoff is rather small compared to wet conditions. Much larger volumes of runoff can be observed during wet conditions and are usually linked to highly-organized patterns of soil moisture, which are due to the influence of non-local control factors (e.g., upslope contributing areas) and the development of lateral soil water fluxes (Ali and Roy, 2009). This non-linear relation between soil moisture and runoff generation is assumed to be a consequence of the different level of hydrological connectivity of a catchment. The analysis of non-linear behaviors and their controls can lead to a better understanding of the mechanisms which link patterns to hydrological processes.

The analysis of the variability in soil moisture patterns is one of the most popular approaches for the investigation of hydrological connectivity (e.g., Western et al., 2001, 2005; Tromp-van Meerveld and McDonnell, 2005; James and Roulet, 2007). Recently, approaches based on the

study of groundwater variations were used to infer the processes underlying the development of subsurface connections between different areas of a catchment (e.g., Tromp-van Meerveld, 2006a and b). Subsurface connectivity between different portions of a catchment (e.g., hillslopes-riparian zone-stream) results from the development of saturation above less permeable layers (e.g., soil-bedrock interface) or when groundwater rises into more permeable soil layers, causing lateral water flow reaching the stream network. However, determining subsurface hillslope-stream connectivity and the investigation of its spatial and temporal variability and its relation with runoff generation mechanisms are difficult tasks because the water flow occurs in the subsurface. Common methods for the investigation of surface and subsurface connectivity are based on the retrieval of multiple measurements of the same variable at different locations and sampling times. Bracken et al. (2013) remarked that these multiple snapshots are good to study the structural connectivity and identify potential local controls, but often the focus of many studies is not based on the attempt to capture the processes responsible for hydrological connectivity. This means that hydrological research should develop towards measurements aiming to understand processes underlying the response of catchments rather than focusing only on the extreme small-scale heterogeneity of the patterns (McDonnell et al., 2007).

1.1. Objectives

This thesis aims to enhance the understanding of the hydrological functioning of headwater catchments by focusing on *i)* how rainfall patterns controls spatial and temporal variability of soil moisture, and *ii)* how the soil moisture variability provide a control to the catchment response. The main objective is developed into five specific objectives:

1. Analysis of the spatial and temporal variability of soil moisture at the plot scale for two different types of land use (meadow and vineyard), and assessment of the capability of a dynamic model to explain the soil moisture variability and the effect of land use.
2. Assessment of the difference in throughfall amount and spatial variability for two types of collectors at the plot scale for a forested hillslope.
3. Analysis of the influence of throughfall spatial patterns on near-surface soil moisture, by investigating the relation between the spatial patterns of throughfall and near-surface soil moisture at the plot scale for a forested hillslope, and the comparison of the temporal stability of throughfall and soil moisture.

4. Quantification of the spatial and temporal variability of subsurface connectivity in five headwater catchments and assessment of the relation between streamflow dynamics and connectivity.
5. Development of an index to characterize hysteresis between hydrological variables at the runoff event timescale.

1.2. Structure of the thesis

The thesis is divided into seven main sections, in addition to this first introductory chapter. Section 2 presents an updated literature review on *i)* the temporal stability of soil moisture and throughfall patterns, *ii)* subsurface hillslope-stream connectivity and *iii)* the hysteresis between hydrological variables at the runoff event timescale. Section 3 describes the study areas and the materials and methods. In Sections 4-8 the results and findings of the individual studies are discussed. The analysis of the spatial variability of soil moisture and the capability of a simple model to simulate the time series of the spatial mean and standard deviation of soil moisture for two sites with different land use is evaluated and discussed in Section 4. Section 5 focuses on the quantification of throughfall and the difference in the spatial variability obtained by the two types of collectors. Section 6 describes the analysis and modeling of the temporal stability of throughfall and near-surface soil moisture. Section 7 focuses on the main controls on subsurface connectivity in five headwater catchments. Finally, Section 8 presents the application of the hysteresis index to synthetic and field data and the sensitivity analysis of the hysteresis index.

The processes were investigated at the typical spatial and temporal scales for experimental catchment hydrology (Fig. 1.2.1). The spatial scales range from the plot scale to the hillslope and small catchment scale (< 1 km^2), while the temporal scales range from minutes, to hours (duration of rainfall-runoff events) to a few years. The influence of sampling methods on capturing the real spatial and temporal variability is also considered in the comparison of two different types of throughfall collectors and the sensitivity analysis of the hysteresis index to temporal resolution and noise in the data.

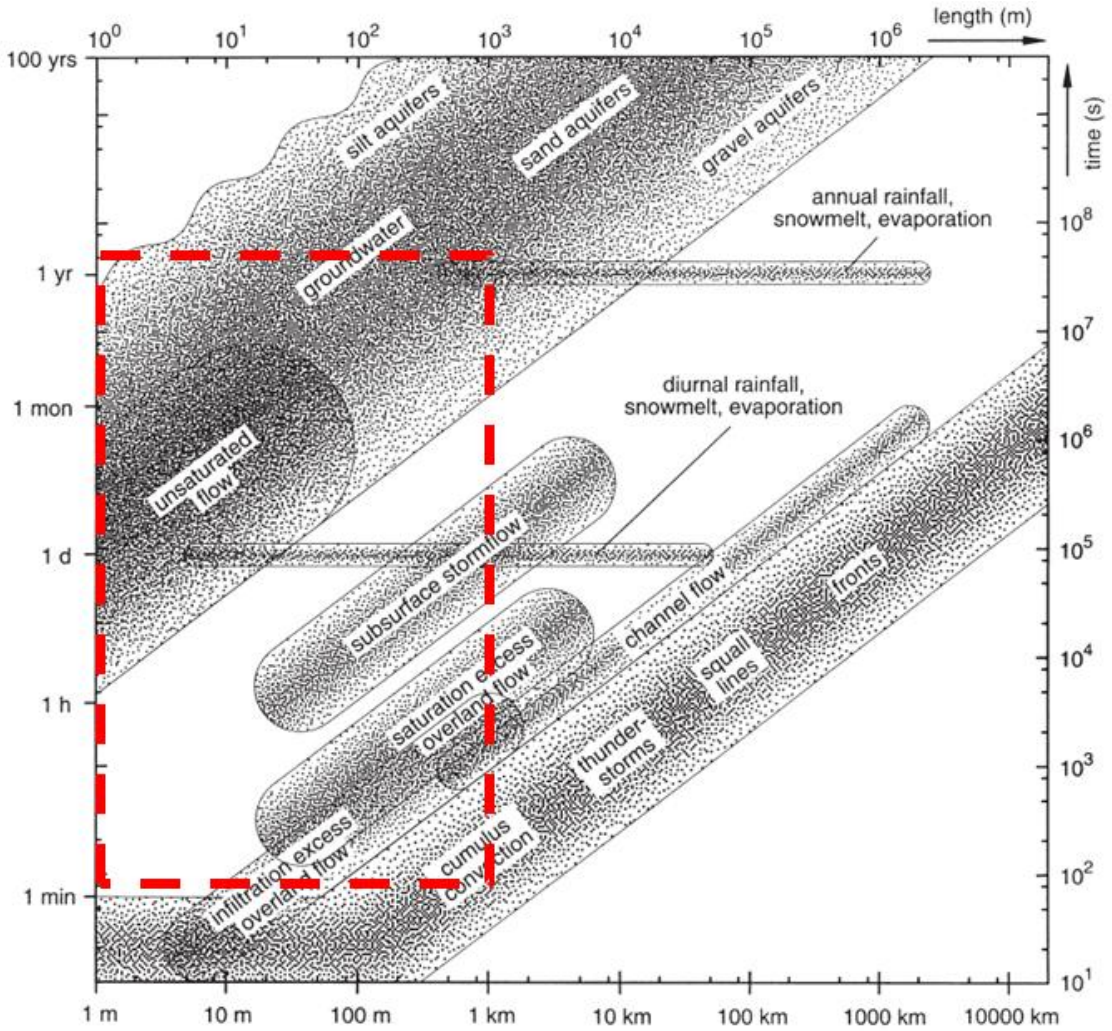

Fig. 1.2.1. Relation between spatial and temporal scales for various hydrological processes (modified from: Grayson and Blöschl, 2000). The red dashed rectangle indicates the temporal and spatial scales considered in the thesis.

2. STATE OF THE ART

2.1. Temporal stability of soil moisture and throughfall patterns

Soil moisture is a key variable controlling water and energy fluxes at different spatio-temporal scales (Robinson et al., 2008; Vereecken et al., 2008). Soil moisture plays an important role in climate dynamics from the regional to the global scale by controlling the exchange and partitioning of water and energy fluxes at the land surface. Agricultural and irrigation management practices largely depend on a timely and accurate characterization of temporal and spatial soil moisture dynamics in the root zone at the field scale. Soil moisture plays a major role in the organization of natural ecosystems and biodiversity (Vereecken et al., 2008), flood formation (Borga et al., 2007; Norbiato et al., 2009; Brocca et al., 2010), hillslope erosion (Cotler and Ortega-Larrocea, 2006) and soil-plant interaction (Laio et al., 2001; Rodríguez-Iturbe et al., 2001). Because a thorough comprehension of these hydrological processes requires the interpretation of soil moisture patterns, numerous studies focused on the spatial and temporal variability of soil moisture across different scales (Albertson and Montaldo, 2003; Famiglietti et al., 2008; Penna et al., 2009; Brocca et al., 2007, 2010).

Temporal stability is a well known concept in hydrology, and especially in studies focusing on spatial and temporal patterns of soil moisture. Vachaud et al. (1985) introduced the concept of temporal stability and defined it as “the time-invariant association between spatial location and classical statistical parameters of a given soil property”. They found that specific locations within a field represented the field averaged soil moisture, while other locations were consistently wetter or dryer than the average. This means that soil moisture at each sampling site varied over time, but that the relative spatial organization of soil moisture was preserved. Temporal stability of soil moisture has been reported for different scales: from the plot (e.g., Pachepsky et al., 2005; Herbst et al., 2009) to the hillslope (e.g., Penna et al., 2013) to the regional scale (e.g., Martínez-Fernández and Ceballos, 2003). Vanderlinden et al. (2012) showed that the concept of temporal stability is useful for finding the most time stable sampling locations (e.g., Vachaud et al., 1985; Kachanoski and de Jong, 1988), up- and downscaling soil moisture measurements (e.g., Cosh et al., 2004; Jacobs et al., 2004) and replacing missing data in a dataset (e.g., Pachepsky et al., 2005). Furthermore, temporal stability has been used in hydrological modeling (Brocca et al., 2009) and for assimilation of soil moisture monitoring data for soil water flow modeling (Pan et al., 2012).

There are two groups of methods for the computation of temporal stability (Vanderlinden et al., 2012). The first group of methods uses all measurements during the sampling period. These

methods include mean relative differences (MRD) and time independent spatial patterns (EOF analysis). The second group of methods uses pairs of observation times and includes the Spearman rank correlation, the Pearson correlation and the temporal persistence regression.

The mean relative differences (Vachaud et al., 1985) is a rank stability method and is the most used technique for the assessment of temporal stability. The description of the method and the equations can be found in Section 3.2.4.

Empirical orthogonal function (EOF) analysis, known also as principal component analysis (PCA), is a statistical method used for the analysis of large and multidimensional datasets and for the search of patterns. EOF analysis has been applied to soil moisture datasets (e.g., Perry and Niemann, 2007) to partition the variation into time-invariant spatial patterns (EOFs).

Regression and correlation analysis (Pearson correlation and Spearman rank correlation) focus on the "memory" in spatial soil moisture patterns by comparing pairs of observation times. These methods are weaker than the mean relative differences and EOF analysis because the correlation coefficient and slope and intercept of the regression may change as the pairs of observation times change. However, these methods are useful in characterizing observations in which the spatially stable pattern is different for different periods within the total sampling period (Vanderlinden et al., 2012).

Temporal stability is also used to find representative locations within a sampling area. Representative locations are defined as sites where measured soil moisture is close to the average or can be easily transformed to obtain the averaged soil moisture. Grayson and Western (1998) called these locations "catchment average soil moisture monitoring (CASMM) sites". The easiest method to define the representative location is the MRD. However, the concept of MRD alone does not consider the error represented by SDRD (the standard deviation of relative differences). Some authors, therefore, proposed to combine MRD and SDRD in a root mean square error (Jacobs et al., 2004; Zhao et al., 2010) or in the mean absolute bias error (MABE; Hu et al., 2010).

Recently, a further advancement in the analysis of the spatial variability and the temporal stability of soil moisture was presented by Mittelbach and Seneviratne (2012). They decomposed the spatial variance of absolute soil moisture over time in contributions from the spatial variance of mean soil moisture at all sites (which is a time-invariant term) and components varying over time that are related to soil moisture dynamics. This study showed that the time-invariant term is the largest contributor to the overall variability of soil moisture. The spatial variance of the temporal anomalies, which is related to soil moisture dynamics and

is relevant for climate and hydrological applications, contributes only a small fraction to total variance. They also showed that the concept of temporal stability introduced by Vachaud et al. (1985) mostly characterizes the time-invariant patterns (Mittelbach and Seneviratne, 2012).

The identification of the locations that are time-stable and most representative of the mean soil moisture (CASMM sites) is important to reduce the number of measurements and to compare soil moisture measured at the plot or small catchment scale with soil moisture derived by remote sensing data. Thus, research has been focusing on the controls of spatial patterns and temporal stability of soil moisture. Although some studies found that the CASMM sites have average vegetation and soil properties (e.g., Vachaud et al., 1985; Hupet and Vanclooster, 2004; Starr, 2005), there are other studies reporting that the effective controlling factors were not identified or were relatively unclear (e.g., Mohanty and Skaggs, 2001; Lin, 2006; Guber et al., 2008). Zhao et al. (2010) focused on the temporal stability of soil moisture patterns to identify the local controls of the most representative sampling points in a semi-arid steppe ecosystem in China. They collected field measurements in four plots with different grazing intensities and found that soil moisture was more stable during wet conditions than during dry or moist conditions. Zhao et al. (2010) also showed that the temporal persistence of spatial patterns of soil moisture varied with grazing intensity, and that soil texture, organic carbon and bulk density influenced the temporal stability in two plots, while vegetation and topographic properties were less important factors.

Martinez et al. (2013) quantified and elucidated the effects of several local controls on the temporal stability of soil moisture by simulating the flow of water with the HYDRUS model for sandy loam, loam and clay soils with different variability in the saturated hydraulic conductivity and different land cover (i.e., bare land and grassland). They found that spatial variability in saturated hydraulic conductivity determines the variability in MRD and that the magnitude of the variability in MRD depended on soil depth and soil texture (i.e., topsoil and coarser textures displayed larger variability in MRD than deeper soil layers and clay soils). On the contrary, root water uptake tended to decrease the variability of MRD in the root zone, while the variability in MRD increased in the soil layer below the root zone.

The concept of temporal stability has also been applied to studies focusing on the spatial and temporal patterns of throughfall, which can have important effects on the spatial patterns of soil moisture (Coenders-Gerrits et al., 2013). Keim et al. (2005) focused on the persistence of throughfall patterns, but modified the method developed by Vachaud et al. (1985) for the

computation of temporal stability. The computation of the relative differences neglects the variance of the sampling points and therefore extreme values of throughfall have a potential large effect on the spatially averaged throughfall. Keim et al. (2005) proposed to standardize throughfall based on the spatial mean and standard deviation computed for each sampling time. Then, the sampling locations were ranked based on their standardized throughfall. Keim et al. (2005) found that patterns of throughfall can be described by variograms and time stability plots of normalized throughfall. They also showed that the forest stand and the season affect the temporal persistence of throughfall, but that the spatial patterns could not be predicted *a priori* from tree locations.

Zimmermann et al. (2008) proposed an additional change to the modified mean relative differences method of Keim et al. (2005) for the analysis of temporal stability of throughfall patterns. To account for the frequent non-normal distribution of throughfall, Zimmermann et al. (2008) replaced the spatial mean and standard deviation of throughfall with the spatial median and the median absolute deviation to compute the standardized throughfall. They applied their analysis of temporal stability to spatial patterns of throughfall and solute deposition in a tropical rain forest and found that throughfall patterns were less stable during the early wet season compared to the later season. These results suggested that rapid plant growth at the beginning of the rainy season resulted in a lower stability of throughfall patterns, whereas less vegetative activity might affect the higher persistence of locations characterized by large and small throughfall amounts (Zimmermann et al., 2008).

Despite the large number of studies discussing the temporal stability of soil moisture and the studies focusing on the spatial variability and the temporal persistence of throughfall patterns, only a limited number of studies aimed to investigate the correlation between throughfall and soil moisture patterns (e.g., Raat et al., 2002; Shachnovich et al., 2008) and to identify the role of local controls and/or rainfall characteristics on these correlations (e.g., Coenders-Gerrits et al., 2013; Klos et al., 2014). It is still unclear how the interaction of soil properties and vegetation characteristics may increase or decrease the stability of soil moisture patterns and weaken the correlation between the MRD of throughfall and soil moisture.

2.2. Subsurface hillslope-stream connectivity

Connectivity describes the condition by which elements of a landscape become connected or are connected by a flow of energy, water, matter or organisms. In hydrology, connectivity is usually referred to as the linkage of separate areas of a catchment by surface (overland flow) and/or subsurface water flow (Blume and van Meerveld, 2015). The connections between different elements of a catchment develop as a result of water volume, rate of transfer (Bracken et al., 2013) and antecedent wetness conditions. Inputs of water are represented by rainfall, snow- and ice-melt, while interception, evaporation, transpiration, infiltration and transmission determine losses in the water volume. The rate of water movement between areas of the catchments depends on flow resistance and pathways, which depend on topography, soil type and their permeability, soil depth, presence of macropores and bedrock permeability.

Although there is an increasing interest in hydrological connectivity, several review articles reported the lack of a common definition of the term (e.g., Bracken and Croke, 2007; Tetzlaff et al., 2007; Turnbull et al., 2008; Ali and Roy, 2009; Lexartza-Artza and Wainwright, 2009; Michaelides and Chappell, 2009; Bracken et al., 2013; Blume and van Meerveld, 2015). Ali and Roy (2009) distinguished four types of definitions for hydrological connectivity based on *i)* components of the water cycle, *ii)* landscape features, *iii)* spatial patterns of hydrological properties, and *iv)* flow processes. Definitions based on components of the hydrological cycle (e.g., Pringle, 2003) and landscape features (e.g., Stieglitz et al. 2003; Lane et al., 2004; Bracken and Croke, 2007; Tetzlaff et al., 2007) are scale-independent and do not make assumptions about the processes involved and the resulting patterns (Ali and Roy, 2009). On the other hand, definitions associated with spatial patterns (e.g., Western et al., 2001; Knudby and Carrera, 2005) and flow processes (Hornberger et al., 1994; Vidon and Hill, 2004; Ocampo et al., 2006) focus on specific landscape elements, such as hillslopes. Bracken and Croke (2007) and Turnbull et al. (2008) distinguished two types of hydrological connectivity: static or structural, and dynamic or functional. Structural connectivity refers to the spatial patterns in the landscape, such as soil-moisture connectivity (e.g., James and Roulet, 2007) and terrain connectivity, which influence the movement of water in the landscape and flow paths. Conversely, functional connectivity is focused on the dynamic aspects and how spatial patterns interact with catchment processes to produce runoff, connected flow and water transfer (Turnbull et al., 2008). Wainwright and Bracken (2011) pointed out that the interaction among hydrological

processes and topographic controls determines a feedback between rainfall, infiltration and flow routing and that this feedback is responsible for non linearity in stream hydrographs and scale-dependence of runoff coefficients. Functional connectivity is characterized by larger spatial and temporal variability (e.g., landscape units connect differently based on their intrinsic properties and some of this units usually connect/disconnect depending on input water volumes and antecedent wetness conditions) compared to the static structural connectivity. This implies that functional connectivity is more difficult to measure: while capturing snapshots of catchment characteristics and assessing the potential pathways is enough to understand structural connectivity (Bracken et al., 2013). Developing sampling approaches able to investigate process-based connectivity is quite challenging.

Bracken et al. (2013) report that currently, in catchment hydrology studies, the most used interpretation of hydrological connectivity is based on the investigation of flow processes at the hillslope scale. Specifically, connectivity is considered the development of subsurface connections between the hillslopes, the riparian zone and the stream, which occurs when the water table at the upland-riparian zone interface is above a confining layer (Vidon and Hill, 2004; Ocampo et al., 2006). Lateral subsurface flow occurs after the development of saturation above less permeable layers, such as the soil-bedrock interface, or the rise of groundwater into more permeable soil layers (transmissivity feedback). Hillslope-stream connectivity can develop along preferential flow pathways determined by the presence of macropores and soil pipes (e.g., Sidle et al., 2001; Uchida et al., 2001) or along channels in the subsurface topography (e.g., Freer et al., 1997; Graham et al., 2010) or can appear as a diffuse flow (e.g., Freer et al., 1997; Tromp-van Meerveld and McDonnell, 2006a; Jencso et al., 2009). The temporal variability of hillslope-stream connectivity can be very different. For instance, Ocampo et al. (2006) found that hillslopes and riparian zones respond to rainfall events almost independently and differently and they are disconnected from each other during large part of the year. However, they observed that when a shallow groundwater system is established across the hillslope, hydrological connections between the upland and riparian zones persist for 2-3 months during winter. Conversely, other studies (e.g., Tromp-van Meerveld and McDonnell, 2006b; Haught and van Meerveld, 2011) found that hillslope-stream connectivity lasts for only hours or days during which lateral subsurface flow reaches the stream. Hillslope-stream connectivity also strongly varies in space. For example, only some portions of the hillslopes may be connected to the stream during rainfall or snowmelt events, while other areas may be disconnected (Blume

and van Meerveld, 2015). Ambroise (2004) highlighted the important distinction between active and connected (contributing) areas. Water fluxes generated in active areas do not necessarily contribute to the runoff observed at the outlet of the catchment. For instance, saturated areas determined by the rise of the water table are active and variable in space and time, but not all of areas may be connected to the stream and contribute to runoff. During very wet conditions (e.g., during large rainfall events characterized by wet antecedent conditions) the fraction of contributing areas is equal to the active areas, but during dry conditions or for small rainfall events the extent of the contributing areas may be much smaller than the extent of the active parts of a catchment. This concept also implies that some elements of the landscape act as permanent or temporary gatekeepers, preventing the development of connections between active areas and the stream (Phillips et al., 2011). Gatekeepers may be ridge sites, locations characterized by bedrock outcrop or less permeable soil layers or riparian zones affected by a quick rise in groundwater and flow reversals due to the infiltration of stream water.

Hydrological connectivity has important effects both on runoff generation and the transport of all substances that move with the water along a flow path. The ability of water in infiltrating into the soil, moving vertically and horizontally facilitates the physical transfer of solutes, sediment and organisms across the landscape (e.g., Pringle, 2003; Tetzlaff et al., 2007). Therefore, the connectivity among different portions of a catchment influences biophysical and biogeochemical processes (Brierley et al., 2006), making the connectivity concept of wide interest not only to hydrologists, but also for ecologists and geomorphologists. Improving the current knowledge on how elements of the landscape become connected, which factors control spatial and temporal variation in hydrological connectivity and how natural and anthropogenic disturbances affect connectivity has practical implications in watershed management. Indeed, knowledge of functional or process-based hydrological connectivity is fundamental for a better understanding and prediction of the runoff response, floods, erosion and sedimentation processes and dispersion of pollutants. Therefore, an objective of the thesis is to quantify and compare the spatial and temporal variability in subsurface connectivity in five headwater catchments and to determine its relation to the characteristics of rainfall-runoff events and streamflow dynamics. Subsurface connectivity was studied using a hillslope-centered approach (Blume and van Meerveld, 2015) based on networks of spatially-distributed piezometers and quantified by a graph-theory approach. Graph theory has been proven to be a good method for

investigating network properties and dynamics in earth and environmental sciences (e.g., Phillips et al., 2011; Heckmann et al., 2015; Phillips et al., 2015).

2.3. Hysteresis between hydrological variables at the runoff event timescale

Hysteresis is a non-linear loop-like behaviour that is common in natural systems. Phillips (2003) defined hysteresis in geomorphic systems as a phenomenon where two or more values of a dependent variable are associated with a single value of an independent variable. Similarly, O'Kane (2005) suggested that hysteretic loops in hydrological systems could be seen as rate-dependent behaviours that do not show affine similarity with respect to time. In other words, when the time-argument of an input function is stretched or compressed, the corresponding output function is not stretched in the same way (O'Kane, 2005). Typically, this occurs when a time lag exists between the two variables (Prowse, 1984). Hysteresis can thus be thought of as the dependence of a response variable not only on the value of a driving variable but also on its past history (Camporese et al., 2014; Norbiato and Borga, 2008; Visintin, 2006).

Hysteretic relations are common in hydrology. Hysteresis occurs in the relation between soil water content and pressure head (soil water retention curve) and between stream stage and streamflow during unsteady flow conditions. Hysteresis has also been identified in the relation between streamflow and a number of other hydrologic variables: precipitation (e.g., Andermann et al., 2012), groundwater level (e.g., Fovet et al., 2015; Camporese et al., 2014; Allen et al., 2010; Frei et al., 2010), soil moisture content (e.g., Penna et al., 2011; Parajka et al., 2006), extent of the saturated area (e.g., Shook and Pomeroy, 2011; Niedzialek and Ogden, 2004), storage (e.g., Davies and Beven, 2015), hillslope flow (e.g., McGuire and McDonnell, 2010), sediment concentrations (both bedload and suspended sediment, e.g., Mao et al., 2014; Landers and Sturm, 2013), solute concentrations (e.g., Burt et al., 2014; Cartwright et al., 2014; Outram et al., 2014; Aubert et al., 2013; Hornberger et al., 2001; Evans and Davies, 1998) and stream water temperature (Blaen et al., 2013; Subehi et al., 2010). Hysteretic relations were also found between the diurnal variation in evapotranspiration and vapour pressure deficit (e.g., Zhang et al., 2014; Zheng et al., 2014), spatial mean soil moisture and coefficient of variation (e.g., Fatichi et al., 2015; Ivanov et al., 2010), bulk and fluid electrical conductivity (e.g., Briggs et al., 2014), air and river water temperature (e.g., Wilby et al., 2014) and surface water cover and water storage (e.g., Kuppel et al., 2015).

Analysis of hysteretic relations has led to a better understanding of the nonlinear mechanisms underlying runoff generation at various scales (Spence et al., 2010). The changing direction of the hysteretic relation between hillslope flow and streamflow (McGuire and McDonnell, 2010) and between hillslope soil moisture and streamflow (Penna et al., 2011) have, for example,

highlighted the influence of antecedent soil moisture conditions on the timing of hillslope contributions to streamflow. Similarly, changes in the relation between streamflow and solute concentrations have been related to the different degree of connectivity of hillslopes and stream tributaries (Murphy et al., 2014) or different solute sources in the catchment (Shanley et al., 2015). Differences in hysteresis in the relation between sediment concentrations and streamflow for different events or different catchments have been interpreted with respect to differences in the source area of the suspended sediment. Generally clockwise hysteretic loops are related to a quick flushing of sediment close to the measurement location (e.g., Mano et al., 2009). Aich et al. (2014) showed differences in hysteresis for a series of runoff events for a hillslope and the catchment outlet, providing valuable information about the differences in exhaustion of sediment sources, and seasonal changes in sediment detachment and transport. Numerical simulations showed that the hysteretic relation between sediment concentrations and flow depends on the particle size distribution of the soil and the presence of a deposited layer that protects the soil below (Sander et al., 2011). Studying hysteretic relations for different events or differences in hysteretic patterns between different sites can thus reveal important information about the underlying hydrological processes.

Analysis of hysteretic patterns is typically carried out via a bivariate plot to highlight the relation between the response of one parameter to variations in another parameter. Hysteretic relations can also be described and analysed with indices or metrics that quantify the three main characteristics of hysteretic relations: *i*) the shape (circular, eight-shaped or linear), *ii*) the direction (clockwise and anti-clockwise) and *iii*) the extent of the loop. Quantitative indices are valuable tools to compare hysteretic loops at various space- and timescales, to develop a classification of hysteretic patterns, to detect changes in hysteretic loops or to test the ability of models to reproduce the observed hysteretic behaviour (Fovet et al., 2015; Zhang et al., 2014; Zheng et al., 2014). In the past decade, several researchers have developed indices to quantify the shape, the size and the direction of hysteretic loops. For instance, Poggi-Varaldo and Rinderknecht-Seijas (2003) analysed the hysteretic behaviour in adsorption-desorption and derived the *Hysteresis Coefficient*, defined as the ratio of the derivatives of the adsorption and desorption isotherms at a given point. Butturini et al. (2006) examined the temporal variation in hysteresis between streamflow and dissolved organic carbon and nitrate concentrations. Their index, ΔR, integrated information about the area and the direction of the hysteretic loop and was obtained by standardizing streamflow and solute concentrations and multiplying the

extent of the loop by the term R ($R = 1$ for clockwise loops, $R = -1$ for anti-clockwise loops and $R = 0$ for unclear patterns or a linear relation between streamflow and solute concentration) and then by 100. Therefore, ΔR varied between -100 (for large anti-clockwise loops) and 100 (for large clockwise loops). Bieroza and Heathwaite (2015) successfully used this index to study the seasonal variation in hysteresis between streamflow and phosphorus concentrations. Several other methods for the quantification of hysteretic relations were based on measurements of suspended sediment concentrations and streamflow. Langlois et al. (2005) analysed suspended sediment transport dynamics during a snowmelt period in a small forested catchment in Nevada, USA. They plotted suspended sediment concentrations against streamflow and computed regression lines for both the rising and the falling limb of the hydrograph. The area under the curve for the two regression equations was estimated by integration using the lowest streamflow and the maximum streamflow observed during the event as the lower and upper limits, respectively. The hysteresis index, H, was computed as the ratio of these two areas, where $H \approx 1$ indicated weak hysteresis, $H > 1$ a clockwise hysteretic loop and $H < 1$ an anti-clockwise hysteretic loop. Lawler et al. (2006) studied turbidity during spring storm events in an urban catchment in the UK and also developed a dimensionless index to quantify the magnitude and direction of hysteresis in the relationship between streamflow and turbidity. Their index was based on the extent of the hysteretic loop at the mid-point of streamflow during the event (i.e., halfway between baseflow prior to the event and peak streamflow). Interpolation was used to find the two turbidity values at the mid-point streamflow. The direction of hysteresis was expressed by the index HI_{mid} and based on a conditional statement: if turbidity on the rising limb was higher than on the falling limb, the loop was clockwise, otherwise it was anti-clockwise. Lawler et al. (2006) state that HI can also be computed for multiple streamflow points and then averaged (HI_{mean}, Lawler et al., 2006). Smith and Dragovich (2009) developed a dimensionless similarity function based on individual line lengths and angles between the suspended sediment concentration and streamflow for each sampling time. They used this index to study the similarity in the hysteretic patterns between suspended sediment concentrations and streamflow at the outlet of two nested catchments in South-Eastern Australia and showed that quantitative measures of hysteretic patterns at the event timescale provided a mechanism for linking the timing and magnitude of responses across spatial scales (Smith and Dragovich, 2009). Landers and Sturm (2013) used turbidity measurements to estimate suspended sediment concentrations in a mesoscale catchment in Georgia, USA. They quantified hysteresis between suspended sediment

concentrations and streamflow and between suspended sediment concentrations and turbidity at the runoff event timescale by computing the range and the coefficient of variation of the ratios of streamflow and turbidity to suspended sediment concentration. They based these calculations on the observation that, where hysteresis occurred, the magnitude of hysteresis (i.e., the nonlinearity in the bivariate plot) increased with increasing range and coefficient of variation in those ratios. Finally, Aich et al. (2014) normalised streamflow and sediment concentrations and computed the *Hysteresis Index* (*HI*) as the sum of the maximum distances between the rising and the falling limb of the hysteretic loop and the line that links the streamflow peak to the last sediment concentration data point. *HI* was positive for clockwise hysteresis and negative for anti-clockwise loops. They used this index to compare hysteresis in the relation between streamflow and suspended sediment concentrations at the catchment outlet and a hillslope.

The use of these indices provided detailed understanding of the processes investigated and proved to be useful for the specific cases for which they were developed. However, these existing indices also have some limitations. Some of them require a certain degree of subjectivity and interpretation during their application, which limits their robustness and their use for identifying changes in hysteretic patterns in long data series (e.g., Langlois et al., 2005). They were also not developed to take into account more complex hysteretic patterns, such as eight-shaped loops that combine both clockwise and anti-clockwise hysteresis (e.g., Aich et al., 2014; Langlois et al., 2005). In addition, some indices (e.g., Lawler et al., 2006; Langlois et al., 2005) cannot be used with negative values (e.g., isotopic delta values). Finally, none of these studies provided a sensitivity analysis to verify the results of the index. Knowledge of the sensitivity of the index is needed when the index is used for long data series with many events, e.g., to study seasonal changes in hysteresis, to compare hysteretic responses in different catchments or at different scales, or to compare observed and modelled hysteretic relations. This is particularly the case when noisy input data or different time intervals (temporal resolution) are used. Therefore, an objective of the thesis is to introduce a versatile index for the quantification of a wide range of hysteretic loops at the runoff event timescale. Specifically, the aim is to: *i*) present an index that is able to predict the eight main hysteretic loop types, *ii*) test the robustness and usefulness of the index using synthetic data and field data from experimental catchments in Northern Italy, and *iii*) assess the sensitivity of the index to noisy data and data with different temporal resolutions.

3. STUDY AREAS AND MATERIALS AND METHODS

3.1. Analysis and modeling of soil moisture spatial variability

3.1.1. Soil moisture measurements at the plot scale in Grugliasco

Numerous studies have examined the spatial variability of surface soil water content as a function of the mean soil moisture status and of controlling variables related to soil properties, vegetation and topography, with varying conclusions. One main generalization is that as the mean soil moisture approaches limiting states, at the dry or wet ends, the absolute spatial variability of soil moisture becomes smaller. Between these bounds, however, the trajectories of the spatial variability can be non-unique and dependent on climate, soil, vegetation, topography, and antecedent states (Lawrence and Hornberger, 2007). Relatively few studies have focused on the impact of land use characteristics on the main statistics of soil moisture fields, owing to the difficulties in isolating and examining the vegetation contribution with respect to that of the soil properties and topography.

Soil moisture observations were collected over three years (2006-2008) on a plot (about 200 m^2) in Grugliasco (Po Plain, Northern Italy) at 290 m a.s.l. (Fig. 3.1.1) by means of 40 Time Domain Reflectometry probes. A broader description of the study site is reported in Baudena et al. (2012). The probes were vertically inserted generating minimal disturbance, owing to the sandy texture and the lack of stones, in the 0-30 and 0-60 cm depth. The plot is divided into two subplots: one covered by grapevine plants (monitored with 12 and 11 probes at 0-30 and 0-60 cm depth, respectively), the other covered homogeneously by grass (monitored with 9 and 8 probes at 0-30 and 0-60 cm depth, respectively). The terrain slope is about 1%, the soil is sandy and around the measurement field there is a buffer grass area about 20 m wide. Precipitation and temperature are recorded continuously on site. The characteristics of the site allow to isolate the contribution of soil hydraulic properties and land use to soil moisture variability. Rainfall climatology in this area is characterized by two maxima, respectively in spring (April–May) and fall (October–November), with relatively dry winter and summer (Ciccarelli et al., 2008). During the three observation years the annual precipitation ranged between 755 mm (2007) to 1183 mm (2008), whereas potential evapotranspiration (estimated by means of the Hargreaves method) ranged between 935 mm (2008) and 1001 mm (2007).

For the purpose of the analysis, soil moisture observations were aggregated at the daily time step, retaining the day when at least four instantaneous observations are available.

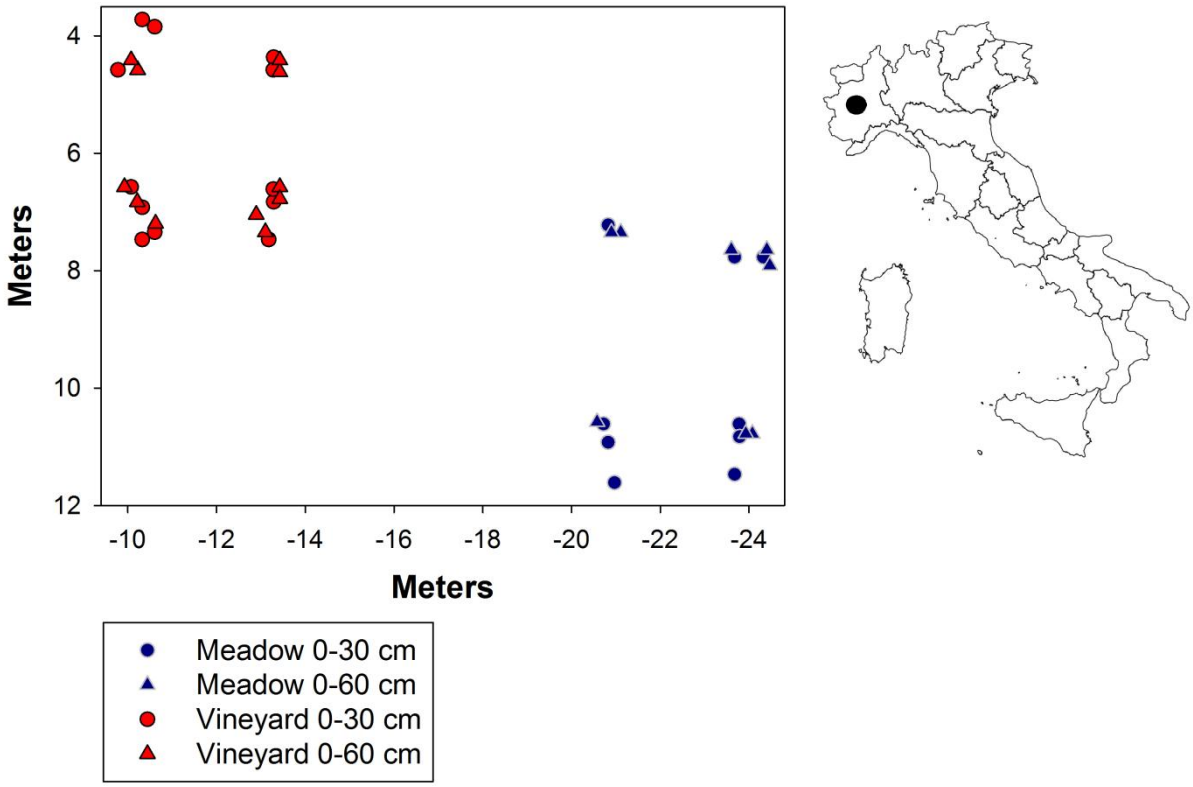

Fig. 3.1.1. Map of the experimental site in Grugliasco.

3.1.2. Soil moisture dynamics model

To assess the influence of the land use characteristics on the soil moisture variability a soil moisture dynamics model developed by Teuling and Troch (2005) was applied. The advantage of this model approach is that the number of parameters is small, while the parameters still reflect observable properties (Romano et al., 2011). Models of similar complexity have been shown to correctly simulate the root zone soil moisture dynamics under different climatic conditions. The equations of the model are given as follows (Teuling and Troch, 2005).

The point-scale soil moisture dynamics is spatially unconnected. Vertical redistribution of soil moisture is assumed to occur instantaneously (at the daily time step). The daily water balance for a number of independent soil columns is solved following:

$$\frac{d\theta}{dt} = \frac{1}{L}(T - S - E - R - q) \tag{3.1.1}$$

where θ is the volumetric soil moisture, L is the depth of the root zone, T the throughfall (i.e., the rainfall that is not intercepted by the vegetation), S the root water uptake, E the evaporation from the soil surface, R the saturation excess runoff (i.e., the part of T that causes oversaturation of the soil) and q the deep drainage. Lateral flow is assumed to be negligible in

the root zone. Deep drainage is computed using the following parameterization (Campbell, 1974):

$$q = k_s(\frac{\theta}{\Phi})^{2b+3} \tag{3.1.2}$$

where k_s is the saturated hydraulic conductivity, b is the pore size distribution parameter, Φ is the porosity. The vertically integrated root water uptake is thought to be proportional to a maximum transpiration rate E_p, a soil moisture stress function $\delta(\theta)$ and a function accounting for spatially variable response of unstressed transpiration to atmospheric boundary layer conditions (Al-Kaisi et al., 1989). The root water uptake is computed as follows:

$$S = f_r\delta(\theta)[1 - \exp(-c\xi)]E_p \tag{3.1.3}$$

where f_r is the root fraction in the layer of depth L, $\delta(\theta)$ is a soil moisture stress function, c is a light use efficiency parameter, ξ is the Leaf Area Index (LAI). The factor $[1 - \exp(-c\xi)]$ allows to account for LAI (ξ). Soil moisture stress is modelled as:

$$\delta = max\left[0; \min\left(1; \frac{\theta-\theta_w}{\theta_c-\theta_w}\right)\right] \tag{3.1.4}$$

where θ_c is the critical soil water content and θ_w is the wilting point, which defines the transition between unstressed and stressed transpiration.

LAI (ξ) is modelled with a spatial and temporal component (Penna et al., 2009; Teuling and Troch, 2005):

$$\xi = \xi_{max}\left[c_1 - (1 - c_1)\sin\left(2\pi\frac{DOY-c_2}{c_3} + \frac{\pi}{2}\right)\right] \tag{3.1.5}$$

where ξ_{max} is the local maximum of ξ, and the parameters c_1 and c_2 indicate the seasonal variation of ξ.

Bare soil evaporation is assumed to be small in comparison to the root water uptake over the entire soil profile. The root zone depth is assumed equal to 30 cm. During the implementation, the model was initialized by using observed soil moisture values. The model was applied at the daily time step, using local rainfall and potential evapotranspiration. The model was calibrated based on the time series of mean soil moisture measured at 0-30 cm depth in 2008 and verified over 2006 and 2007. The Nash-Sutcliffe index of efficiency (NS) and the Root Mean Square (RMSE) were used to quantify the model adequacy.

3.2. Temporal stability of throughfall and soil moisture patterns

3.2.1. Study area: Ressi catchment

The 1.96-ha Ressi study catchment is located in the Southern part of the Posina River basin (116 km^2) at the foothills of the Central-Eastern Italian Alps (45°47’11.79’’ N; 11°15’ 54.12’’ E) (Fig. 2.a.1.1). The Posina River is a tributary of the Astico River that flows into the Adriatic Sea. Around 74% of the Posina basin is densely vegetated (Norbiato et al., 2009), in part due to marked expansion of deciduous forests in the last five decades as a result of abandonment of agricultural practices. Beech, chestnut, maple and hazel are the main species in the catchment; hornbeam and ash are less common. The climate is humid temperate. The average annual precipitation (1992-2007) recorded by a weather station in the central part of the Posina basin (at 597 m a.s.l., approximately 4.5 km in a straight line from Ressi) is 1695 mm. The average annual temperature is 9.7 °C; average monthly temperatures range between 1.2°C in January and 18.7°C in July. Rainfall is concentrated in spring (150 mm and 159 mm on average in April and May, respectively) and autumn (236 mm and 246 mm on average in October and November, respectively). Elevations in the study catchment range from 609 to 725 m a.s.l.. The mean slope is 26°; the aspect is predominantly North-West. The channel is approximately 150 m long. The channel and relatively flat near-stream zone that is frequently saturated comprise roughly 1.5% of the catchment area. The geology in Ressi catchment consists of a sequence of rhyolites and dacites from Triassic volcanic extrusions (Sedea et al., 1986). The soil is classified as Cambisol (ARPAV, 2005). The topsoil (0-10 cm) has a sandy clay loam texture, while deeper in the profile the soil has a sandy clay texture.

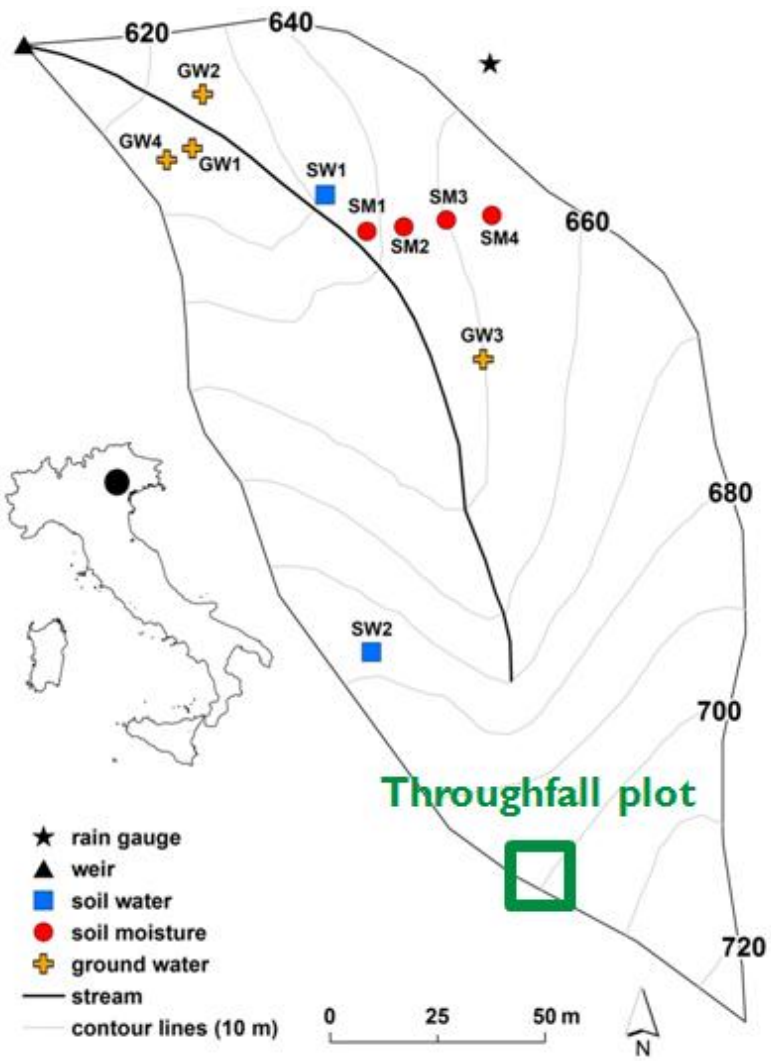

Fig. 3.2.1. Map of Ressi catchment showing the location of the field measurements and the sampling locations. GW: groundwater; SW: soil water; SM: soil moisture. The location of Ressi catchment in Italy is shown in the inset.

Hydrometric and tracer data (stable isotopes of water and electrical conductivity) has been collected since August 2012. Rainfall was measured using a 0.25 mm tipping bucket (Spectrum Technologies Inc., United States of America; Decagon Devices Inc., United States of America) in an open area just outside Ressi catchment (Fig. 3.2.1). Unfortunately, due to malfunctioning of the data-logger, rainfall data were not available for several periods and were unreliable during freezing conditions. Precipitation was also measured at three weather stations operated by the Regional Agency for Environmental Protection and Prevention of Veneto (ARPAV): Passo Xomo (1056 m a.s.l.), Contrà Doppio (725 m a.s.l.) and Castana (430 m a.s.l.), at 2.3, 3.9 and 4.8 km from the catchment, respectively. Comparison of measured rainfall at Ressi and the inverse distance weighted (IDW) mean precipitation from the three weather stations showed that there was a very good and good correlation between the two data series for event-based total

rainfall (R^2 = 0.91; n = 25) and average rainfall intensity (R^2 = 0.44; n = 25), respectively, and that the data plotted almost on a 1:1 line.

Stream stage was measured at a 5-min interval by a pressure transducer (Keller AG für Druckmesstechnik, Switzerland) behind a V-notch weir (Fig. 3.2.2). Streamflow was measured during different flow conditions using the volumetric method to check the weir equation. Groundwater levels were monitored at a 5-min resolution in two riparian wells (GW1 and GW2) and in one well at the bottom of the hillslope (GW3, Fig. 3.2.1). GW1 was equipped with a pressure transducer (Solinst Ltd., Canada), whereas GW2 and GW3 were equipped with a capacitance water level logger (Trutrack Ltd., New Zealand). The depth of the wells was 2.04, 1.04 and 0.68 m for GW1, GW2, and GW3, respectively. Near-surface (0-30 cm) soil moisture was measured at a 10-min interval using four reflectometers (CS625, Campbell Scientific Inc., United States of America). The probes were installed at different positions along a transect: SM1 was positioned in the riparian zone, approximately 1 m from the stream, SM2 at the transition between the riparian zone and the hillslope (footslope), SM3 in the middle part of the hillslope and SM4 in the upper part of the hillslope (Fig. 3.2.1). The reflectometers were not specificallly calibrated for the soil in Ressi as the research was more focused on the temporal variation in soil moisture, rather than the actual soil moisture content. Therefore the manufacturer's equation for clay soils was used to determine soil moisture content.

Fig. 3.2.2. Outlet of the Ressi catchment.

3.2.2. Throughfall measurements

The redistribution of rainfall by the canopy determines the amount of rain water reaching the soil surface and typically results in marked spatial and temporal variability in throughfall (Levia and Frost, 2006; Keim et al., 2005). This spatial variability in throughfall has important effects on soil moisture (Coenders-Gerrits et al., 2013) and soil chemistry (Kohlpaintner et al., 2009; Raat et al., 2002), as well as subsurface stormflow generation (Hopp and McDonnell, 2011; Bouten et al., 1992). However, capturing this variability and understanding its controlling factors is not straightforward, in part because of the possible bias introduced by the use of different throughfall collectors or by adopting different experimental designs and sampling strategies (Zimmermann et al., 2010; Holwerda et al., 2006). Unlike rainfall, there are no standardized instruments or sampling designs to measure and monitor throughfall amount and variability in forested environments. Previous studies have shown that roving gauges are more likely to capture dripping points and thus give a better estimate of average throughfall amount (Ritter and Regalado, 2014; Holwerda et al., 2006) but the roving of the gauges makes it more difficult to study the link between throughfall and soil moisture or soil chemistry.

For this thesis two types of throughfall collectors were installed to assess: *i*) the difference in throughfall amount obtained by the two types of collectors; *ii*) the difference in throughfall spatial variability based on the two types of measurements; and *iii*) if the two types of collectors identify a similar number of spatial clusters and outliers in throughfall.

Throughfall was measured from April 2013 to March 2014 in a 500 m^2 experimental plot (Fig. 3.2.3 and 3.2.4) on a hillslope of the forested Ressi catchment in the Italian pre-Alps. The main tree species in the plot are beech and chestnut (Fig. 3.2.5). The stem density in the plot is 3100 trees/ha; the basal area is 57.1 m^2/ha. The diameter at breast height varied between 1 and 61 cm (median: 4 cm). Two different types of throughfall collectors were used: buckets (BK; collecting area per bucket: 556 cm^2; capacity: 162 mm) and rain gauges (RG; collecting area per gauge: 47 cm^2; capacity: 90 mm). Fifty buckets were randomly distributed in the plot, while 40 rain gauges were installed on a regular grid (2.5 m by 3 m spacing). The buckets covered 0.56% of the plot area, whereas the rain gauges covered 0.04% of the area. Positions of the throughfall collectors were determined using a laser distance meter. A bucket and a rain gauge were installed in a nearby open area as well (approximately 150 m from the experimental plot) to collect gross rainfall. Rainfall and throughfall collected in buckets were measured for a total of 24 samplings (gross rainfall range: 4-155.7 mm; mean rainfall intensity range: 0.3-8.3 mm/h)

by manually emptying the collectors and measuring the volume of water. Similarly, rainfall and throughfall were measured manually in rain gauges for 21 samplings.

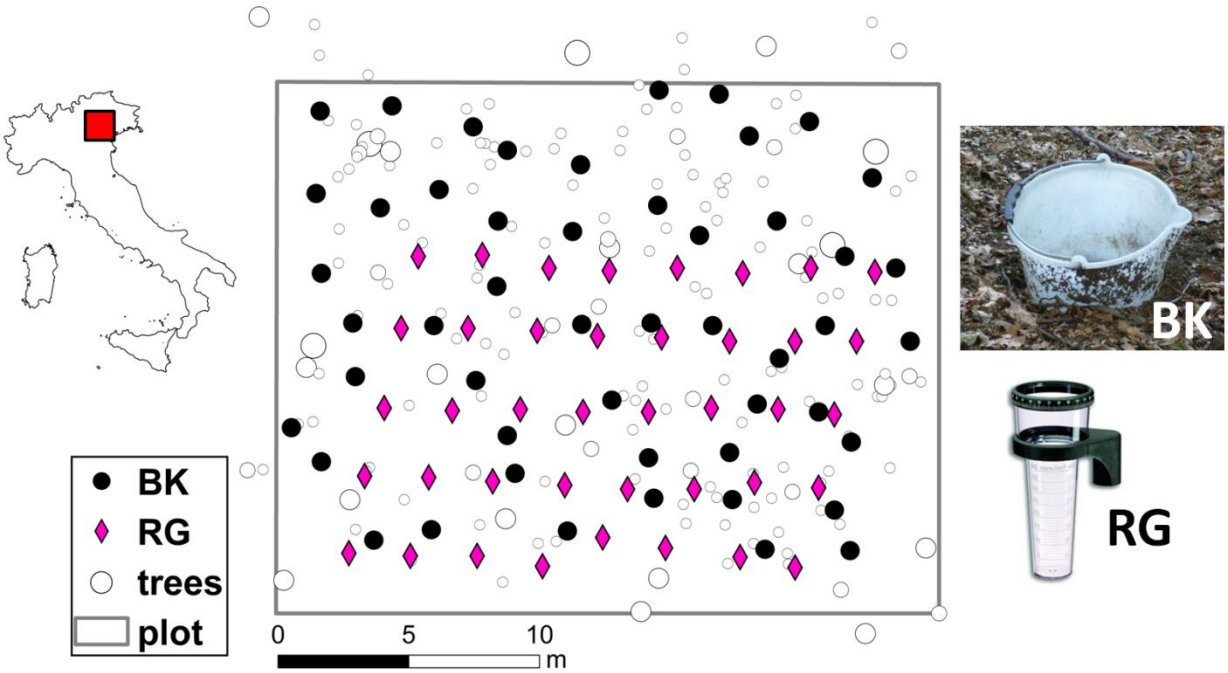

Fig. 3.2.3. Location of the throughfall plot in Italy and the spatial distribution of the trees and the two types of throughfall collectors in the plot (BK: buckets; RG: rain gauges).

Fig. 3.2.4. Buckets and rain gauges installed in the experimental plot.

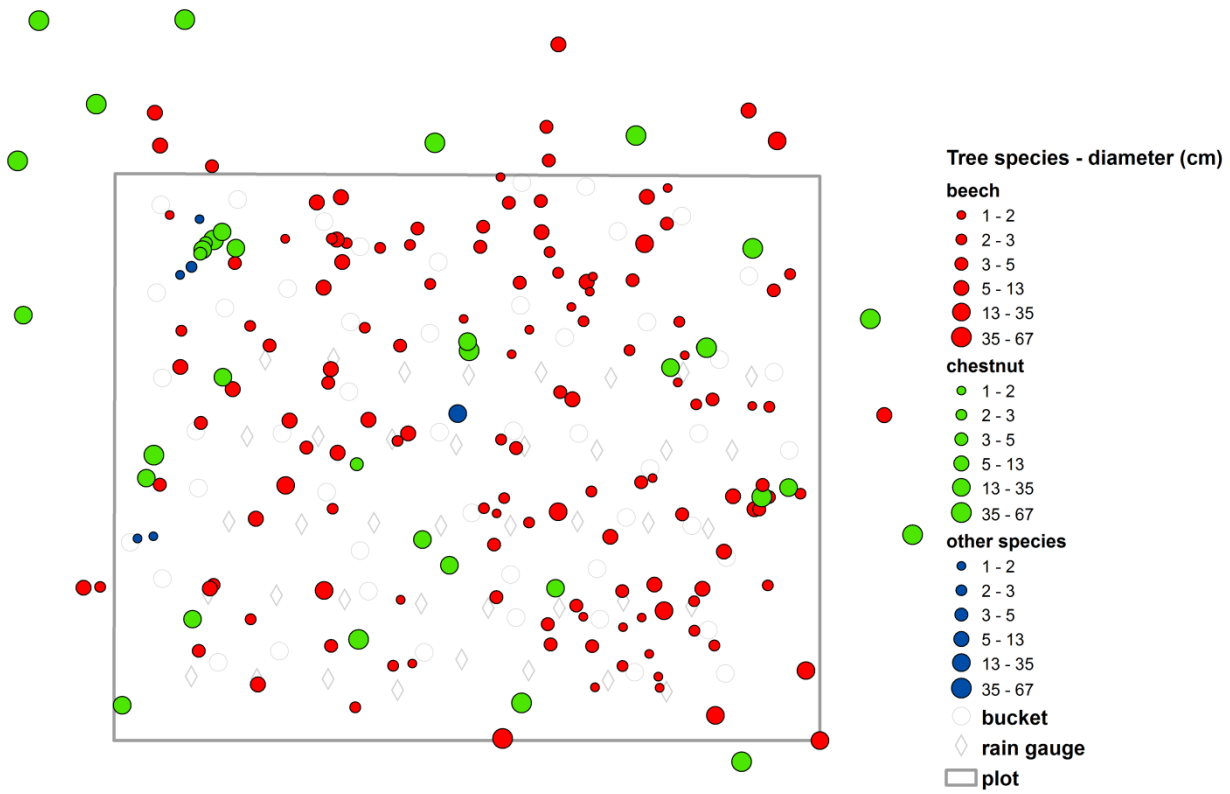

Fig. 3.2.5. Location of the trees in the throughfall plot.

The difference in throughfall amount and spatial variability in throughfall obtained by the two types of collectors was analyzed for 21 measurements. The rainfall characteristics for the events (Table 3.2.1) were determined from the inverse distance-weighted mean rainfall measured at three weather stations operated by the Regional Agency for Environmental Protection and Prevention of Veneto (ARPAV): Passo Xomo, Contrà Doppio and Castana (Section 3.2.1).

Throughfall was expressed as the fraction of rainfall that fell through the canopy and reached the ground (i.e., the ratio between throughfall measured at each collector (mm) and gross rainfall measured in the open area (mm), multiplied by 100). The bootstrap method (Efron, 1979) was used to resample throughfall measured by the two types of collectors 10,000 times to compare the differences in the throughfall means for each measurement day. To investigate the optimum sample size for both throughfall collectors, we computed the number of collectors required to measure throughfall for each measurement day d (Holwerda et al., 2006; Kimmins, 1973):

$$m_d = \frac{z_\varphi^2 \times CV_d^2}{\varphi^2} \tag{3.2.1}$$

where m_d is the required number of collectors, z_φ is the critical value of 95% confidence level (2.0; Kimmins, 1973), φ is the pre-set error in percentage of the mean (10% in this study) and CV_d is the coefficient of variation of throughfall measured on day d.

The analysis of local spatial clusters and outliers in measured throughfall was carried out by computing the Local Moran's index I (Anselin, 1995) for each measurement day for both types of collectors:

$$I_i = \frac{g_i \sum_{j=1}^{n} w_{ij} g_j}{\sum_{j=1}^{n} g_j^2 / N} \tag{3.2.2}$$

where $g_i = T_i - \bar{T}$, the deviation of the throughfall (T_i) measured at collector i from the mean throughfall, $\bar{T}$; w_{ij} is the spatial weight between collectors i and j and N is the total number of collectors. For the calculation of the Local Moran's I, the inverse distance weights were used to characterize the spatial relations between the throughfall collectors.

	Mean	**Min.**	**Max.**
Gross rainfall (mm)	28.6	4.0	82.6
Mean rainfall intensity (mm/hr)	1.3	0.3	4.0
Max. rainfall intensity (mm/hr)	6.8	1.0	29.8
Duration (hr)	23	8	44
Plot-averaged throughfall based on BK data (%)	80.1	69.7	93.5
Plot-averaged throughfall based on RG data (%)	82.2	68.4	100.2

Table 3.2.1. Characteristics of rainfall events for the 21 throughfall measurements considered for the comparison of the two types of throughfall collectors.

3.2.3. Soil moisture measurements at the plot scale in Ressi catchment

Near-surface soil moisture was measured at the throughfall plot in the Ressi catchment to assess whether throughfall patterns influence the spatial and temporal variability of soil moisture.

Volumetric soil moisture content was measured at 50 points in the immediate vicinity (~ 30 cm upslope) of each bucket at two depths (0-7 and 0-12 cm) using portable TDR (Time Domain Reflectometry) probes (FieldScout TDR300, Spectrum Technologies Inc., USA; Fig. 3.2.6). These instruments were used for data collection in Penna et al. (2009, 2013), while an evaluation of TDR 300 probes can be found in Brevik and Batten (2012). Soil moisture measurements were taken before the rainfall events and during the 2-36 hour period after the end of the events. At each sampling site and for each sampling depth five measurements of the soil water content

were taken, then the truncated mean was computed by discarding the minimum and maximum value. In total, soil moisture was sampled 49 and 48 times for 0-7 cm and 0-12 cm depth, respectively. Soil moisture measurements were not specifically calibrated for the soil in Ressi as the research was more focused on the temporal variability of the patterns and correlation with the throughfall spatial patterns, rather than the actual soil moisture content.

Fig. 3.2.6. TDR probe used for the soil moisture measurements at the throughfall plot.

3.2.4. Analysis of temporal stability of throughfall and soil moisture

The relation between soil moisture at the two depths and the relation between throughfall and soil moisture spatial patterns were computed by the Spearman rank correlation coefficient (ρ_s). Furthermore, the relation between throughfall and soil moisture spatial patterns was analyzed in terms of temporal stability (Vachaud et al., 1985). Temporal stability was assessed computing the Spearman rank correlation coefficient (ρ_s) between pairs of observation times, the mean relative difference (MRD) and standard deviation of relative difference (SDRD) for all measurements of throughfall and soil moisture. The relative difference was defined as follows:

$$\tau_{i,t} = \frac{M_{i,t} - \bar{M}_t}{\bar{M}_t} \tag{3.2.3}$$

where $M_{i,t}$ is the soil moisture (or throughfall) measured at site i and time t,

$$\bar{M}_t = \frac{1}{N}\sum_{i=1}^{N} M_{i,t} \tag{3.2.4}$$

$\bar{M}_t$ is the mean value of soil moisture (or throughfall) at time t and N is the number of sampling sites. The mean relative difference for site i was computed as:

$$MRD_i = \frac{1}{Z}\sum_{t=1}^{Z} \tau_{i,t} \tag{3.2.5}$$

where Z represents the number of sampling times. The standard deviation of the relative difference at site i was defined as follows:

$$SDRD_i = \sqrt{\sum_{t=1}^{Z} \frac{(\tau_{i,t} - MRD_i)^2}{Z-1}} \tag{3.2.6}$$

A positive value of MRD for a certain location indicates that the location is wetter or is characterized by larger throughfall than the plot average. Conversely, a negative value of MRD indicates that the location is drier or there is large interception of precipitation by the canopy. The SDRD gives a measure of the variability of the estimate. A MRD close to zero combined to a low SDRD for a location indicates that the location is temporally stable and it is the most representative site of the spatial soil moisture (or throughfall) mean.

3.2.5. Estimation of vegetation characteristics in the throughfall plot

One aim of this study is the assessment of the relation between tree canopies and throughfall temporal stability. Therefore, distance from the nearest tree, canopy openness, LAI and weighted basal area (WBA) were estimated for each bucket.

Canopy openness was determined with two different sampling campaigns on 16/09/2013 and 19/06/2014. During the first campaign pictures were taken with a 24 mm lens (covering an angle of 84°) upward from each bucket and rain gauge (Fig. 3.2.7). Then, canopy openness was estimated selecting thresholds between dark (canopy) and light (sky) areas using the software Adobe Photoshop CS6 (Adobe Systems Inc., USA). During the second field campaign on 19/06/2014, pictures were taken upward from each bucket by a digital camera with a fisheye lens (Fig. 3.2.8). The software Gap Light Analyzer (GLA), developed by the Institute of Ecosystem Studies, Simon Fraser University (Canada), was used for the computation of canopy openness and LAI (e.g., Konishi et al., 2006). The two methods yielded different results: canopy openness ranged between 2.9 and 7.9% and between 5.0 and 11.6% for pictures taken with the 24 mm lens and the fisheye lens, respectively. Furthermore, the values of canopy openness obtained with the two sampling campaigns were not significantly correlated, probably due to small-scale variability in canopy openness (there were no large gaps in the canopy). LAI, computed with the software GLA for the pictures taken with the fisheye lens, ranged between 2.6 and 4.2, with an average of 3.3.

The distance between each bucket and the nearest tree was computed after the field survey on 16/09/2013 to determine the location and the basal area of each tree (Fig. 3.2.5). The distances from the nearest tree ranged between 0.24 and 1.80 m. In addition, WBA (Tromp-van Meerveld and McDonnell, 2006c) was computed for each bucket (BK) as follows:

$$WBA_{BK} = \sum_{all\ trees} \frac{BA_{tree}}{dist_{tree-BK}^{\gamma}} \qquad (3.2.7)$$

where BA_{tree} is the basal area of a tree, $dist_{tree-BK}$ is the distance between the tree and the bucket and γ is a constant determining how rapidly the weighting of a tree declines with the distance.

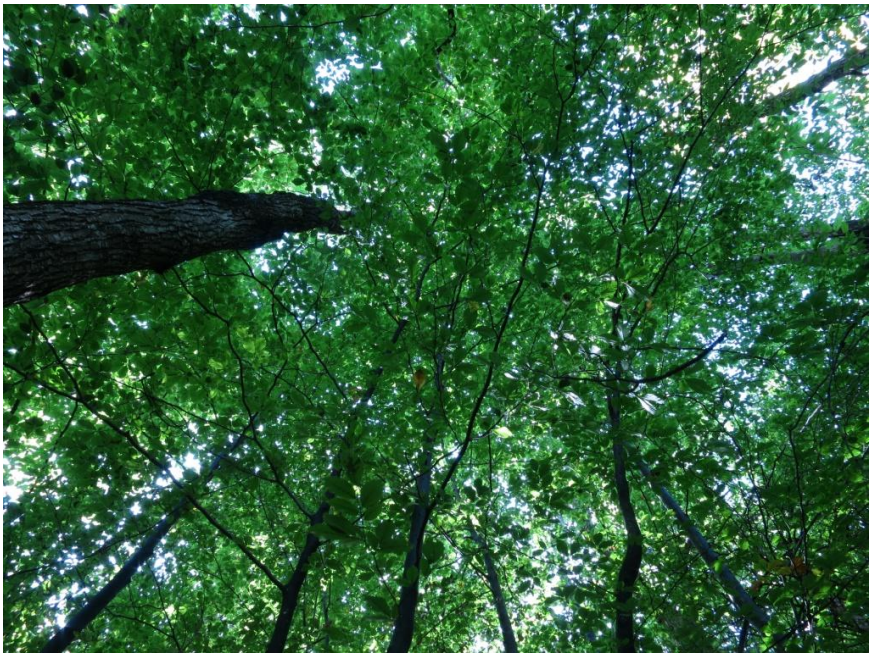

Fig. 3.2.7. Picture of the canopy above BK 13, taken with a 24 mm lens on 16/09/2013.

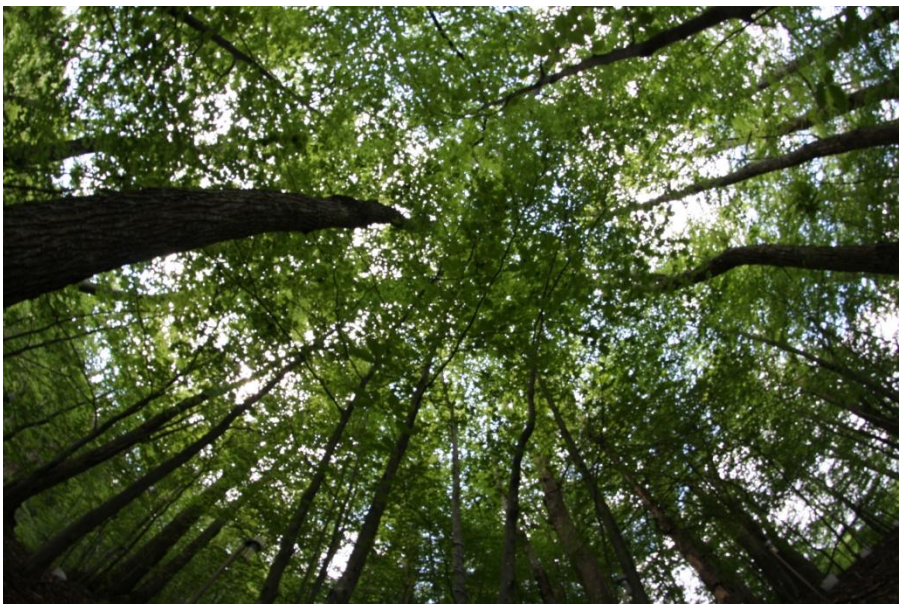

Fig. 3.2.8. Picture of the canopy above BK 13, taken with a fisheye lens on 19/06/2014.

3.2.6. Evaluation of the controls on temporal stability of near-surface soil moisture

The soil moisture dynamics model (Teuling and Troch, 2005) described in Section 3.1.2 was used to investigate how the variability in saturated hydraulic conductivity and vegetation parameters control soil moisture temporal stability and the correlation with throughfall patterns. Soil moisture variability dynamics were simulated for 50 independent soil columns of

7 and 12 cm depth, with vertically uniform hydraulic characteristics. The spatial variability of saturated hydraulic conductivity was simulated by the generation of sets of values drawn from lognormal distributions (Teuling and Troch, 2005; Martinez et al., 2013) with different values of mean (μ_{k_s}) and standard deviation (σ_{k_s}) of saturated hydraulic conductivity (Fig. 3.2.9 and 3.2.10; Table 3.2.2).

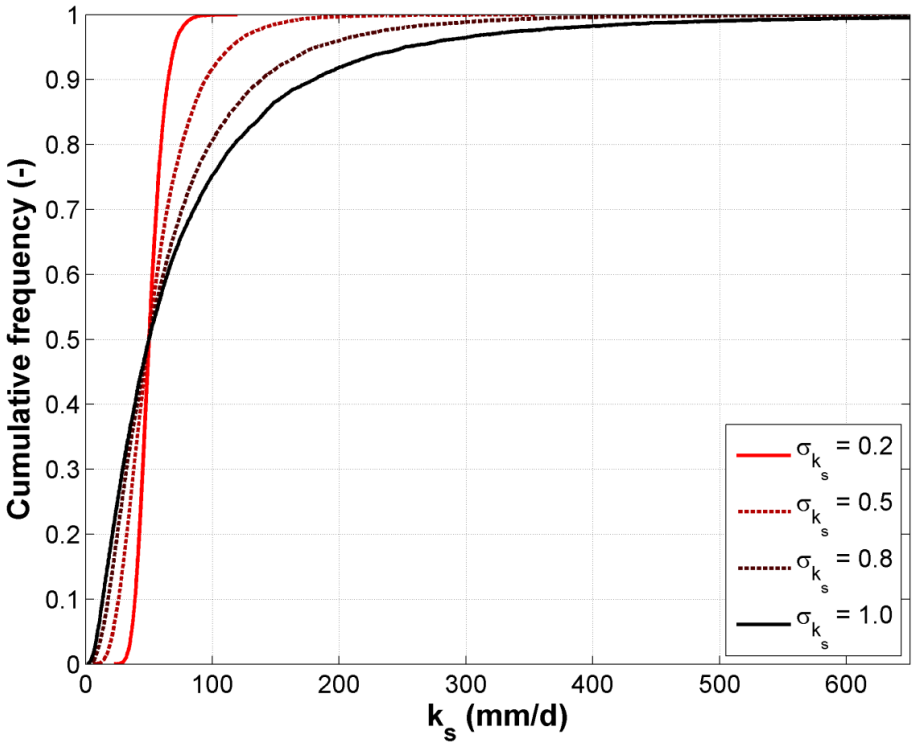

Fig. 3.2.9. Cumulative frequency distributions of simulated saturated hydraulic conductivity with a mean of 50 mm/d and different values of standard deviation (logarithmic scale).

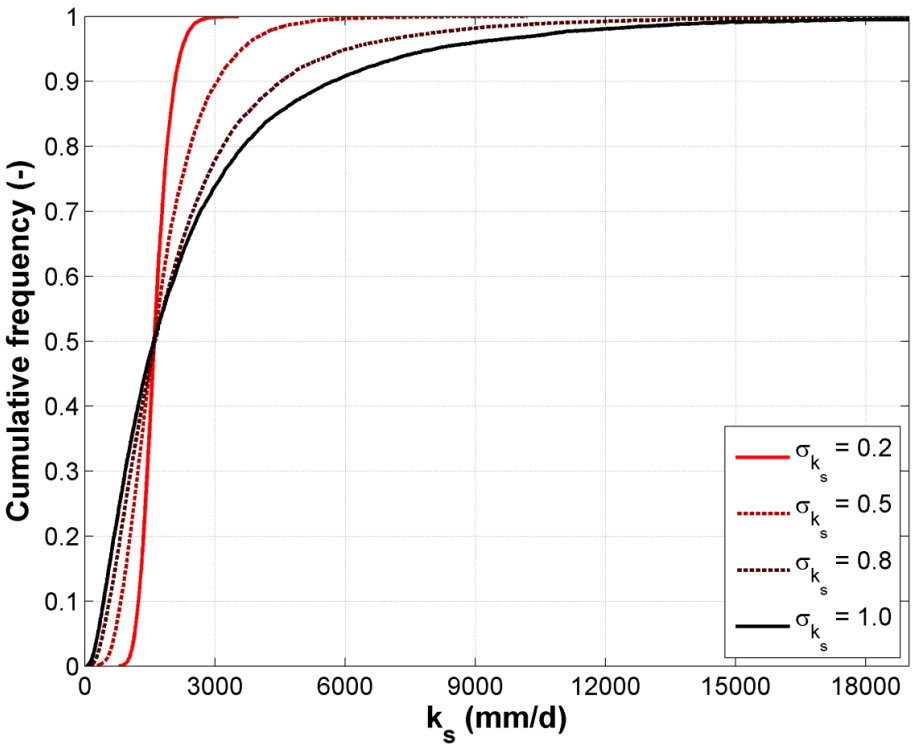

Fig. 3.2.10. Cumulative frequency distributions of simulated saturated hydraulic conductivity with a mean of 1600 mm/d and different values of standard deviation (logarithmic scale).

μ_{k_s} (mm/d)	$ln\ \mu_{k_s}$ (-)	$ln\ \sigma_{k_s}$ (-)
50	3.91	0.2, 0.5, 0.8, 1.0
100	4.61	0.2, 0.5, 0.8, 1.0
200	5.30	0.2, 0.5, 0.8, 1.0
400	5.99	0.2, 0.5, 0.8, 1.0
800	6.68	0.2, 0.5, 0.8, 1.0
1600	7.38	0.2, 0.5, 0.8, 1.0
3200	8.07	0.2, 0.5

Table 3.2.2. Mean and standard deviation values of logarithmic k_s used in the simulations.

The effect of vegetation on temporal stability of soil moisture was assessed using three sets of parameters (Table 3.2.3) and each of these was run for each distribution of k_s, yielding a total of 78 combinations of parameters for a soil layer. In the first set of parameters for the vegetation, root fraction in the soil layer (f_r) and LAI were considered uniform in the plot. The second and the third set of parameters were characterized by spatial variability in f_r and LAI, which were assumed to follow a normal distribution. Mean (μ_ξ) and standard deviation (σ_ξ) of LAI were fitted from observations (Section 3.2.5). In the third set of parameters LAI and f_r were assumed to have a positive linear correlation with k_s. To allow a comparison with observed soil moisture, a variability due to a measurement error (ε) was also accounted. Arrays of pseudo-random numbers whose elements were normally distributed (mean ≈ 0 and variance ≈ 1)

were generated at each time step and scaled by a constant of 0.03. Then, the random numbers were multiplied by the soil moisture values and added to the original soil moisture data.

Simulation parameters	**Homogeneous vegetation**	**Heterogeneous vegetation**	**Heterogeneous vegetation and correlated k_s, f_r and ξ**
θ_w	0.25ϕ	0.25ϕ	0.25ϕ
μ_ξ, σ_ξ	3.32, 0.0	3.32, 0.35	3.32, 0.35
c	0.55	0.55	0.55
μ_{f_r}, σ_{f_r}	0.75, 0.0	0.75, 0.15	0.75, 0.15
μ_{ρ_s} between k_s, f_r and ξ	0.0	0.0	0.9
c_1, c_2, c_3	0.5, 91, 213	0.5, 91, 213	0.5, 91, 213
ϵ	0.03	0.03	0.03

Table 3.2.3. Parameter values used in the simulations.

The model was applied at the daily time step from January 2013 to March 2014 (455 days in total), using local rainfall and potential evapotranspiration data (estimated by means of the Hargreaves method). The daily time step was preferred to the hourly time step to reduce computational times and because the average duration of the observed 24 rainfall events was larger than a day. In total 200 simulations were performed for each set of parameters.

In contrast to Teuling and Troch (2005), throughfall was not considered proportional to LAI. Throughfall amounts at each sampling site were modeled by a simple regression model, which relates throughfall to gross rainfall (Jackson, 1975). The spatial variability of throughfall was simulated drawing values of slopes, intercepts and inflexion point (parameters of the regression model used by Jackson (1975)) from normal distributions with a specific mean and standard deviation. The mean and the standard deviation of the slopes, the intercepts and the inflexion point were calibrated based on the percentiles (i.e., 5th, 10th, 25th, 50th, 75th, 90th and 95th) of the MRD and SDRD distributions obtained from throughfall observations (Fig. 3.2.11). Estimates of the simple linear regression (i.e., slope, intercept and coefficient of determination) computed between percentiles of the observed and simulated MRD and SDRD distributions were used to verify the adequacy of the parameters of the throughfall model to reproduce the observed temporal stability (Fig. 3.2.12. and 3.2.13).

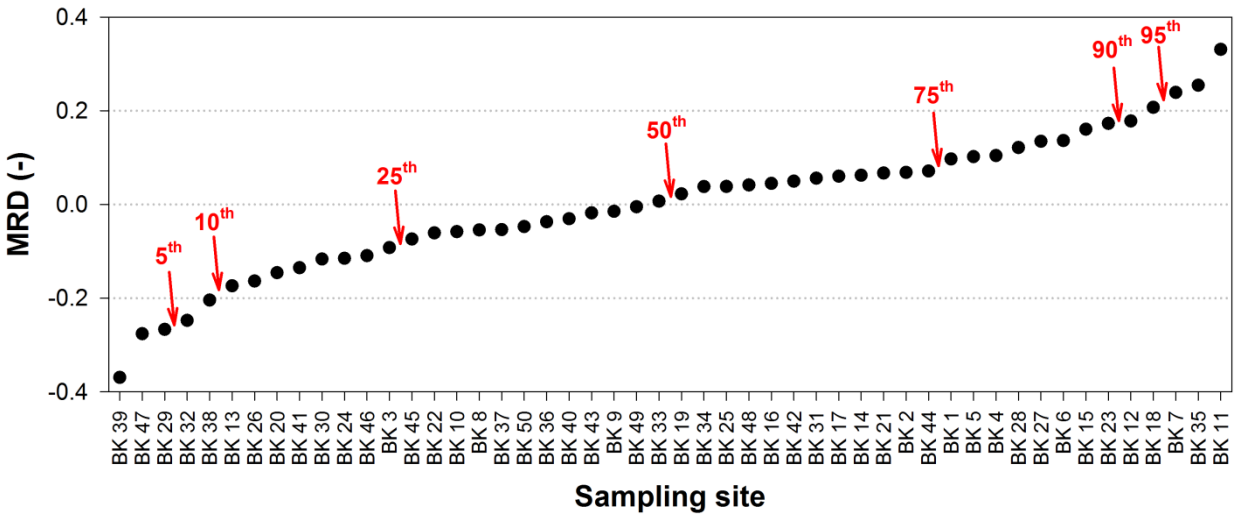

Fig. 3.2.11. Example of ranked MRD of throughfall measured by buckets (all 24 sampling times were considered) with indication of the percentiles of the distribution.

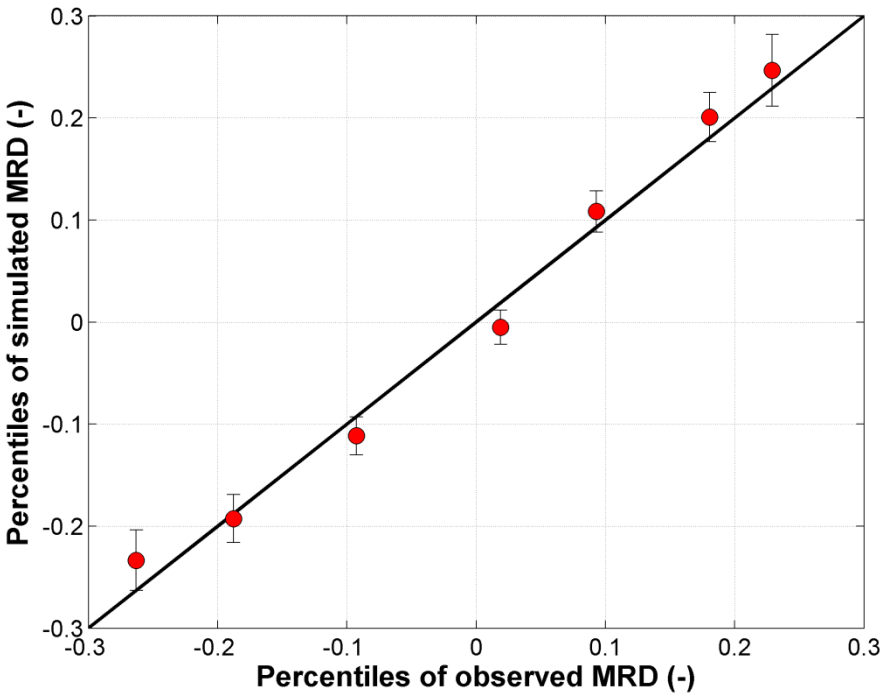

Fig. 3.2.12. Relation between percentiles (i.e., 5th, 10th, 25th, 50th, 75th, 90th and 95th) of the observed and the simulated MRD distributions of throughfall. The simulated values shown in the plot are the averages obtained from 200 simulations, while the error bars represent the standard deviations. The black solid line represents the 1:1 line.

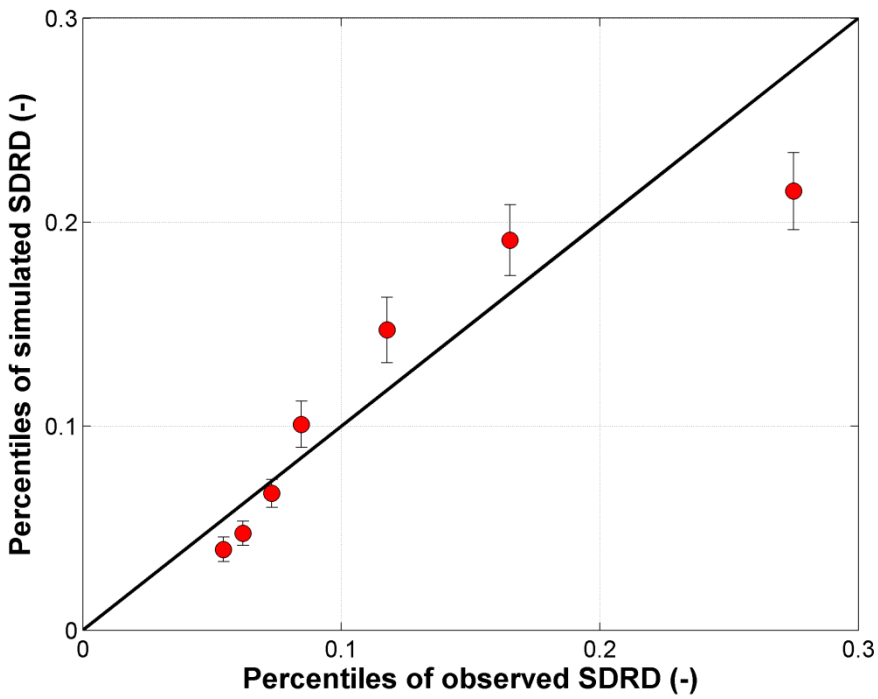

Fig. 3.2.13. Relation between percentiles (i.e., 5th, 10th, 25th, 50th, 75th, 90th and 95th) of the observed and the simulated SDRD distributions of throughfall. The simulated values shown in the plot are the averages obtained from 200 simulations, while the error bars represent the standard deviations. The black solid line represents the 1:1 line.

Percentiles of the observed MRD and SDRD distributions of soil moisture at 0-7 and 0-12 cm depth were used for comparison with the simulated MRD and SDRD distributions. Furthermore, the effects of k_s and vegetation parameters on the correlation between throughfall and soil moisture temporal stability were evaluated comparing the observed ρ_s with the distribution of the ρ_s obtained from the 200 simulations.

3.3. Quantification of subsurface connectivity in five headwater catchments

Subsurface connectivity was quantified in five catchments (Table 3.3.1) in the Italian Alps (Bridge Creek (BCC) and Larch Creek (LCC) catchment in the Dolomites; Penna et al., 2015a; Camporese et al., 2014) and the Swiss pre-Alps (C1, C2 and C3; Rinderer et al., 2014, 2015). The five catchments differ in area, elevation range, dominant geology, soil type and presence of a riparian zone. Groundwater levels were monitored by a network of piezometers (Fig. 3.3.1 and Table 3.3.2) installed with a different sampling design in the five catchments. We quantified the number of piezometers being activated during and between rainfall-runoff events. We defined a piezometer activation as the presence of water in the piezometers in BCC and LCC catchments or in the oxidized soil layer in the piezometers in C1, C2 and C3 catchments. We used a graph-theory approach (Blume and van Meerveld, 2015; Phillips et al., 2011) to quantify subsurface connectivity at the catchment or the hillslope scale. Directed graphs were drawn for each catchment (Fig. 3.3.1): the stream and the piezometers represented nodes, while connections (edges) between piezometers and between piezometers and the stream were established based on the main flow directions. We assumed that a piezometer was connected to the stream network whether *i)* it was active and *ii)* connected to the stream by an edge or a series of edges and active nodes. Individual nodes contributed to decrease connectivity when they became inactive and prevented active nodes to be connected to the stream network (gatekeepers in Table 3.3.2). A weight, based on the Thiessen polygon method, was assigned to each piezometer. Weights allowed for considering the spatial distribution of the piezometers and their representativeness at the catchment scale in C1, C2 and C3 catchments or at the hillslope scale in BCC and LCC catchments, and to determine the areas of the catchments that were connected to the stream. The degree of subsurface connectivity was quantified for each time step summing the weights of each piezometer connected to the stream network and multiplying by 100.

	Catchments				
	BCC	**LCC**	**C1**	**C2**	**C3**
Area (ha)	13.96	3.32	0.26	0.23	0.99
Mean precipitation (mm/yr)	1220	1220	2300	2300	2300
Mean temperature (°C/yr)	4.1	4.1	6.0	6.0	6.0
Elevation range (m a.s.l.)	1932-2515	1974-2128	1388-1425	1593-1650	1307-1388
Mean slope (°)	29.9	25.9	26.2	26.1	21.7
Mean exposure	South	East	West	West	Southwest
Dominant geology	Dolomite	Dolomite	Flysch	Flysch	Flysch
Soil type	Cambisol with mull	Cambisol with mull	Gleysol	Gleysol	Gleysol
Soil texture	Clay: 45-73% Silt: 16-28% Sand: 3-25%	Clay: up to 73% Silt: up to 28% Sand: up to 9%	Clay: 43-49 %, Silt: 42-46 % Sand: 5-15 %[2,3]	Clay: 43-49 %, Silt: 42-46 %, Sand: 5-15 %[2,3]	Clay: 43-49 %, Silt: 42-46 %, Sand: 5-15 %[2,3]
Land cover	grassland	grassland, sparse trees	light forest	grassland, sparse trees	grassland, light forest
Riparian zone (% of catchment area)	8.6	4.4	<1	0	<1
Permanently saturated areas	YES	YES	YES	YES	YES

Table 3.3.1. Main characteristics of the catchments.

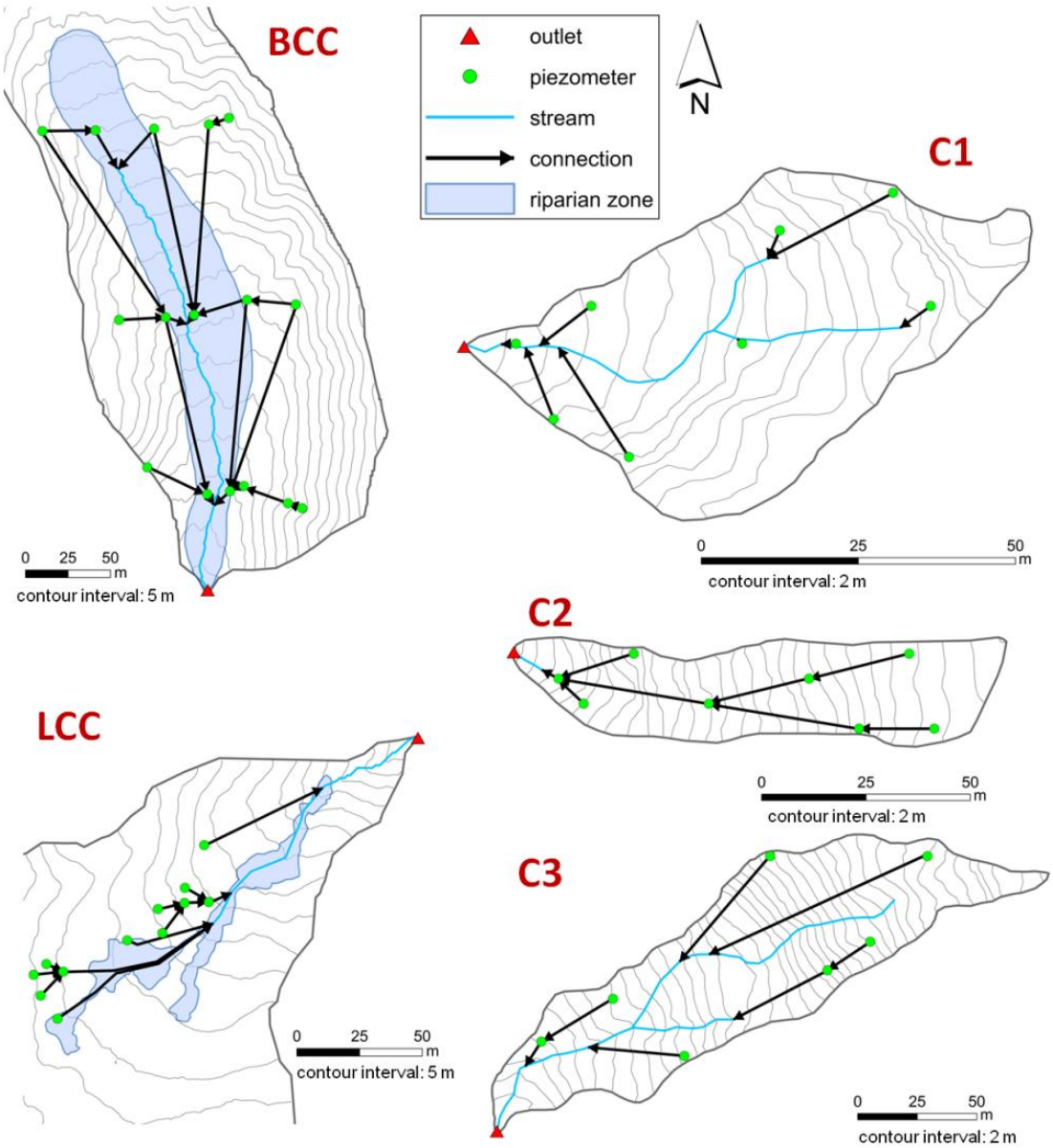

Fig. 3.3.1. Locations of the piezometers in the five catchments and directed graphs of piezometers-stream networks.

	Catchments				
	BCC	**LCC**	**C1**	**C2**	**C3**
Number of wells / number of connections to the stream	16/6	12/5	8/8	8/1	7/5
Number of nodes / number of edges	17/21	13/12	9/8	9/8	8/7
Potential gatekeepers	10	3	0	4	2
Gatekeepers	2	0	0	4	2
Mean weighted area (m^2) / standard deviation	2957/1175	399/237	330/209	285/119	1321/190
Median weighted area (m^2) / mean absolute deviation (m^2)	2546/933	354/188	317/166	252/101	1551/124

Table 3.3.2. Main characteristics of the connectivity network in the five catchments.

3.4. Development of a hysteresis index for hydrological variables at the runoff event timescale

3.4.1. Development of the index

The index is developed for hysteretic loops where the independent variable ($x(t)$) increases from its initial value, reaches a peak and then decreases. In hydrological applications, this is typically the case of streamflow, groundwater levels or soil moisture content, which increase during rainfall, snowmelt or glacier melt events and then decline. The dependent variable ($y(t)$) can increase or decrease during the event. It is assume that the evolution of the dependent variable is related to that of the independent variable. In the examples reported in Section 3.4.2 and Section 8, the relation between streamflow and other hydrological variables at the runoff event timescale is investigated, so that x is streamflow.

The index is based on the computation of definite integrals on the increasing and decreasing curve of the independent variable. The rising curve is defined as the part of the curve of the independent variable that goes from the initial value to its highest value, and the falling curve as the part of the curve of the independent variable that goes from the peak to the last observed value. The last observed value is used as loops do not always close (i.e., the variables do not always return to their initial state). We define eight main hysteresis classes: clockwise (classes: I and V), anti-clockwise (classes: IV and VIII), or eight-shaped (or more complex), where the main direction is clockwise (classes: II and VI) or anti-clockwise (classes: III and VII) (Table 3.4.1). Class I to IV describe the situation where the dependent variable increases during the rising curve of the independent variable, while classes V-VIII describe the situation where the dependent variable mainly decreases during the rising curve of the independent variable. If the dependent variable remains constant during the rising curve of the independent variable, then the classification of the loops is based on whether the dependent variable mainly increases or decreases during the falling curve. The hysteresis index is structured so that it can classify hysteretic loops into these eight classes.

Hysteresis class	Loop	Dependent variable	ΔA_{min}	ΔA_{max}	h
I	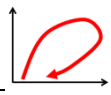	increase from the initial state	> 0	> 0	> 0
II	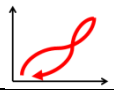	increase from the initial state	≤ 0	> 0	≥ 0
III	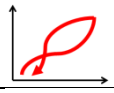	increase from the initial state	< 0	≥ 0	< 0
IV	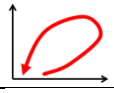	increase from the initial state	< 0	< 0	< 0
V	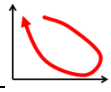	decrease from the initial state	> 0	> 0	> 0
VI	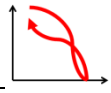	decrease from the initial state	≤ 0	> 0	≥ 0
VII	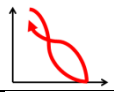	decrease from the initial state	< 0	≥ 0	< 0
VIII	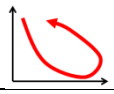	decrease from the initial state	< 0	< 0	< 0

Table 3.4.1. The eight main hysteresis classes for independent variables that increase from the initial state, reach a peak and then decrease, with the corresponding minimum (ΔA_{min}) and maximum (ΔA_{max}) values of the difference between the integrals $\Delta A_{[i,j]}$ (equation (3.4.5)) and their sum, h.

The computation of the hysteresis index involves four steps, which were implemented in MATLAB scripts (MathWorks, Inc., USA) and a stand-alone tool in Java:

1) Normalization of the two variables (columns a and b in Fig. 3.4.1), as:

$$u(t)=\frac{x(t)-x_{min}}{x_{max}-x_{min}} \tag{3.4.1}$$

$$v(t)=\frac{y(t)-y_{min}}{y_{max}-y_{min}} \tag{3.4.2}$$

where $x(t)$ and $y(t)$ are the two variables at time t, x_{min}, x_{max}, y_{min} and y_{max} are the minimum and maximum values of the independent and dependent variables, respectively, and $u(t)$ and $v(t)$ are the normalized values of $x(t)$ and $y(t)$, respectively. The two normalized variables range between 0 and 1. Typically, x_{min} should be the independent variable at its initial state, so that normally $u(0) = 0$.

2) Computation of the definite integrals, $A_{r[i,j]}$ and $A_{f[i,j]}$ of the functions $v_r(u)$ and $v_f(u)$ on intervals $[i,j]$ for the rising (r) and the falling (f) curve, as:

$$A_{r[i,j]} = \int_i^j v_r(u)du \tag{3.4.3}$$

$$A_{f[i,j]} = \int_i^j v_f(u)du \tag{3.4.4}$$

where i and j represent the lower and upper limit of integration, respectively, and can assume all the values from $u = 0$ to $u = 1$. The integrals can be computed on intervals of different widths delimited by selected points, i and j, of the independent variable u (column c and d in Fig. 3.4.1). The choice of the intervals of integrations should depend on the quality and resolution of the data and the rate at which the dependent variable changes with respect to the independent variable. In the examples in Section 3.4.2, we computed 17 integrals of equal width (intervals of 0.05 from $u = 0.15$ to $u = 1$) for the rising and for the falling curve, using a linear function.

The definite integrals for the rising and the falling curves can be plotted as a function of u (column d in Fig. 3.4.1). For clockwise loops the integrals of the rising curve are always larger than the integrals of the falling curve (Fig. 3.4.1 column d, hysteresis class I), for anti-clockwise loops the integrals of the falling curve are always larger than those of the rising curve (Fig. 3.4.1 column d, hysteresis class IV), while for eight-shaped or other complex hysteretic loops the integrals of the two curves cross (i.e., some integrals of the rising curve are larger than those on the falling curve, while others are smaller than those of the falling curve; Fig. 3.4.1 column d, hysteresis class II and III).

3) Determination of the difference between the definite integrals on the rising and the falling curve computed for the same interval, $[i, j]$, as:

$$\Delta A_{[i,j]} = A_{r[i,j]} - A_{f[i,j]} \tag{3.4.5}$$

Clockwise loops have all $\Delta A_{[i,j]} > 0$, anti-clockwise loops have all $\Delta A_{[i,j]} < 0$, linear relations (no hysteresis) have all $\Delta A_{[i,j]} = 0$, while eight-shaped hysteretic patterns are characterized by $\Delta A_{min} < 0$ and $\Delta A_{max} > 0$ (column e in Fig. 3.4.1 and Table 3.4.1), where ΔA_{min} and ΔA_{max} are the minimum and maximum value of $\Delta A_{[i,j]}$, respectively.

4) Quantification of the h index, as:

$$h = \sum_{k=1}^{n} \Delta A_{[i,j]} \tag{3.4.6}$$

where n is the number of intervals ($n = 17$ in the examples in Section 3.4.2).

Clockwise hysteresis is characterized by $h > 0$, anti-clockwise loops have $h < 0$, while $h \approx 0$ indicates no hysteresis or a symmetrical eight-shaped or complex loop (Table 3.4.1). For complex eight-shaped loops, the dominant direction is defined by the relative size of the two (or more) loops. The value of the index is also a measure of the size of the hysteretic loop: the larger the hysteretic loop, the further h is from 0.

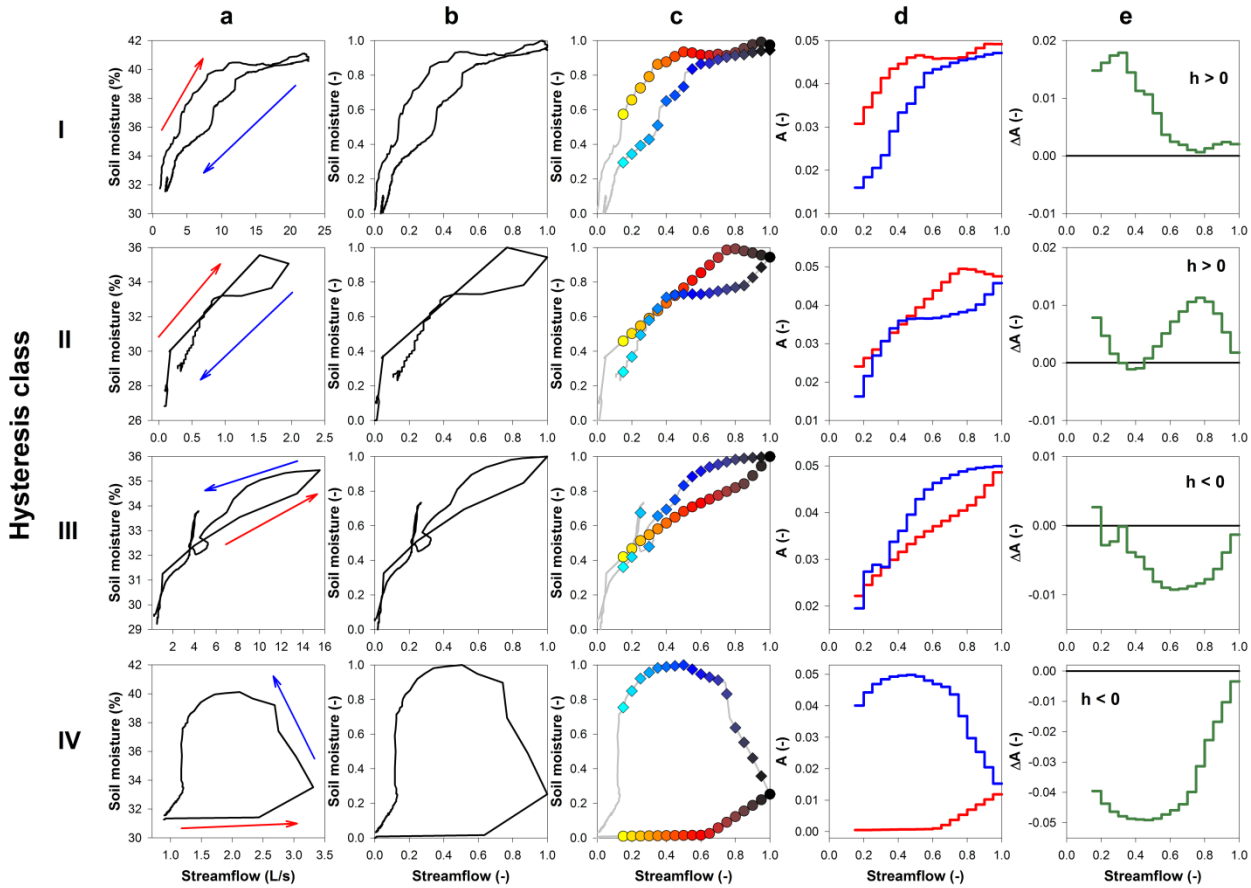

Fig. 3.4.1. Examples of hysteretic relations between streamflow and soil moisture representing the four main hysteresis classes where the dependent variable increases during an event (column *a*) and the main steps in the computation of the hysteresis index (columns *b*-*e*). The circles and diamonds in column *c* represent the selected points (u) delimiting the intervals of integration on the rising and the falling limb, respectively. The symbol colors change from yellow to dark red to cyan during a runoff event. The horizontal black line in column *e* represents $\Delta A = 0$.

3.4.2. Instrumentation and datasets used to test the hysteresis index

The hysteresis index was tested with hydrological data from three experimental catchments in Italy (Fig. 3.4.2). The index was applied to the hysteretic relation between streamflow and four typical runoff response variables: soil moisture, depth to water table, isotopic composition of stream water (δ^2H) and electrical conductivity (EC) of stream water (Fig. 3.4.3). These variables were chosen because *i)* they show different responses during rainfall and snowmelt events (soil moisture and groundwater level typically increase during the event, EC usually decreases, while the stream water isotopic composition can increase or decrease depending on the isotopic signature of the rain or snowmelt); *ii)* they have different signs (soil moisture and EC are positive, whereas isotopic composition is generally a negative number, and groundwater level can be positive, water level above the bottom of the well, or negative, distance from the

surface); and *iii)* previous studies have shown hysteretic relation with streamflow (Penna et al., 2011; McGlynn et al., 2004; Wetzel, 2003).

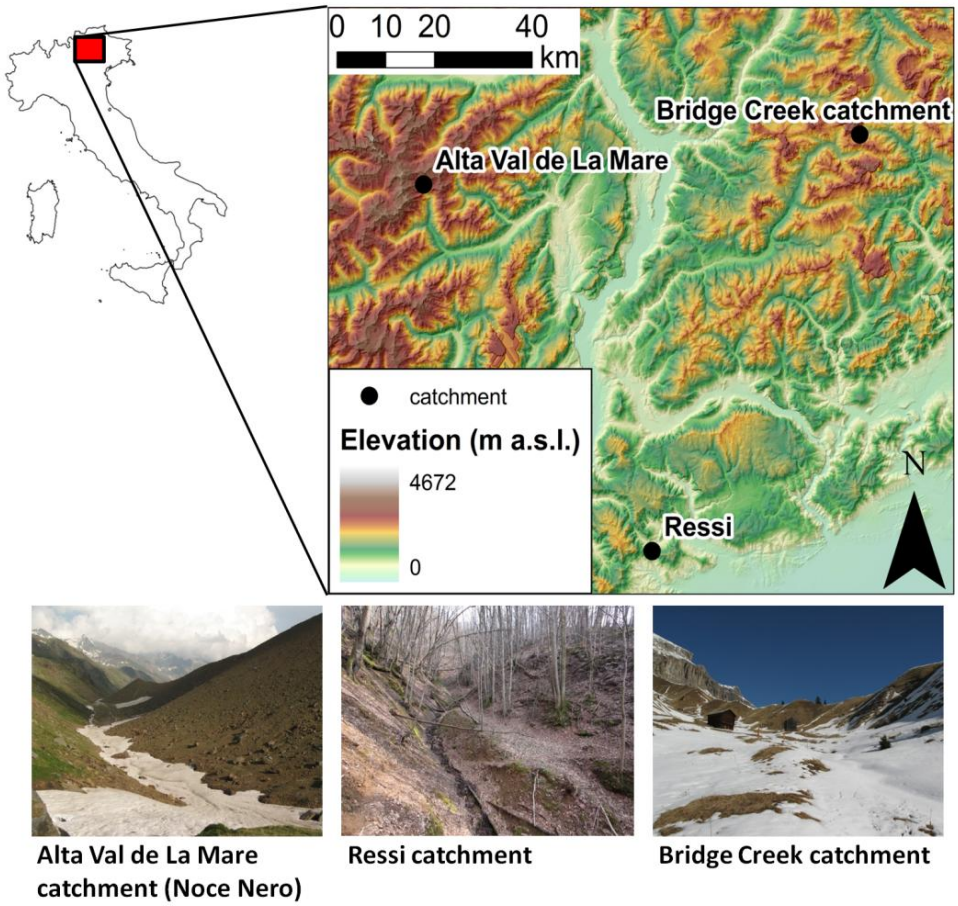

Fig. 3.4.2. Location of Alta Val de La Mare, Ressi and Bridge Creek catchment in Italy.

In order to apply the hysteresis index to the field data (Fig. 3.4.3) we selected equal intervals of 0.05 from $u = 0.15$ to $u = 1$ on the rising and the falling curve. The number of selected intervals represents a reasonable frequency for the applications, leaving out possible noise for low flow observations ($u < 0.15$). The use of different intervals did not change the results. Linear interpolation between two observations was used to determine the corresponding values of the dependent variable, $v(u)$ when data for the dependent variable at the selected times of u were missing in the dataset (i.e., the time stamp of the two datasets was not exactly the same).

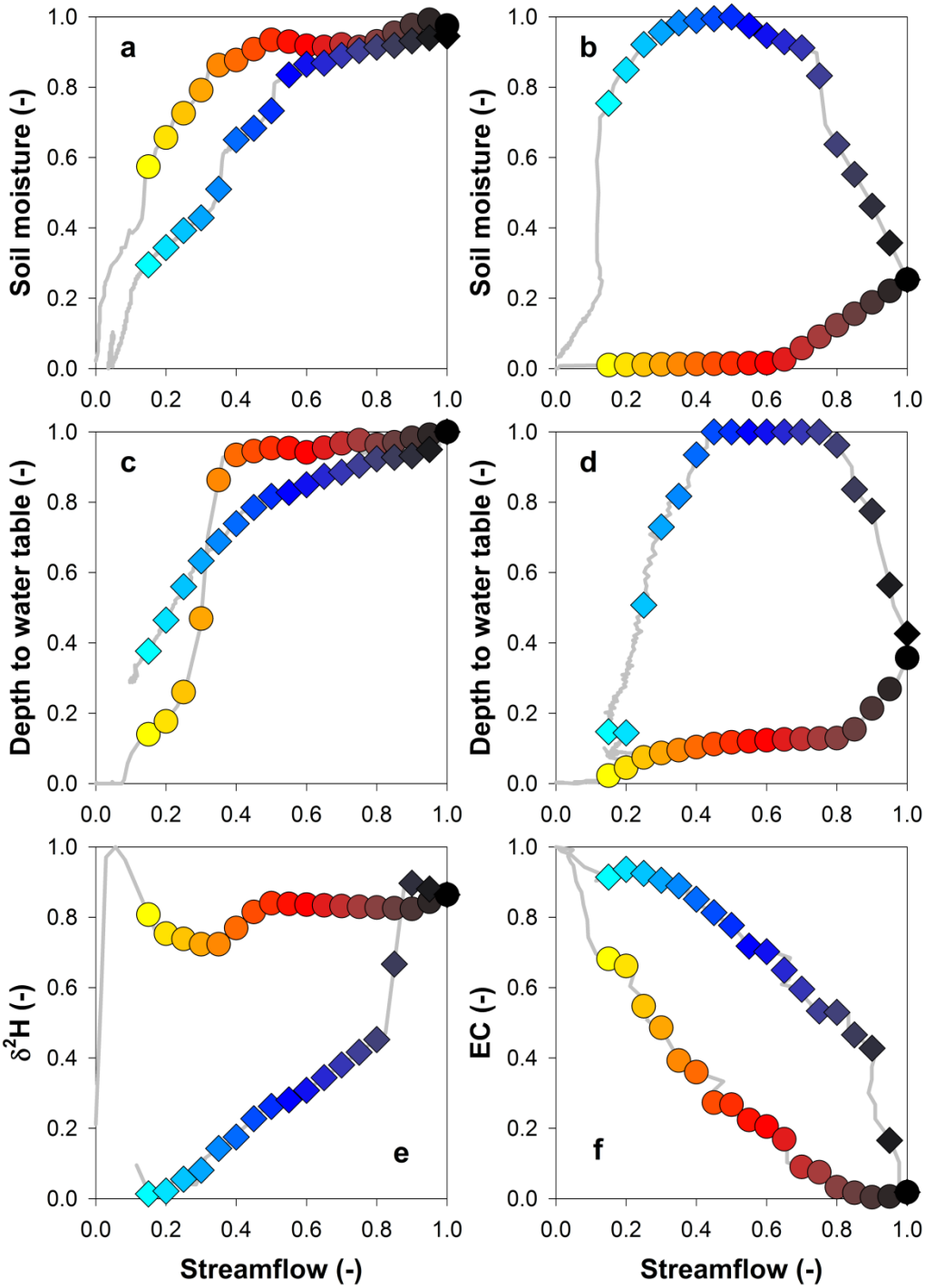

Fig. 3.4.3. Normalized hysteretic loops between streamflow and soil moisture in the Ressi catchment (*a*: clockwise; *b*: anti-clockwise), depth to water table in a piezometer in the Bridge Creek catchment (*c*: eight-shaped; *d*: anti-clockwise), δ^2H in the Ressi catchment (*e*: eight-shaped), and EC in the Alta Val de La Mare catchment (*f*: anti-clockwise). Values of ΔA_{min}, ΔA_{max} and h are reported in Table 8.2.1. Circles and diamonds represent selected points delimiting the 0.05 intervals of integration on the rising and the falling curve, respectively. The symbol colors change from yellow to dark red to cyan during a runoff event. See Fig. 3.4.4 for the time series.

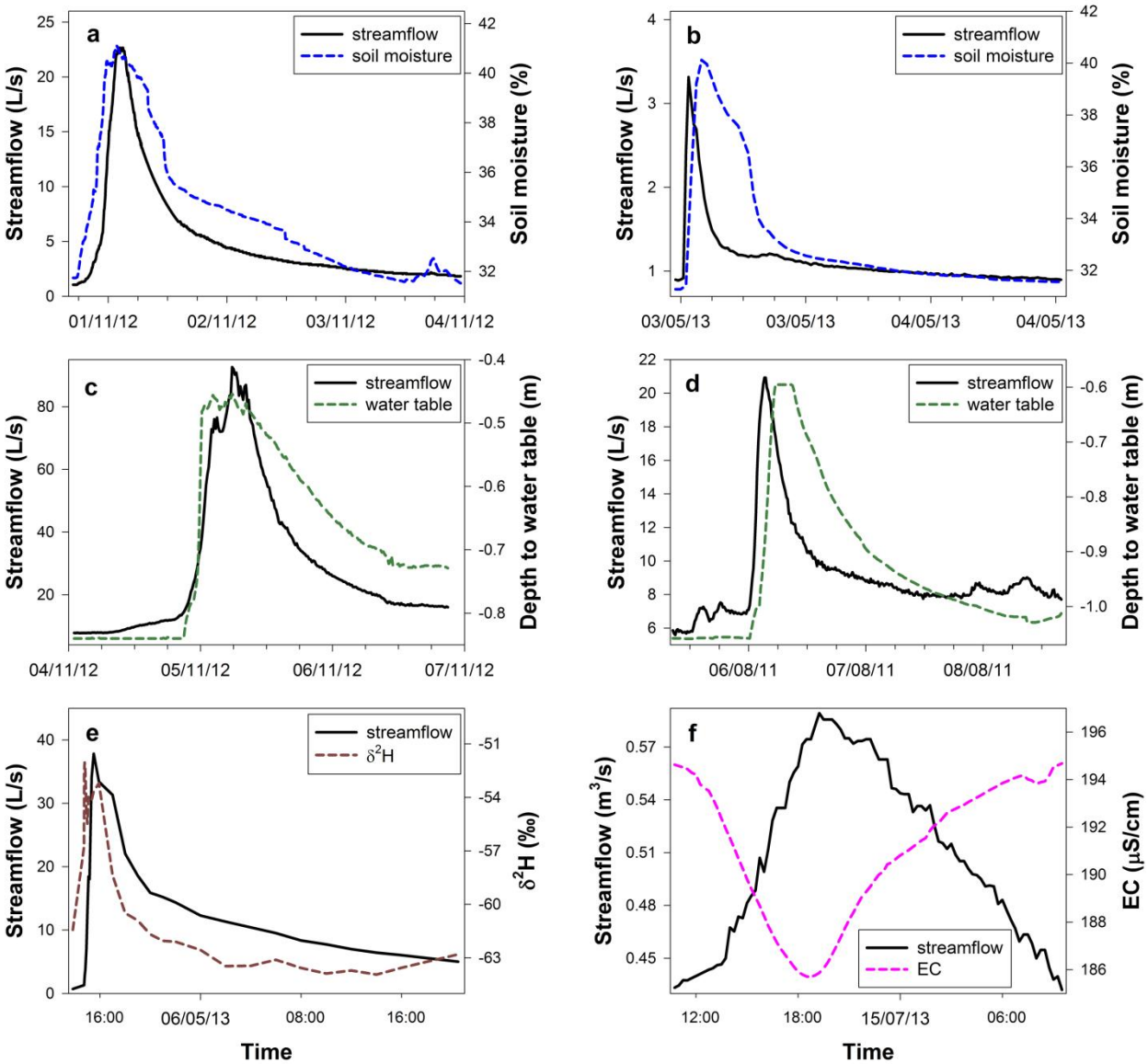

Fig. 3.4.4. Time series of streamflow, soil moisture (a, b), depth to water table (c, d), δ^2H of streamwater (e) and stream water EC (f) for the hysteretic loops shown in Fig. 3.4.3.

Ressi catchment

For the application of the hysteresis index on field data, soil moisture and streamflow data from the Ressi catchment were used (Section 3.2.1). 30 rainfall-runoff events (event total precipitation larger than 10 mm) between August 2012 and July 2013 were analyzed (Penna et al., 2015b). Precipitation amount ranged between 11.8 and 266.2 mm, while event-average rainfall intensity varied between 2.0 and 11.1 mm/hr. Soil moisture was measured at 0-30 cm depth by the four time domain reflectometers installed at different positions along the hillslope-riparian zone transect. Soil moisture was measured at a 5-min interval from mid August 2012 until the end of November 2012, when the resolution was changed to 10 minutes. The increase in streamflow (i.e., the difference between the minimum and maximum

streamflow during an event) varied between 0.4 and 63.1 L/s for the 30 rainfall-runoff events. Because of the fast streamflow response, the rainfall-runoff events were analyzed using a 5-min resolution data for both streamflow and soil moisture. Therefore, a linear interpolation was used to estimate soil moisture at 5-min intervals from December 2012 to July 2013, when 5-min time resolution data were not available (17 out of the 30 events). We used the streamflow-soil moisture relation (Fig. 3.4.3a, b) to evaluate the temporal variability of h, as well as the classification of the hysteretic loops (Table 3.4.1), and their relation to event characteristics (e.g., average and maximum rainfall intensity, rainfall depth and runoff coefficient) and the antecedent soil moisture index (ASI):

$$ASI = \theta \times D \tag{3.4.7}$$

where θ is the volumetric soil moisture content (m^3/m^3) measured by each probe and D is the installation depth (0.3 m) (Haga et al., 2005; Detty and McGuire, 2010a, b). The correlation between the hysteresis index and the rainfall event characteristics was assessed using the Spearman rank correlation analysis (ρ_s).

In addition to the soil moisture data, the index was tested for the hysteretic relation between streamflow and the isotopic composition of stream water during a 50-mm rainfall event on 05/05/2013 (Fig. 3.4.3e). Additional information on water sampling and determination of the isotopic composition can be found in Penna et al. (2015b).

Bridge Creek catchment

Figures 3.4.3c shows the hysteretic relation between streamflow and depth to water table measured with a pressure transducer in a piezometer on a hillslope during a 49-mm rain-on-snow event on 04/11/2012 at the Bridge Creek catchment (BCC, 46°29’32.34’’ N, 11°50’38.66’’ E; Eastern Italian Alps). Figure 3.4.3d shows the hysteretic relation between streamflow and depth to water table in a different piezometer (125 m away) measured with a capacitance sensor during a 20-mm rainfall event on 05/08/2011. Stream stage at BCC was measured behind a V-notch weir with a pressure transducer. Streamflow was obtained by the weir equation, which was checked with bucket measurements. All data were collected at a 15-min interval. Information on the catchment and a detailed description of the groundwater responses can be found in Penna et al. (2011; 2015a).

Alta Val de La Mare catchment

Figure 3.4.3f shows the hysteretic relation between streamflow and stream water EC for a snowmelt event in the Noce Nero, a stream fed by snowmelt and spring water (Alta Val de La

Mare catchment, 46°24’51.30’’ N, 10°40’50.90’’ E; Eastern Italian Alps, Carturan et al., 2012). Stream stage and EC were measured at a 15-min interval by a Dipper-PTEC (SEBA Hydrometrie GmbH & Co., Germany) multi-parameter sensor. Streamflow was measured during different flow conditions using the salt dilution method.

4. ANALYSIS AND MODELING SOIL MOISTURE SPATIAL VARIABILITY AT THE PLOT SCALE

4.1. Observed soil moisture variability

Due to the varying temporal sampling over the three years, there was a different availability of daily soil moisture data. Table 4.1.1 summarizes the main characteristics of the observed data, including the averages of the spatial means and standard deviations. Inspection of the data shows that mean soil moisture was larger for vineyard than for the meadow at both depths (Fig. 4.1.1 and Table 4.1.1); correspondingly, the average of the spatial variability of soil moisture (expressed by the standard deviation) was larger for the meadow than for the vineyard. This is consistent with earlier observations (Penna et al., 2009, 2013) and indicates that the variability of soil moisture distributions decreases when the mean soil moisture value increases. As expected, soil moisture increased quite fast after a rainfall pulse especially at the shallow layer and mean soil moisture was larger during the winter period (Fig. 4.1.1).

Summary statistics	**Meadow**		**Vineyard**	
Depth (cm)	**0-30**	**0-60**	**0-30**	**0-60**
Sampling points	9	8	12	11
Sampling times	650	681	700	670
Mean (%)	12.9	14.4	16.2	15.6
Mean of standard deviation (%)	1.2	0.8	1.0	1.3

Table 4.1.1. Summary of soil moisture statistics over the two land uses for 2006-2008 (only common sampling times are considered).

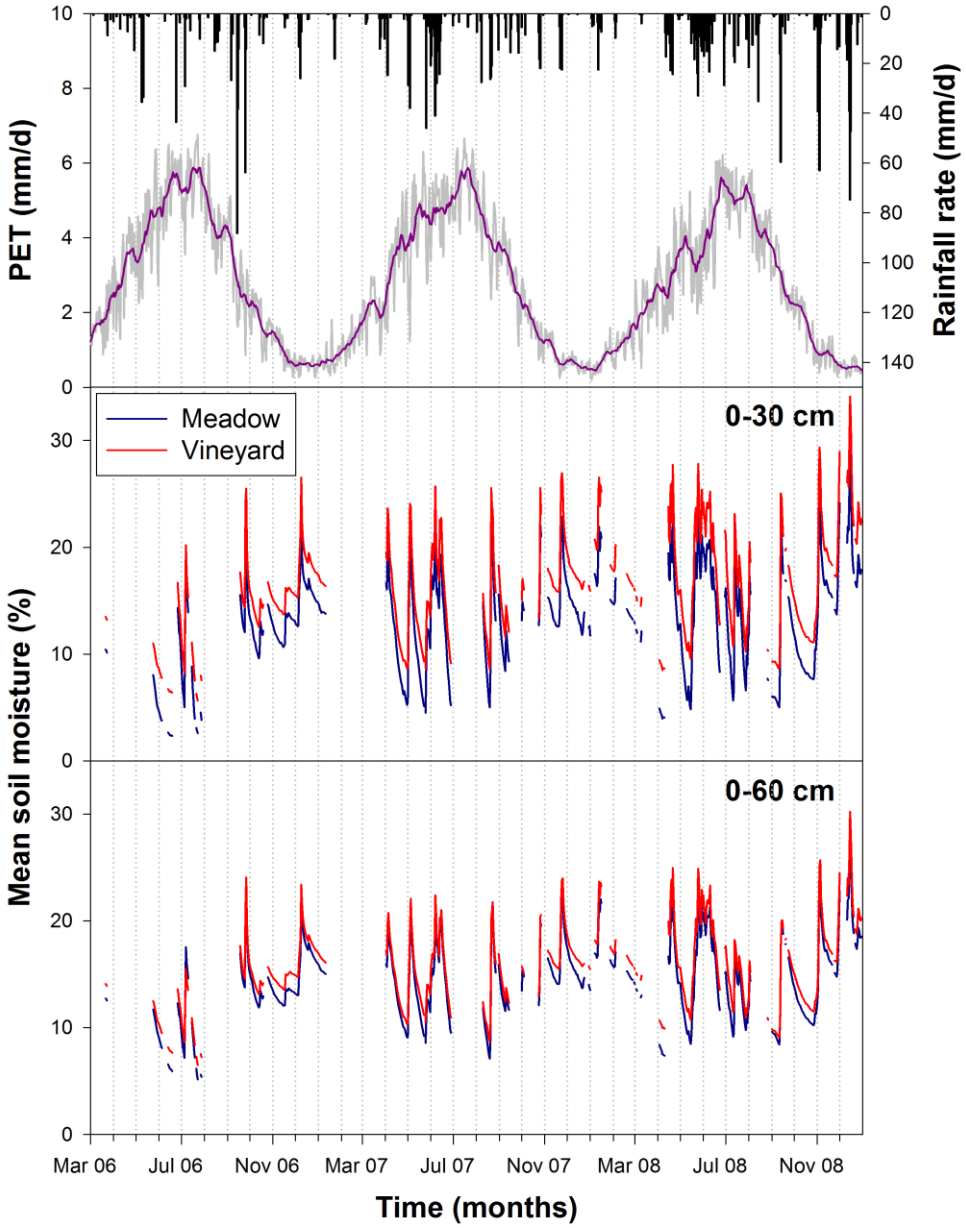

Fig. 4.1.1. Time series of spatial mean soil moisture, rainfall and potential evapotranspiration (PET). The purple line in the upper plot is the moving average of PET.

Figure 4.1.2 and 4.1.3 show the distributions of soil moisture spatial statistics: spatial mean and spatial standard deviation for the three years. The statistics are reported for the growing (from April to September) and for the dormant season (from October to March) at 0-30 and 0-60 cm depth. Consistently with the observations reported in Table 4.1.1, the mean spatial soil moisture was significantly (Mann-Whitney test $p < 0.001$) larger in the vineyard than in the meadow for both seasons and at both depths. Not surprisingly, the spatial variability of soil moisture was significantly (Mann-Whitney test $p < 0.001$) larger for the meadow than for the vineyard for both seasons at 0-30 cm depth (Fig. 4.1.3). Particularly, the standard deviation in the vineyard is much larger for the growing period than for the dormant period, implying the

effect of the plant growth during the growing season. On the other hand, the spatial standard deviation of soil moisture was found larger in the vineyard than in the meadow at 0-60 cm depth, likely due to an increased heterogeneity in the deeper soil layers.

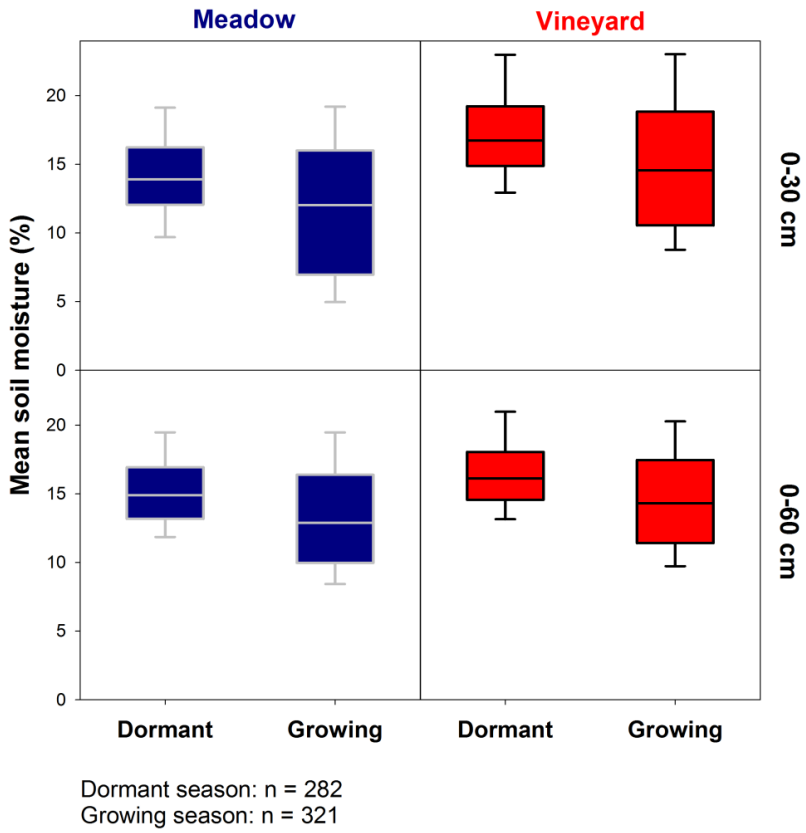

Fig. 4.1.2. Boxplots of the spatial mean soil moisture for 2006-2008. The statistics are reported for the meadow and the vineyard at both depths, for the growing season (April to September) and the dormant season (October to March). The boxes indicate the 25th and 75th percentile, the whiskers indicate the 10th and 90th percentile, the horizontal line within the box marks the median.

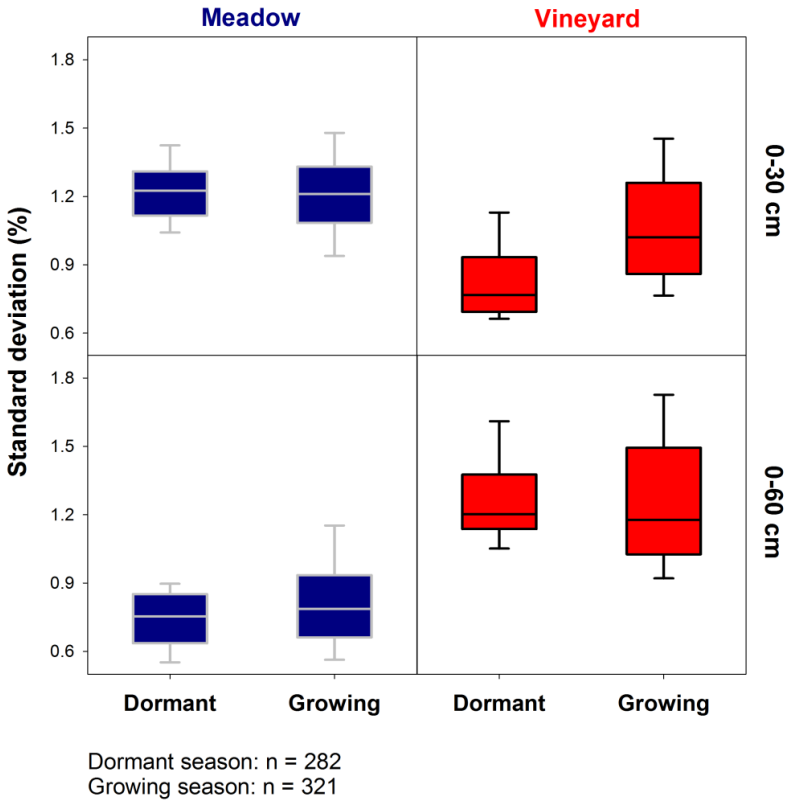

Fig. 4.1.3. Boxplots of the spatial standard deviation of soil moisture for 2006-2008. The statistics are reported for the meadow and the vineyard at both depths, for the growing season (April to September) and the dormant season (October to March). The boxes indicate the 25th and 75th percentile, the whiskers indicate the 10th and 90th percentile, the horizontal line within the box marks the median.

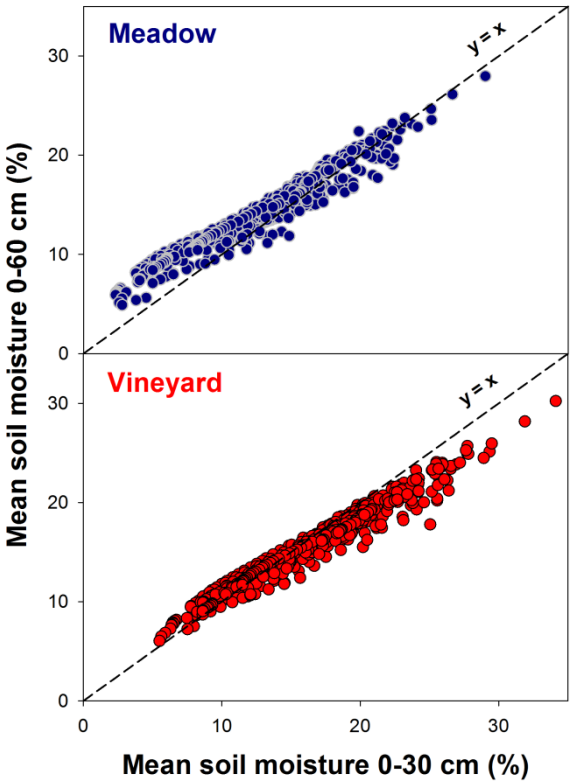

Fig. 4.1.4. Relation between the spatial mean soil moisture at 0-30 cm and at 0-60 cm depth.

The spatial mean soil moisture was significantly correlated between the two soil depths (0-30 and 0-60 cm depth), but during dry conditions soil moisture was higher at the deeper layer compared to the shallow one, probably due to the evaporation processes affecting most soil moisture at the soil surface (Fig. 4.1.4).

Figure 4.1.5 shows that the coefficient of variation decreased when the mean soil moisture value increased (Penna et al., 2009, 2013). As expected, the coefficients of variation were larger during days characterized by high evapotranspiration, underlining the role of the seasonal growth of the vegetation.

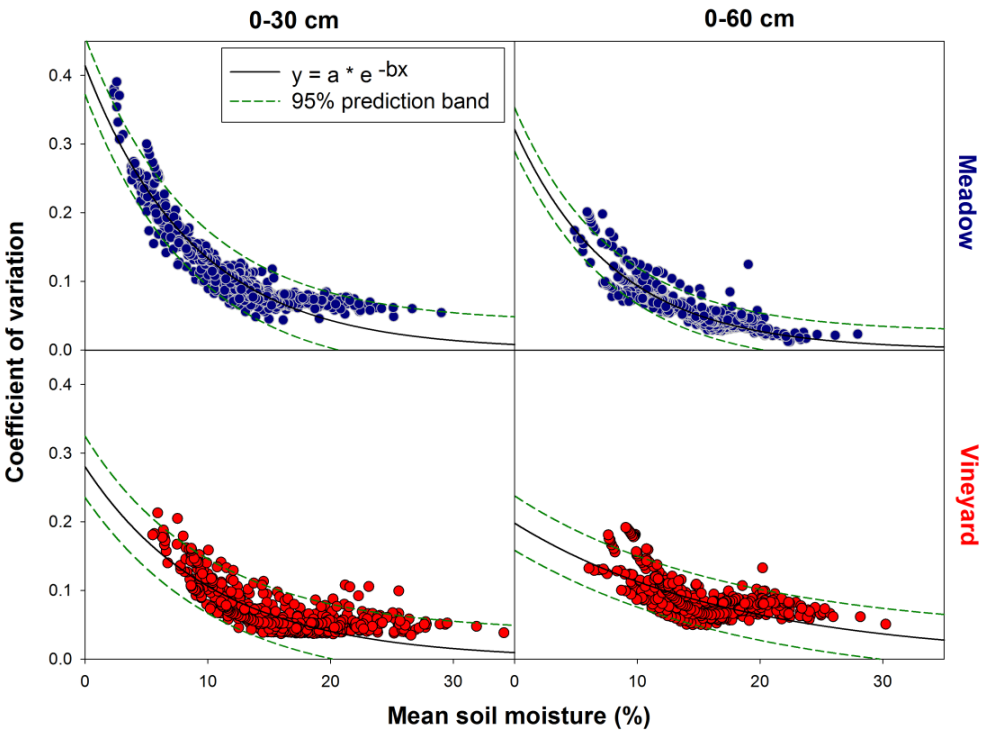

Fig. 4.1.5. Relation between the spatial mean soil moisture and the coefficient of variation.

4.2. Modeling soil moisture spatial variability

Table 4.2.1 reports the values for the calibration and the verification periods for the meadow and the vineyards at 0-30 cm depth, obtained by the application of the soil moisture model described in Section 3.1.2. The values show a good predictive capability of the model, particularly when considering that 2008 was much wetter than the other two years. The parameters identified by means of the calibration process are reported in Table 4.2.2, showing a good correspondence with similar parameters obtained in the model application exercise described in previous works (Baudena et al., 2012). The comparison between the time series of simulated and observed daily values is reported for the year 2008, showing both good

simulation performances (particularly during the spring and fall months) and less good modeling capability in the late summer season for the meadow site (Fig. 4.2.1).

	Meadow			Vineyard		
	2006	**2007**	**2008**	**2006**	**2007**	**2008**
NS	0.80	0.52	0.74	0.82	0.65	0.72
RMSE	2.05	2.77	2.60	1.78	2.37	2.77

Table 4.2.1. Indexes of performance between observed and simulated mean soil moisture data. NS: Nash-Sutcliffe efficiency index; RMSE: Root Mean Square Error.

Simulation parameters	Meadow	Vineyard
μ_{k_s}, σ_{k_s}	8.6, 0.32	7.8, 0.40
θ_w	0.19ϕ	0.25ϕ
θ_c	0.22ϕ	0.31ϕ
μ_ξ, σ_ξ	1.6, 0.1	3.5, 0.6
c	0.55	0.55
f_r	0.8	0.8
c_1, c_2, c_3	0.5, 1, 260	0.5, 60, 260

Table 4.2.2. Parameter values used in the simulation.

In Table 4.2.2 μ_{k_s} and σ_{k_s} are mean and standard deviation for spatial distribution of $ln(k_s)$, ϕ represents porosity, θ_w is the wilting point, θ_c is critical moisture content, μ_ξ, σ_ξ are mean and standard deviation for spatial distribution of LAI at its maximum (ξ_{max}), c is a light use efficiency parameter, f_r is root fraction in the layer of depth L ($L = 0.3\ m$) and c_1, c_2, c_3 are parameters that specify the seasonal development of LAI.

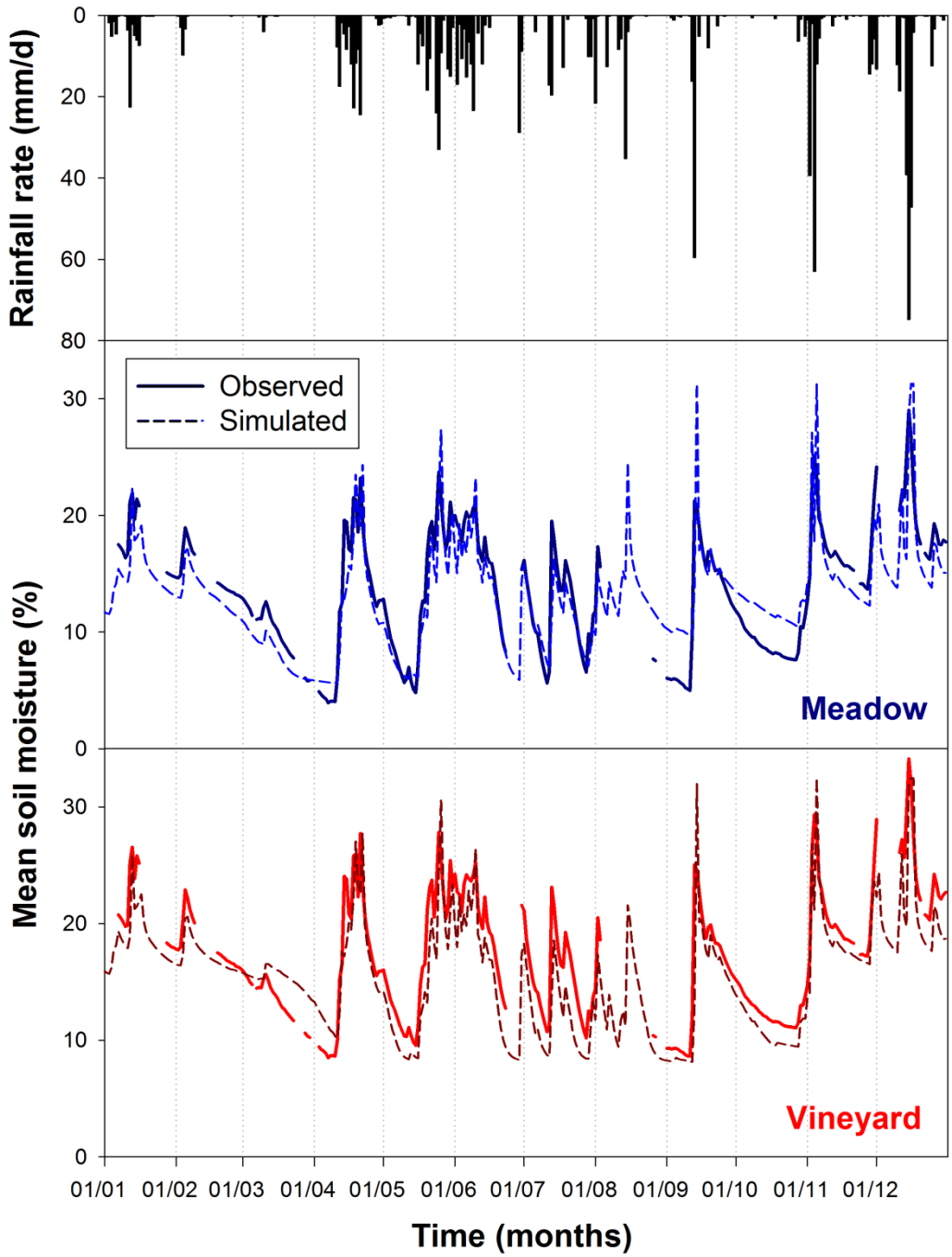

Fig. 4.2.1. Time series of rainfall and spatial mean soil moisture for the year 2008 for (a) meadow and (b) vineyard at 0-30 cm depth.

Table 4.2.3 reports the comparison between simulated and observed average values of soil moisture spatial statistics, for both meadow and vineyard. Inspection of these statistics shows that the model reproduces well the spatial statistics in the two sites.

A more complete representation of the distribution of both the spatial mean values and the spatial standard deviation is reported in Fig. 4.2.2, corresponding to the period June-September 2008. The simulated mean soil moisture reproduces well the observations, for both the

meadow and the vineyard. The simulation of the distribution of the spatial standard deviation captures the main differences between the two land uses, with a lower standard deviation for the vineyard than for the meadow. However, the ranges of the values are not well reproduced.

		Meadow			Vineyard		
		2006	2007	2008	2006	2007	2008
No. of sampling times		150	205	291	150	205	291
Mean (%)	**Observed**	11.6	12.9	13.5	14.4	15.8	17.2
	Simulated	12.0	13.1	13.1	15.0	15.2	15.7
Mean of standard deviation (%)	**Observed**	1.1	1.2	1.3	0.9	1.0	1.0
	Simulated	1.2	1.2	1.3	0.9	0.9	1.0

Table 4.2.3. Summary of soil moisture statistics over the two land uses (0-30 cm depth) for 2006-2008.

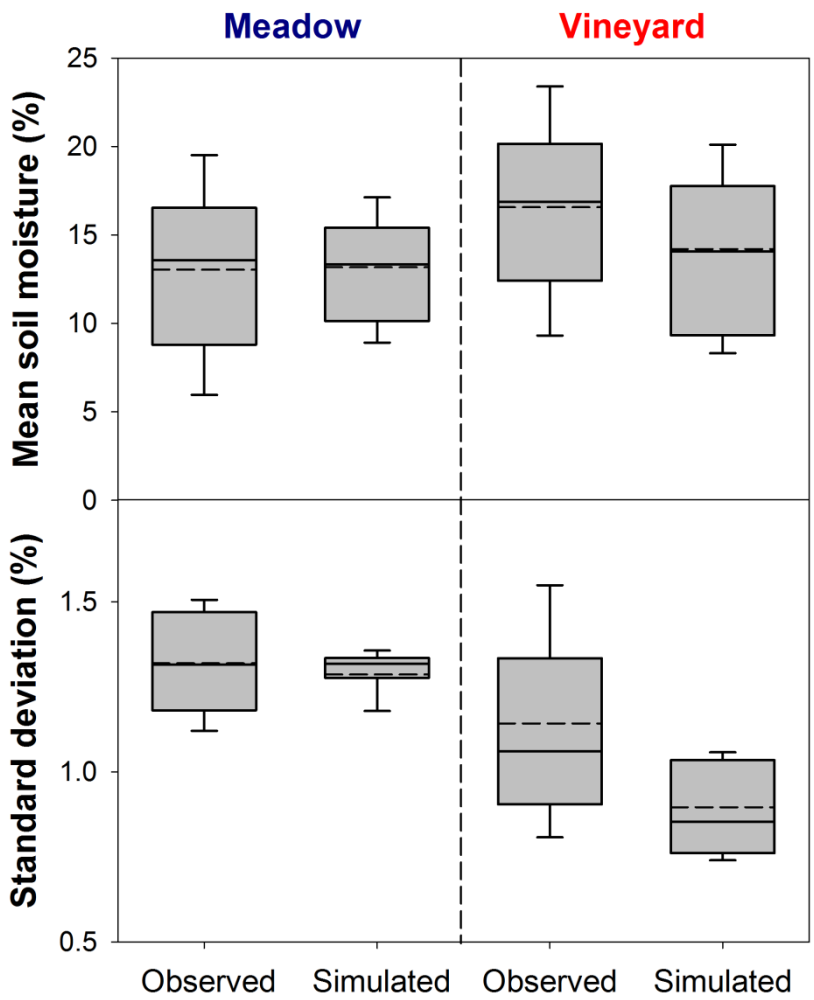

Fig. 4.2.2. Boxplots of the spatial mean soil moisture and standard deviation for the period June-September in 2008. The boxes indicate the 25th and 75th percentile, the whiskers indicate the 10th and 90th percentile, the horizontal line within the box marks the median and the dash line marks the mean.

While the results reported so far show that there are limitations in the model capability in reproducing the fine characteristics of the distribution of the spatial standard deviation, the model seems to be adequate to summarize the main differences between the two types of vegetation.

5. COMPARING TWO DIFFERENT TYPES OF THROUGHFALL COLLECTORS

Comparing the differences in throughfall means measured by buckets and rain gauges (Section 3.2.2) a significant difference ($\alpha = 0.05$) was found for only two measurements in fall, when beech and chestnut usually shed their leaves (31/10/2013 and 11/11/2013; Fig. 5.1). A negative difference in mean throughfall (i.e., a larger mean throughfall for the rain gauges than for the buckets) was detected for 15 of the 21 sampling times, likely due to the different number of dripping points detected by the buckets and rain gauges. Indeed, the difference between the 90th percentile of throughfall (that includes the dripping points) measured by buckets and rain gauges ranged between 0.6% and -26.3% (mean: -10.9%). The difference between the throughfall means appeared to be independent from the gross rainfall amount. The non-significant difference in mean throughfall indicates that the arrangement of the collectors (sample size, collecting area and spatial distribution) was sufficient and did not affect mean throughfall measured in the study plot. The assessment of the optimum sample size for each measurement day showed that the number of collectors required to measure throughfall within 10% of the mean with a 95% confidence interval ranged between 9 and 36 for buckets and between 12 and 185 for rain gauges (Fig. 5.2). These optimum sample sizes indicated that the number of required buckets was smaller than the number of samplers deployed in the field (n = 50) but that more rain gauges were needed to determine throughfall during small rainfall events. As expected, the optimum sample sizes (y) decreased with increasing gross rainfall (x) (Fig. 3) following an exponential decay relation ($y = 23.98 * e^{-0.015*x}$, R^2 = 0.28, n = 21 for buckets; $y = 233.11 * e^{-0.106*x}$, R^2 = 0.52, n = 21 for rain gauges) because the spatial variability of throughfall decreased with increasing gross rainfall. There was a significant negative correlation between gross rainfall and the 95% confidence interval (Spearman's ρ_s = -0.51, $p < 0.05$, n = 21).

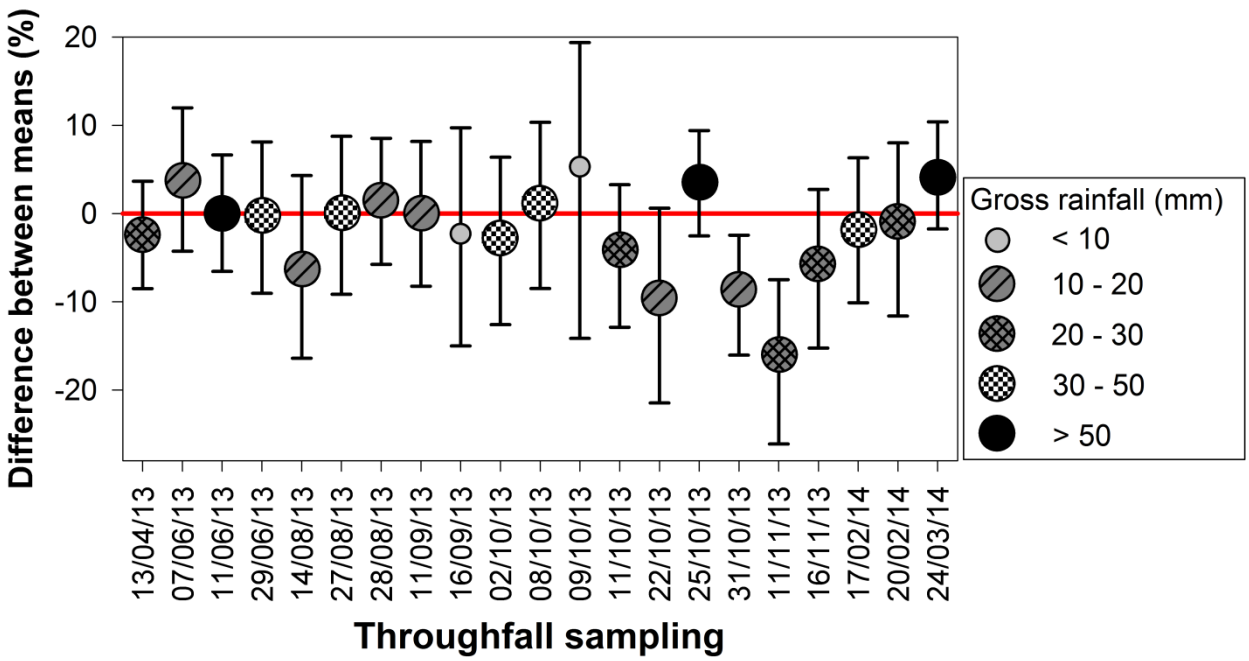

Fig. 5.1. Difference between mean throughfall measured by the buckets and rain gauges for the 21 measurements. Means and 95% confidence intervals were computed after application of the bootstrapping re-sampling method. The differences between the two means are significant when the confidence intervals do not intersect zero (red solid line). A positive difference between the means indicates that the buckets collected more throughfall than the rain gauges.

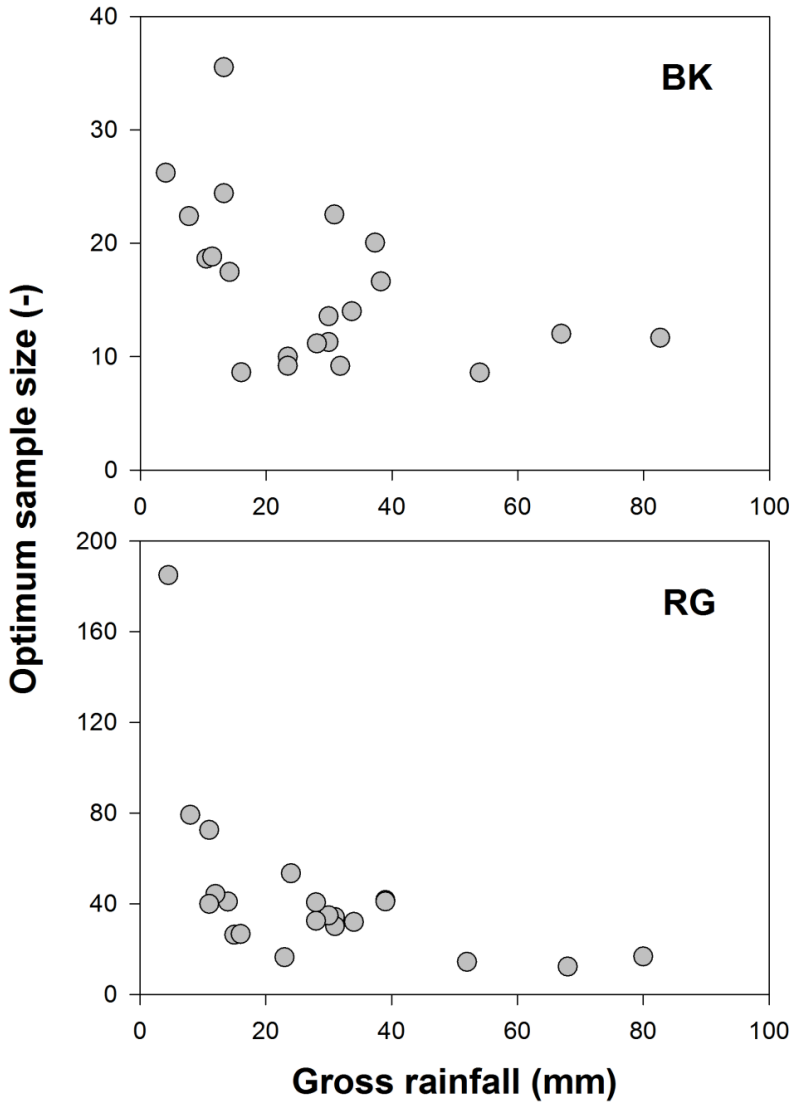

Fig. 5.2. The relation between gross rainfall and optimum sample size computed for buckets (BK) and rain gauges (RG).

The observed spatial variability in throughfall was larger for the rain gauges than the buckets (Fig. 5.3). This difference in the observed spatial variability was probably related to the difference in the area of the two collectors: buckets have a larger collecting area than rain gauges, thus they integrate more small scale variability and consequently the variability between individual measurement locations is smaller. The difference between the standard errors of throughfall measured by the buckets and rain gauges as a fraction of precipitation (%) tended to decrease with increasing rainfall (Fig. 5.3d), suggesting less variability in throughfall and a reduced difference in spatial variability of throughfall measured by the two types of collectors for large events.

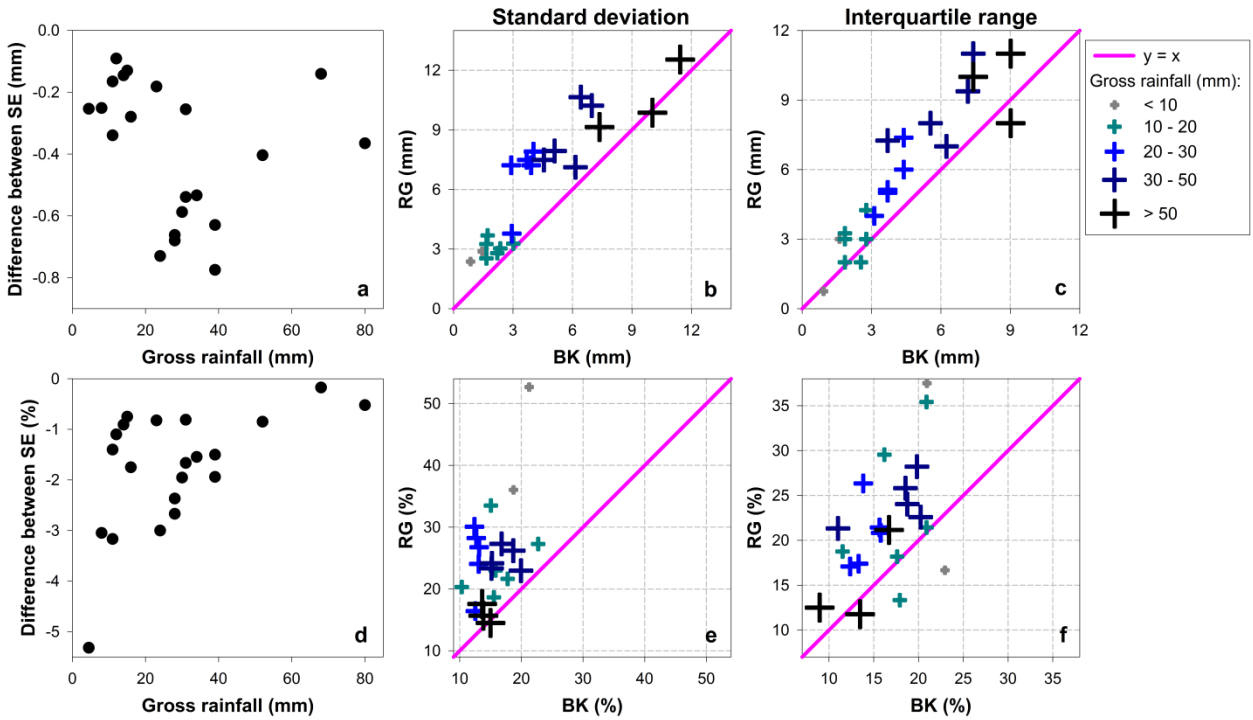

Fig. 5.3. The relation between gross rainfall and the difference between standard errors (SE) of throughfall measured by the buckets (BK) and rain gauges (RG) (*a* and *d*) and the relation between the standard deviation (*b* and *e*) and interquartile range (*c* and *f*) of throughfall measured by the buckets (BK) and the rain gauges (RG). The measured throughfall is expressed as amount (mm) (*a*-*c*) and as a fraction of precipitation (%) (*d*-*f*). A negative difference indicates larger standard errors for rain gauges than for buckets. Symbols represent different event size classes; the pink solid line represents the 1:1 line (*b*, *c*, *e* and *f*).

More significant local spatial clusters and outliers were identified in throughfall measured by the buckets than for rain gauges (Fig. 5.4a and b). The average number of measurements sites that were considered outliers was 2.3% (buckets) and 1.5% (rain gauges) for high throughfall sites surrounded by low throughfall (HL) and 1.4% (buckets) and 1.3% (rain gauges) for low throughfall sites surrounded by high throughfall (LH). The average number of high throughfall clusters (HH) was 2.1% (for buckets) and 0.7% (for rain gauges); the average number of low throughfall clusters (LL) was 0.7% (for buckets) and 0.6% (for rain gauges). We hypothesize that the difference in the number of significant local outliers and clusters was due to the spatial arrangement of buckets and rain gauges in the plot. However, further analyses are needed to assess if the sample size and spatial arrangement have an effect on the identification of significant locations of large or small throughfall amounts. Local outliers, and especially dripping points (HL), were more frequent than local clusters, suggesting the importance of dripping points in shaping the spatial variability of throughfall. The overall low number of

significant local clusters and outliers indicates the presence of a near random pattern in measured throughfall.

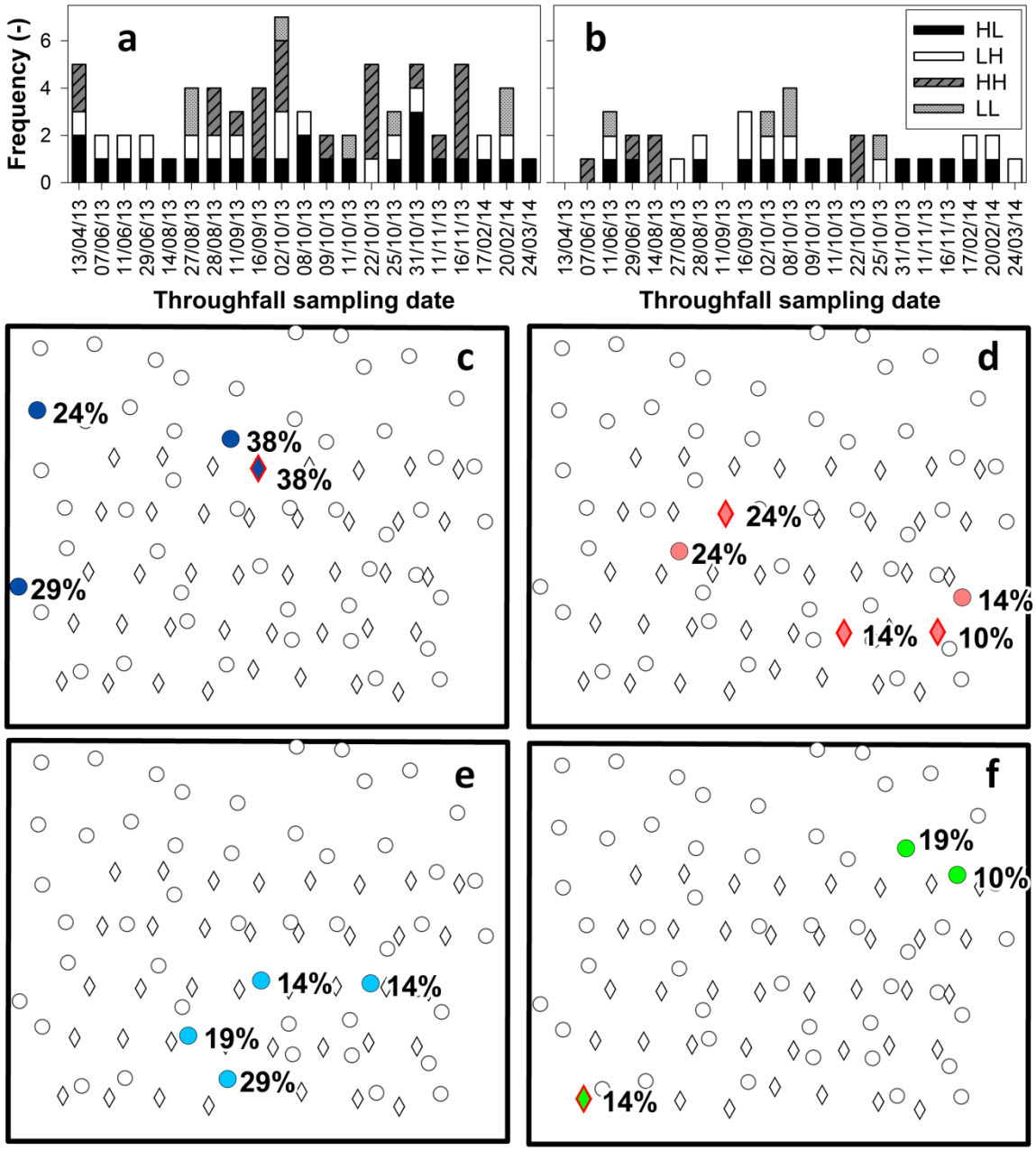

Fig. 5.4. Frequency of significant local outliers and clusters of throughfall for each sampling date in buckets (a) and rain gauges (b) and location of the gauges that were significant local outliers or clusters for more than 10% of the measurement dates: high throughfall surrounded by low throughfall (HL) (c); low throughfall surrounded by high throughfall (LH) (d); clusters of high throughfall (HH) (e); clusters of low throughfall (LL) (f). The locations of the buckets are shown with circles, the locations of the rain gauges with diamonds.

Dripping points (HL) displayed the highest persistence (i.e., temporal stability up to 38% of the sampling times for the highest-frequency locations) (Fig. 5.4c), confirming the important role of dripping points in the spatial distribution of throughfall. When comparing the spatial

distribution of the significant local spatial clusters and outliers, it appears that the clusters identified for bucket measurements were not far from the ones identified for the rain gauges when HL or LH were considered. However, locations where the canopy intercepted more rainfall (LL) were far from similar locations for the rain gauges. In addition, sites that were significant high clusters for more than 10% of the measurements for the buckets were not identified as high throughfall clusters by the rain gauge measurements. This suggests that the size of the collectors and the number of measurements influenced both the observed spatial variability and the spatial patterns of throughfall.

6. ANALYSIS AND MODELING OF TEMPORAL STABILITY OF THROUGHFALL AND SOIL MOISTURE

6.1. Relation between throughfall and rainfall characteristics

Based on the results obtained in Section 5, throughfall amounts measured by buckets were considered for the analysis of temporal persistence of throughfall patterns and their relation with near-surface soil moisture.

The mean throughfall of 24 measurements between April 2013 and March 2014 was 80.4% of the gross rainfall. The relation between rainfall characteristics and throughfall spatial mean suggests that throughfall amounts tend to increase with the increasing rainfall amount (gross rainfall; Fig. 6.1.1) and mean rainfall intensity (Fig. 6.1.2). Large throughfall amounts are likely due to the more uniform saturation of canopy during large events, which leads to increasing fraction of precipitation reaching the ground. Significant correlations were found between throughfall spatial mean and gross rainfall (ρ_s = 0.53, $p < 0.01$), mean rainfall intensity (ρ_s = 0.56, $p < 0.01$) and maximum rainfall intensity (ρ_s = 0.51, $p < 0.05$). Considering each sampling location separately it was found that only 42% of the 50 buckets were characterized by a significant correlation ($p < 0.05$) between throughfall and gross rainfall and throughfall and mean rainfall intensity. The significant correlations decreased to 28% when considering the relation between throughfall and maximum rainfall intensity.

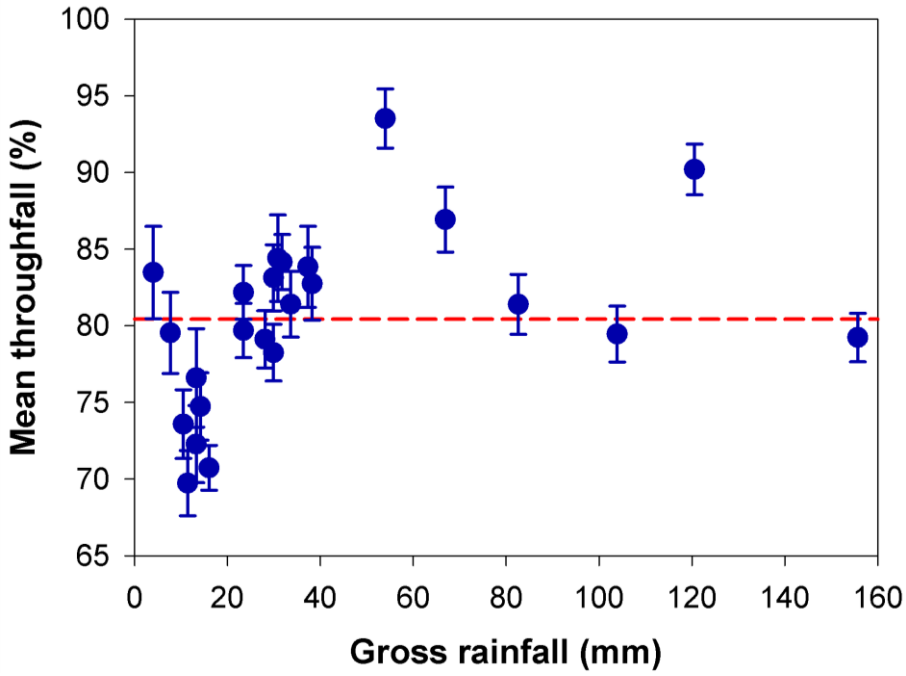

Fig. 6.1.1. Relation between gross rainfall and throughfall spatial mean. The red dashed line represents the mean throughfall computed for 24 measurements using the buckets, while the error bars are the standard errors.

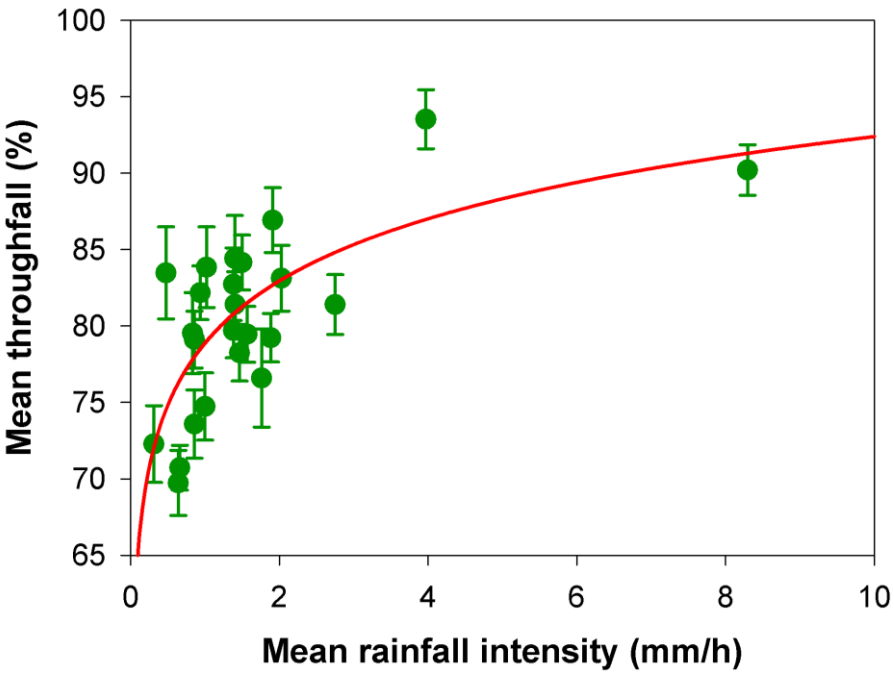

Fig. 6.1.2. Relation between mean rainfall intensity and throughfall spatial mean computed for 24 measurements using buckets. The error bars represent the standard errors.

As expected, the variability in throughfall spatial patterns decreased with the increasing gross rainfall (Staelens et al., 2006). Large coefficients of variation were found for small rainfall events (Fig. 6.1.3) likely due to a heterogeneous saturation of the tree canopies. Similarly to Staelens et al. (2006), the median spatial coefficient of variation of throughfall was larger during the growing/leafed season (April-October; 18 sampling times) than for the dormant season (November-March; six sampling times). The difference in the median spatial coefficient of variation was not significant (Mann-Whitney rank sum test, $p = 0.07$). However, the reduced sample size for the dormant season could have influenced the obtained result, which needs additional measurements to be confirmed.

The Shapiro-Wilk test was used to assess whether the throughfall samples followed a normal distribution. For 14 sampling dates throughfall data matched the normal distribution. The results of the tests were not explained by the analyzed rainfall characteristics. For instance, non normality of the samples was found both for small and large rainfall amounts and for low and high rainfall intensities.

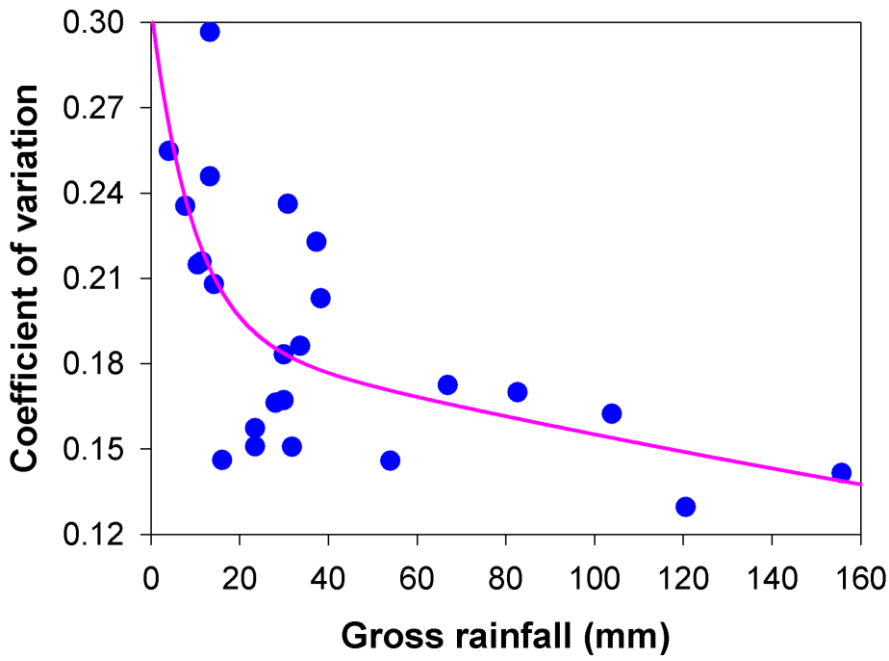

Fig. 6.1.3. Relation between gross rainfall and spatial coefficient of variation of throughfall.

For each sampling date, the number (and frequency) of buckets collecting throughfall amounts > 105% (these locations were considered as dripping points) and < 65% (these buckets were considered as affected by larger interception than the other locations) were computed. Figure 6.1.4 shows that the frequency of dripping points ranged between 0 and 18% and no significant correlation was found with gross rainfall and mean rainfall intensity. On the contrary, canopy interception strongly decreased with increasing gross rainfall and intensity. These results suggest that the frequency of dripping points is almost constant during both large and small events, while rainfall characteristics have a strong effect on the amount of throughfall reaching the ground.

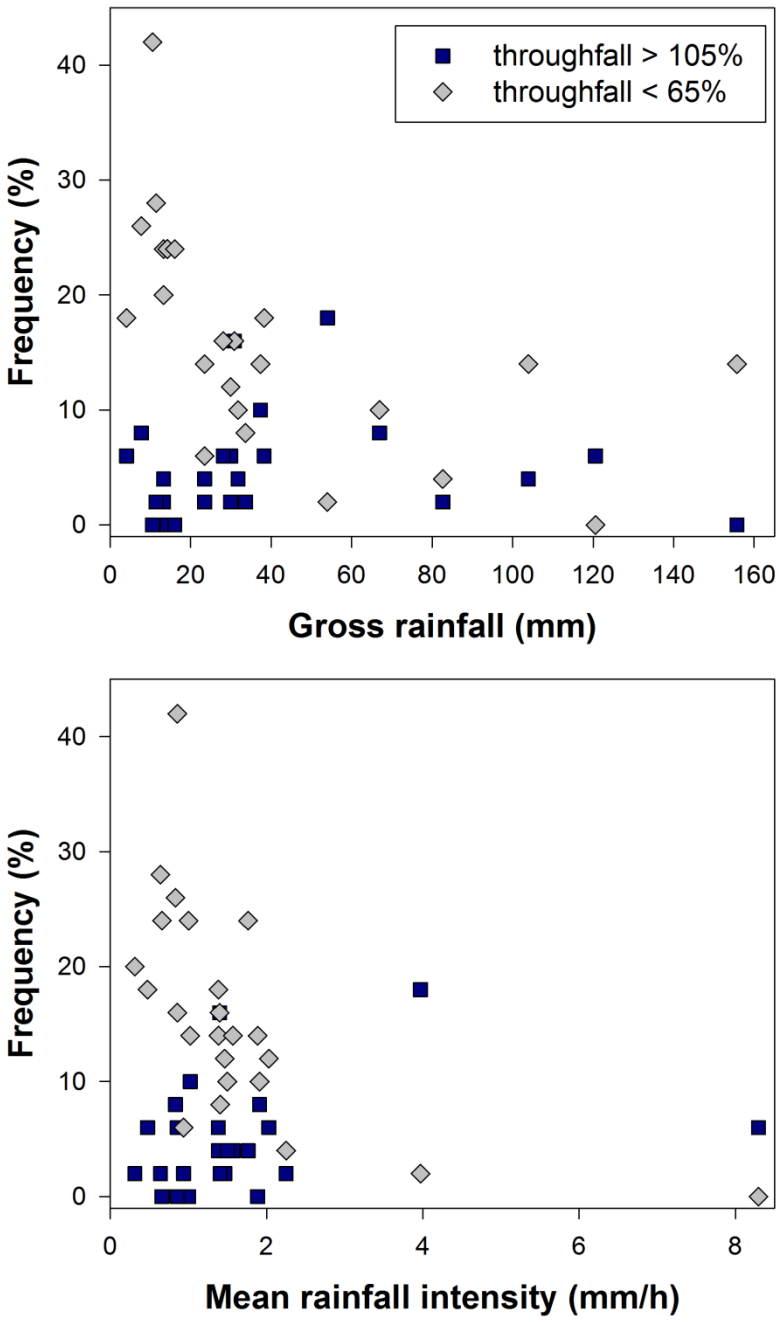

Fig. 6.1.4. Frequency of buckets with throughfall amount > 105% and < 65% for each sampling date, in relation to gross rainfall and mean rainfall intensity.

6.2. Temporal stability of throughfall and relation with vegetation characteristics

The analysis of the temporal stability of throughfall showed that positive and significant correlation coefficients ($p < 0.05$) were found between all the pairs of consecutive observation times (Fig. 6.2.1). The positive and significant correlation coefficients indicate that sampling sites tend to maintain proportionally larger or smaller throughfall amounts for the following rainfall event. Similarly, significant and positive correlations occurred for 95% of all the possible 253 event pairings. The correlation coefficients (ρ_s) were examined to determine if temporal lag between two consecutive samplings or the difference in rainfall characteristics (gross

rainfall, mean and maximum rainfall intensity and duration) could explain the correlation between the spatial patterns (Zimmermann et al., 2008; Carlyle-Moses and Lishman, 2015). In contrast to Zimmermann et al. (2008) and Carlyle-Moses and Lishman (2015), the temporal lag between pairs of consecutive sampling times was not a good predictor for ρ_s. The difference in rainfall characteristics and the seasonality could also not explain the variability in the correlation coefficients.

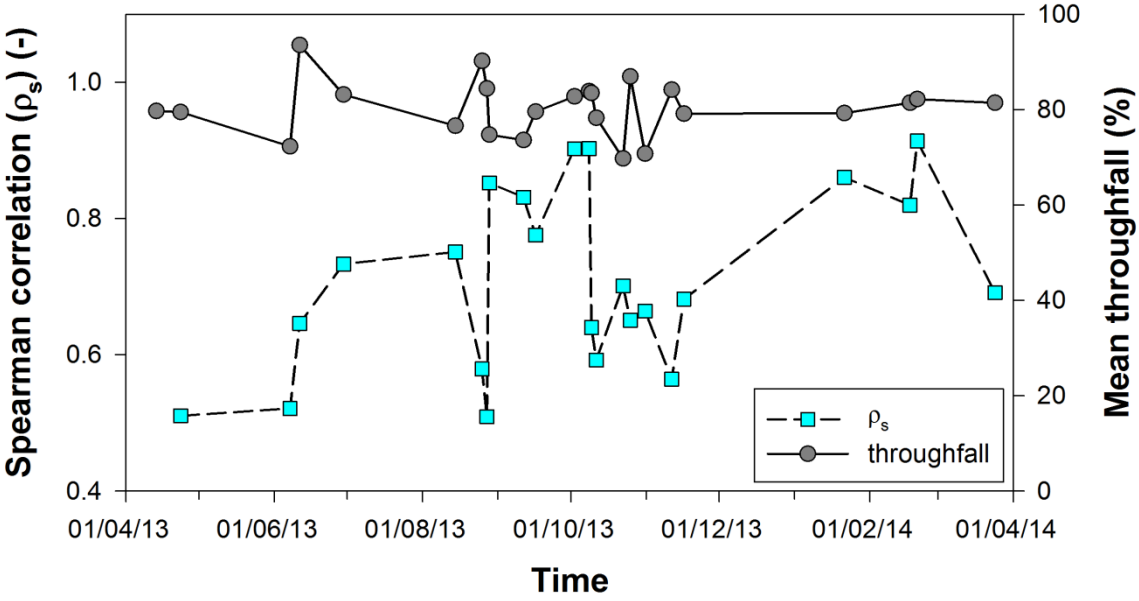

Fig. 6.2.1. Time series of throughfall spatial mean and correlation coefficients between pairs of throughfall sampling times.

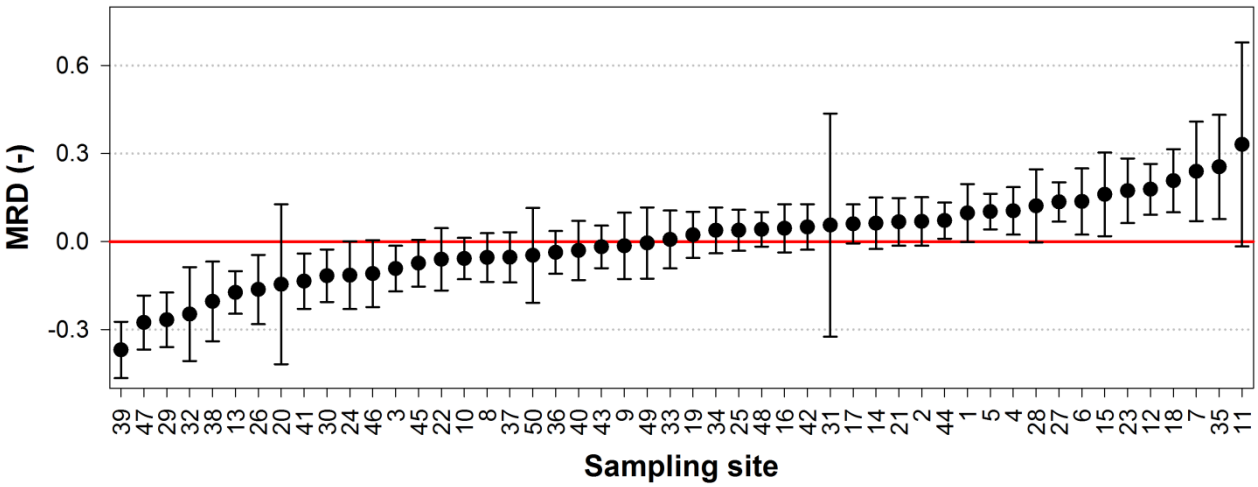

Fig. 6.2.2. Ranked MRD of throughfall measured by buckets (all 24 sampling times were considered). Error bars are SDRD computed for each sampling site, the red solid line represents MRD = 0.

Ranked MRD of throughfall ranged between -0.37 (for BK 39) and 0.33 (for BK 11). BK 49 was the location most representative of the throughfall spatial mean (it had the MRD value closest to zero) (Fig. 6.2.2). SDRD values were not correlated to MRD values and they ranged between

0.06 and 0.38, with an average of 0.11. BK 20, BK 31 and BK 11 were characterized by very large SDRD: these locations had amounts of throughfall both larger and smaller than the spatial mean. Indeed, these locations had throughfall both > 105% and < 65%; this likely suggests that very small-scale characteristics of the vegetation (e.g., the inclination of a branch) could affect the throughfall amount.

Correlation coefficients computed between MRD and SDRD of throughfall and characteristics of the vegetation (distance from the nearest tree, canopy openness, LAI and weighted basal area (WBA); Table 6.2.1) were very small. MRD was negatively correlated with WBA and γ values were small (0.5 and 1.0). This indicates that large basal areas corresponded to small MRD (i.e., there is more interception). However, the small ρ_s imply that WBA or the other vegetation characteristics cannot be used as good predictors of the temporal stability of throughfall.

ρ_s	MRD	SDRD
Distance from the nearest tree	0.06	-0.08
Canopy openness (84° lens)	-0.12	0.43 (**)
Canopy openness (fisheye lens)	0.02	-0.03
LAI	-0.01	0.00
WBA (γ = 0.5)	-0.38 (**)	0.15
WBA (γ = 1.0)	-0.32 (*)	0.24
WBA (γ = 2.0)	-0.26	0.32 (*)
WBA (γ = 4.0)	-0.14	0.15

Significance codes: * = 0.05; ** = 0.01; *** = 0.001.

Table 6.2.1. Spearman correlation coefficients computed for the relation between MRD and SDRD and vegetation characteristics (Section 3.2.5).

6.3. Variability of near-surface soil moisture data

As expected, soil moisture increased after a rainfall pulse especially at the shallow layer (Fig. 6.3.1). Inspection of the data shows that mean soil moisture was larger for 0-7 cm depth than for the 0-12 cm.

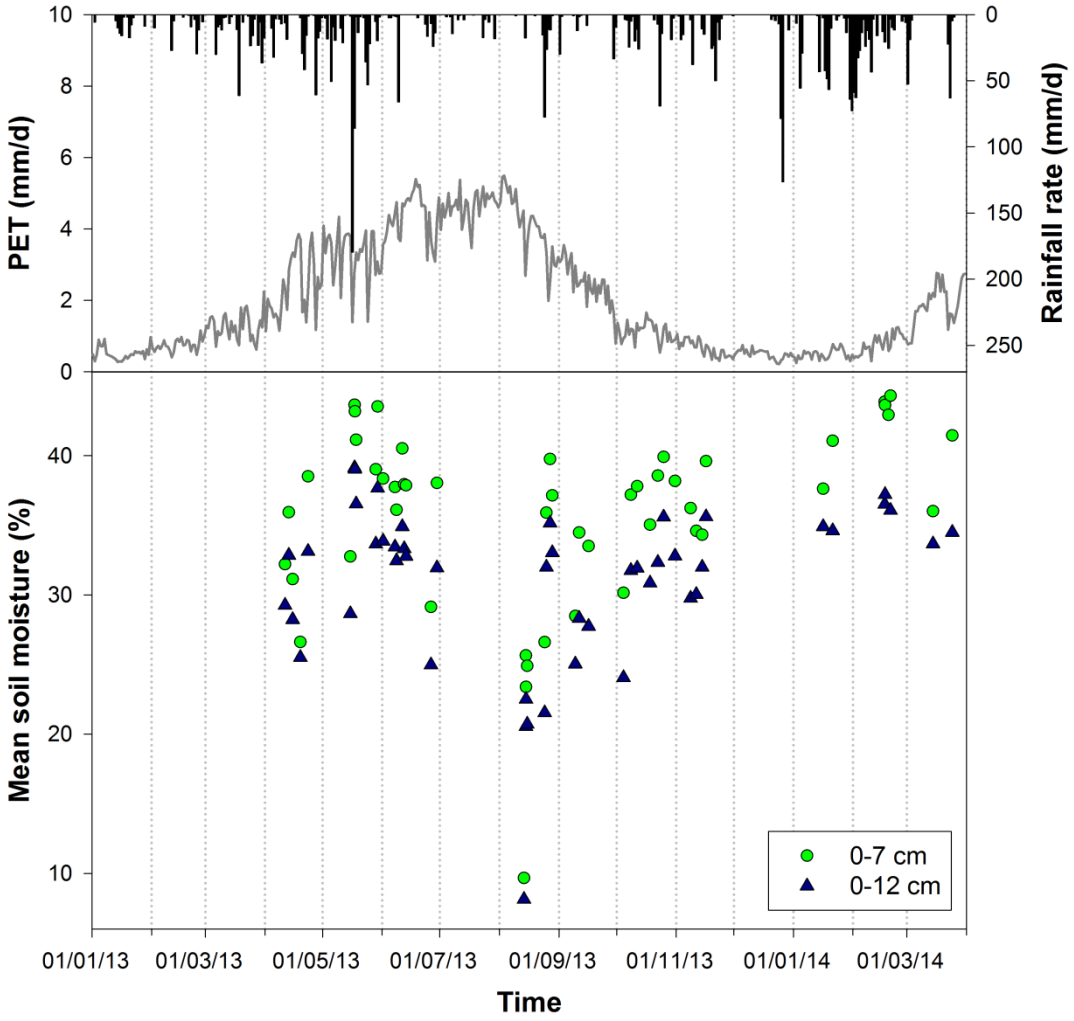

Fig. 6.3.1. Time series of spatial mean soil moisture at 0-7 and 0-12 cm depth, rainfall and potential evapotranspiration (PET).

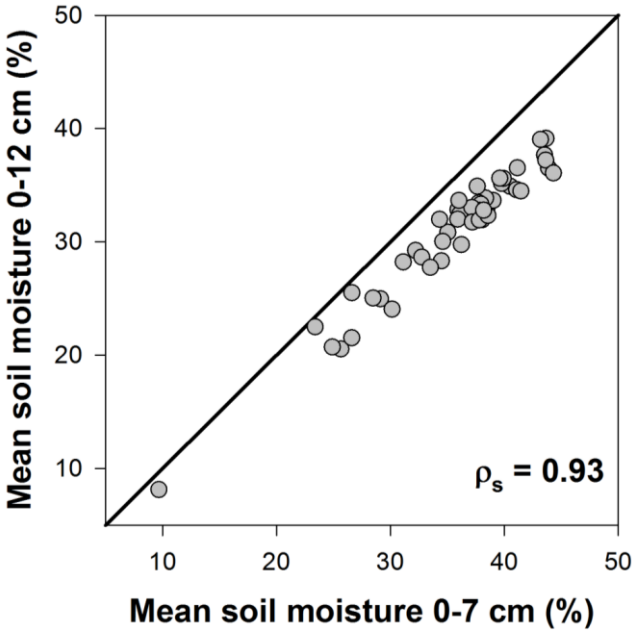

Fig. 6.3.2. Relation between the spatial mean soil moisture at 0-7 cm and at 0-12 cm depth.

The spatial mean soil moisture was significantly correlated between the two depths (0-7 and 0-12 cm depth) and mean soil moisture was always larger at the shallow layer (Fig. 6.3.2).

Figure 6.3.3 shows that the coefficient of variation at the two depths decreased when the mean soil moisture value increased (Penna et al., 2009, 2013). The largest coefficient of variation was found on 13th August 2013 during a dry period.

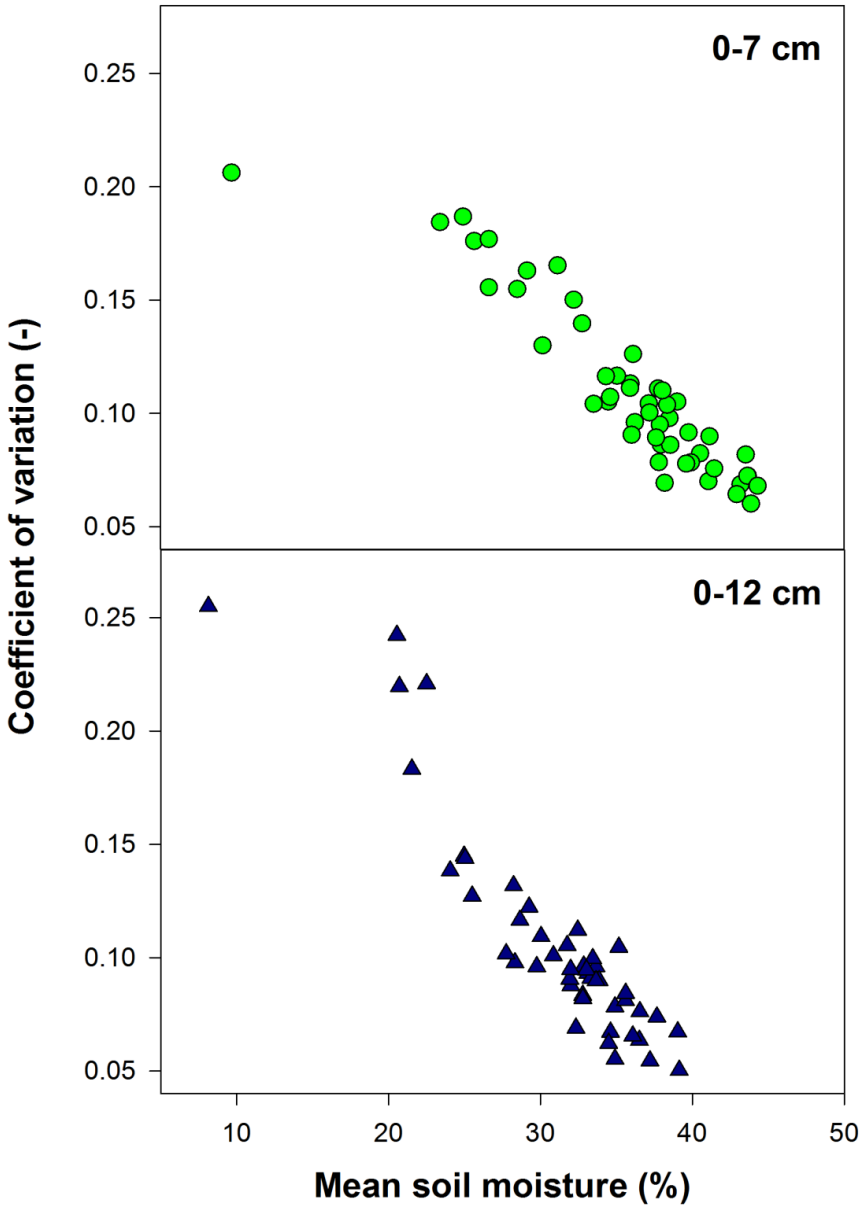

Fig. 6.3.3. Relation between the spatial mean soil moisture and the coefficient of variation. at 0-7 cm and at 0-12 cm depth.

6.4. Temporal stability of near-surface soil moisture

The analysis of the temporal stability of throughfall showed that positive and significant correlation coefficients ($p < 0.05$) were found between all the pairs of consecutive observation times (Fig. 6.4.1). The correlation coefficients (ρ_s) were examined to determine if temporal lag between two consecutive samplings could explain the correlation between the spatial patterns. In contrast to the results for throughfall (Section 6.2), the temporal lag between pairs of consecutive sampling times of soil moisture was negatively correlated with ρ_s. This indicates that for both depths soil moisture tends to have a larger stability when the temporal lag between measurements is small.

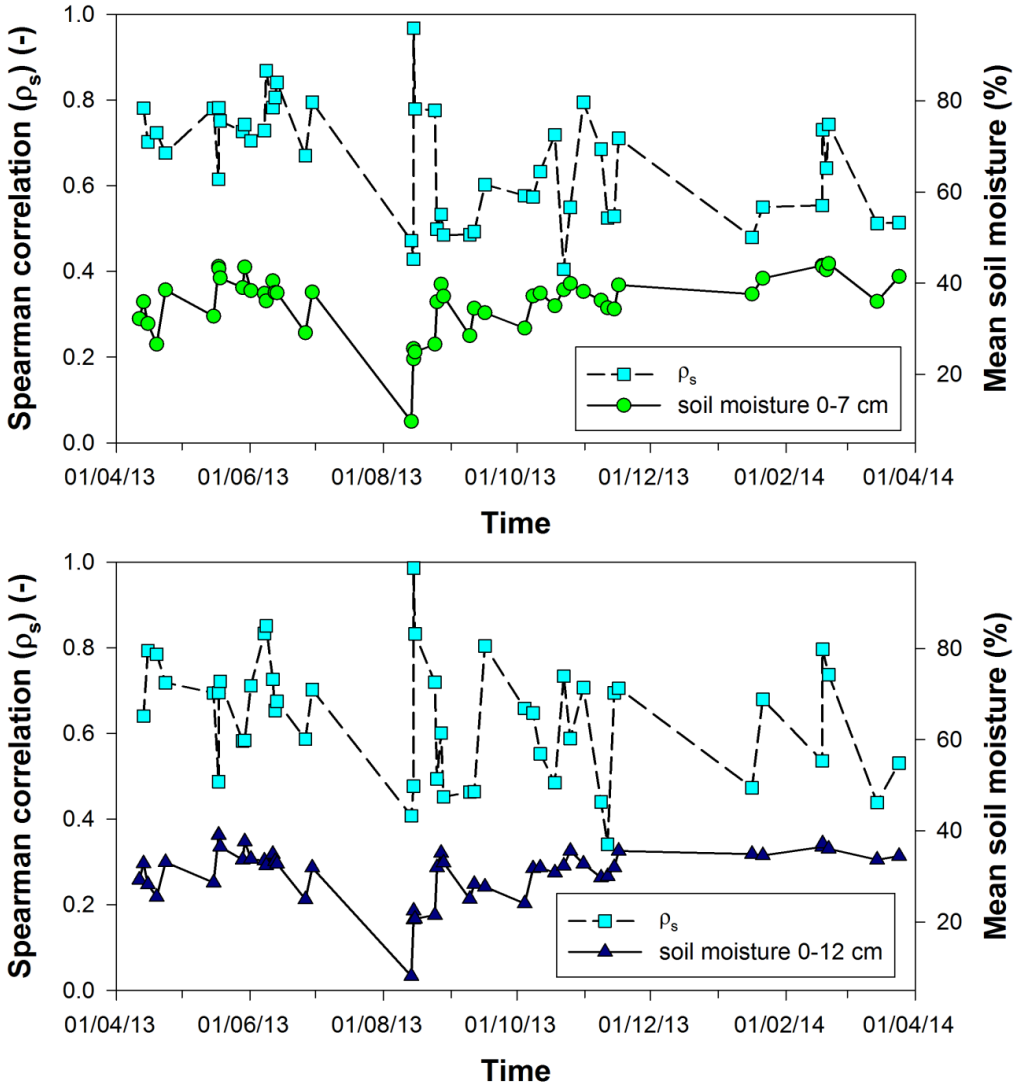

Fig. 6.4.1. Time series of soil moisture spatial mean at 0-7 and 0-12 cm depth and correlation coefficients between pairs of soil moisture sampling times.

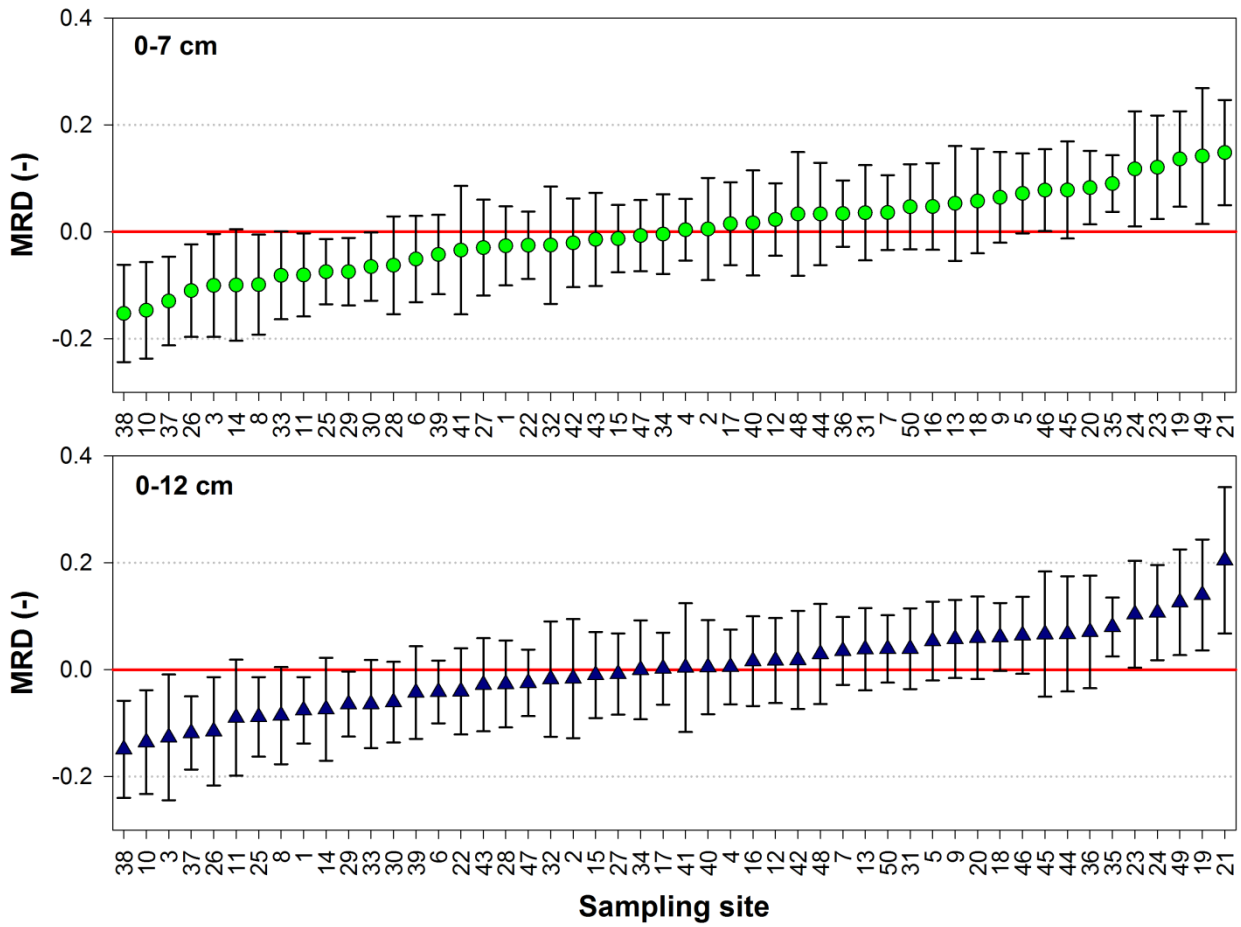

Fig. 6.4.2. Ranked MRD of soil moisture measured at 0-7 and 0-12 cm depth. Error bars are SDRD computed for each sampling site, the red solid line represents MRD = 0.

Ranked MRD of soil moisture at 0-7 cm depth ranged between -0.15 (for the site upslope BK 38) and 0.15 (for the site upslope BK 21). The location upslope BK 17 was the most representative of the soil moisture spatial mean at 0-7 cm depth (Fig. 6.4.2). Ranked MRD of soil moisture at 0-12 cm depth ranged between -0.15 (for the site upslope BK 38) and 0.20 (for the site upslope BK 21). The location upslope BK 17 was the most representative of the soil moisture spatial mean at 0-12 cm depth (Fig. 6.4.2). The ranked MRD for the two soil moisture depths were quite similar, but they were quite different compared to the ranked MRD of throughfall (Fig. 6.2.2). The range of MRD was also larger for throughfall than for MRD of soil moisture.

SDRD values of soil moisture at 0-7 cm depth ranged between 0.05 and 0.13, with an average of 0.09. SDRD values of soil moisture at 0-12 cm depth ranged between 0.06 and 0.14, with an average of 0.09. Compared to the SDRD range for throughfall, soil moisture had smaller range and most importantly SDRD of the different sampling sites were similar.

The large range for MRD and SDRD of throughfall suggest that throughfall is characterized by smaller temporal stability compared to soil moisture.

Correlation coefficients computed between MRD and SDRD of soil moisture and characteristics of the vegetation (distance from the nearest tree, canopy openness, LAI and weighted basal area (WBA)) were not significant ($p > 0.05$). This probably means that soil moisture temporal stability is not related to surface vegetation characteristics and the results of this correlation analysis cannot be used to infer the influence of root fraction on near-surface soil moisture.

The correlations computed between MRD of throughfall and soil moisture were not significant. This implies that soil properties and/or vegetation characteristics could weaken the effect of throughfall spatial patterns on soil moisture. No significant correlations were also found between throughfall and differences between soil moisture measured, at 0-7 cm and 0-12 cm depth, before and after the throughfall sampling. Similarly, no significant or weak correlations were found between throughfall and post rainfall event soil moisture (Fig. 6.5.1). Shachnovich et al. (2008) found similar results and related the absence of correlation between the spatial patterns to a horizontal movement of water on the soil surface or within the soil matrix.

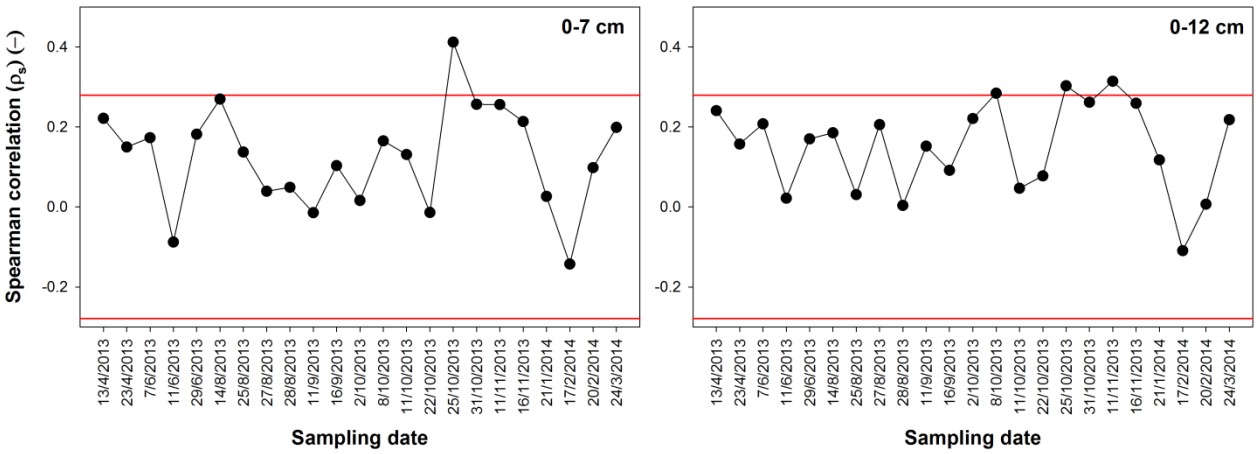

Fig. 6.4.3. Spearman rank correlation coefficients computed between throughfall measured by buckets and post-event soil moisture at the two soil depths, 0-7 cm (left panel) and 0-12 cm (right panel). Red lines indicate significance level with α = 0.05.

6.5. Factors controlling the temporal stability of near-surface soil moisture patterns

This Section of the thesis focuses on the simulation of the temporal stability of soil moisture at the two depths by using the model described in Section 3.1.2 with the sets of parameters reported in Section 3.2.6.

Homogeneous vegetation sets of parameters and relatively small spatial variability in the saturated hydraulic conductivity yielded a small range in the simulated MRD values of soil moisture compared to the observed range of MRD (Fig. 6.5.1). Similarly, simulated SDRD of soil

moisture had smaller values compared to the observed SDRD (Fig. 6.5.2). The analysis of the correlation between the simulated MRD distributions of throughfall and soil moisture highlighted that the two patterns were highly correlated (Fig. 6.5.3). Large correlation coefficients between MRD distributions of throughfall and soil moisture were obtained when the spatial variability of the saturated hydraulic conductivity was rather small.

On the other hand, the simulated SDRD distributions of throughfall and soil moisture were not significantly correlated (Fig. 6.5.4) for all the sets of parameters (this is likely due to the measurement error used in the simulations; Table 3.2.3).

The spatial variability in k_s had an important effect on the temporal stability of soil moisture: a larger variability was responsible for a larger range for MRD (Martinez et al., 2013)

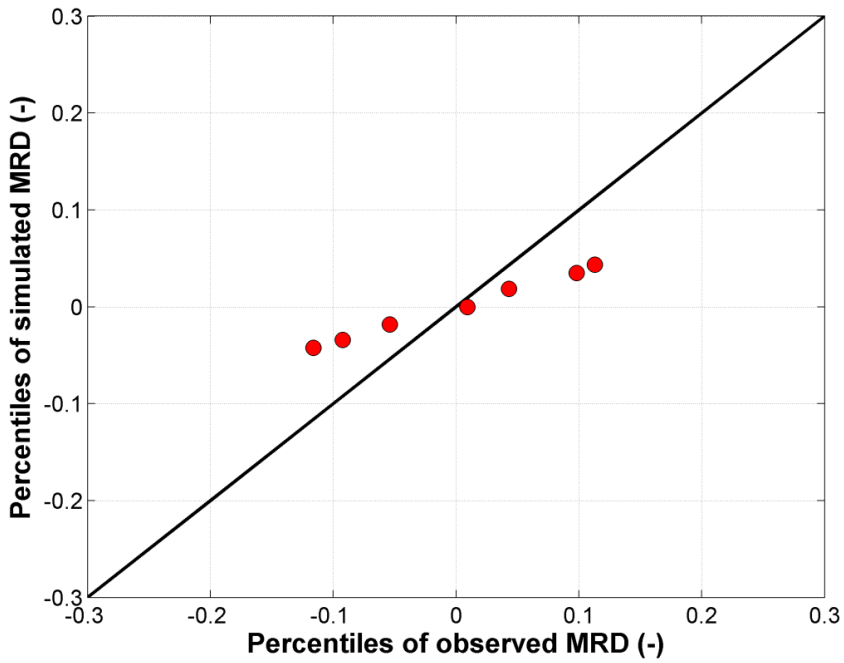

Fig. 6.5.1. Relation between percentiles (i.e., 5th, 10th, 25th, 50th, 75th, 90th and 95th) of the observed and the simulated MRD distributions of post rainfall event soil moisture at 0-7 cm. The simulated values shown in the plot are the averages obtained from 200 simulations, while the error bars represent the standard deviations. The black solid line represents the 1:1 line. The vegetation was simulated as spatially homogeneous, while the mean k_s was 200 mm/d and σ_{k_s} was 0.2.

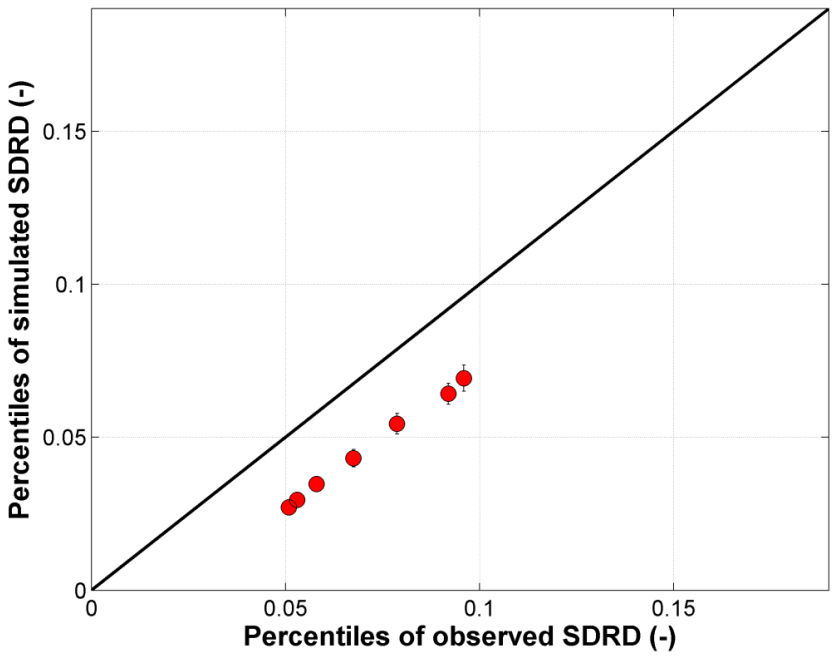

Fig. 6.5.2. Relation between percentiles (i.e., 5th, 10th, 25th, 50th, 75th, 90th and 95th) of the observed and the simulated SDRD distributions of post rainfall event soil moisture at 0-7 cm. The simulated values shown in the plot are the averages obtained from 200 simulations, while the error bars represent the standard deviations. The black solid line represents the 1:1 line. The vegetation was simulated as spatially homogeneous, while the mean k_s was 200 mm/d and σ_{k_s} was 0.2.

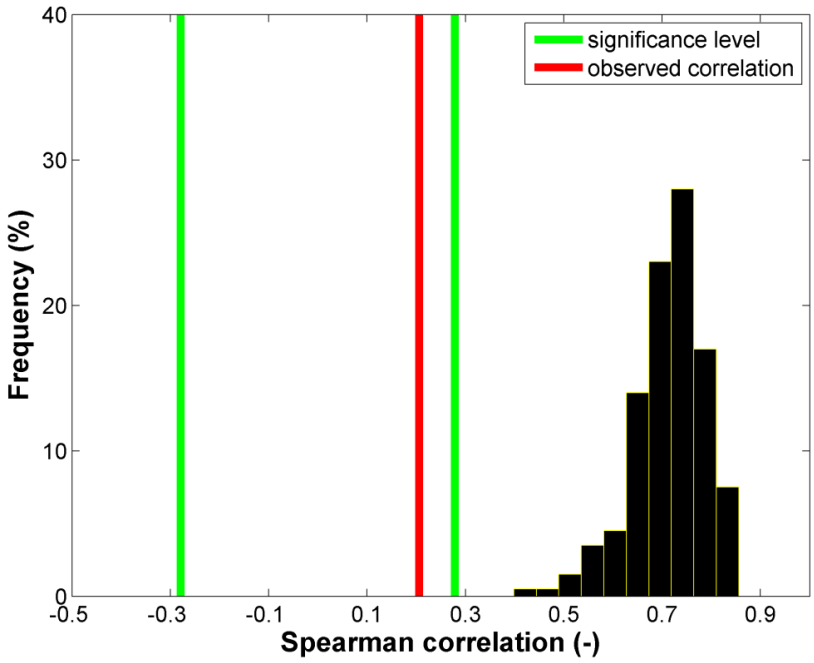

Fig. 6.5.3. Frequency of the Spearman correlation coefficients computed between the simulated MRD distributions of throughfall and post rainfall event soil moisture measured at 0-7 cm depth. The red vertical line represents the observed correlation. The vegetation was simulated as spatially homogeneous, while the mean k_s was 200 mm/d and σ_{k_s} was 0.2.

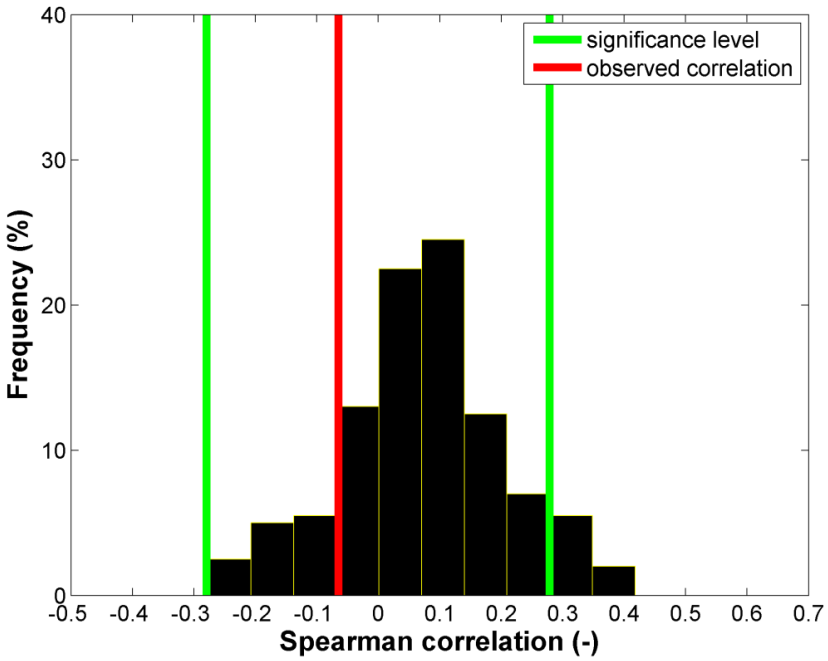

Fig. 6.5.4. Frequency of the Spearman correlation coefficients computed between the simulated SDRD distributions of throughfall and post rainfall event soil moisture measured at 0-7 cm depth. The red vertical line represents the observed correlation. The vegetation was simulated as spatially homogeneous, while the mean k_s was 200 mm/d and σ_{k_s} was 0.2.

Heterogeneous vegetation sets of parameters, correlated with k_s, and relatively large spatial variability in k_s yielded a range in the simulated MRD values of soil moisture similar to the observed range of MRD (Fig. 6.5.5). Similarly, the simulated SDRD values of soil moisture were similar to the observed range of SDRD (Fig. 6.5.6). The analysis of the correlation between the simulated MRD distributions of throughfall and soil moisture highlighted that the two patterns were less significantly correlated (Fig. 6.5.7) compared to sets of parameters simulating a homogeneous vegetation.

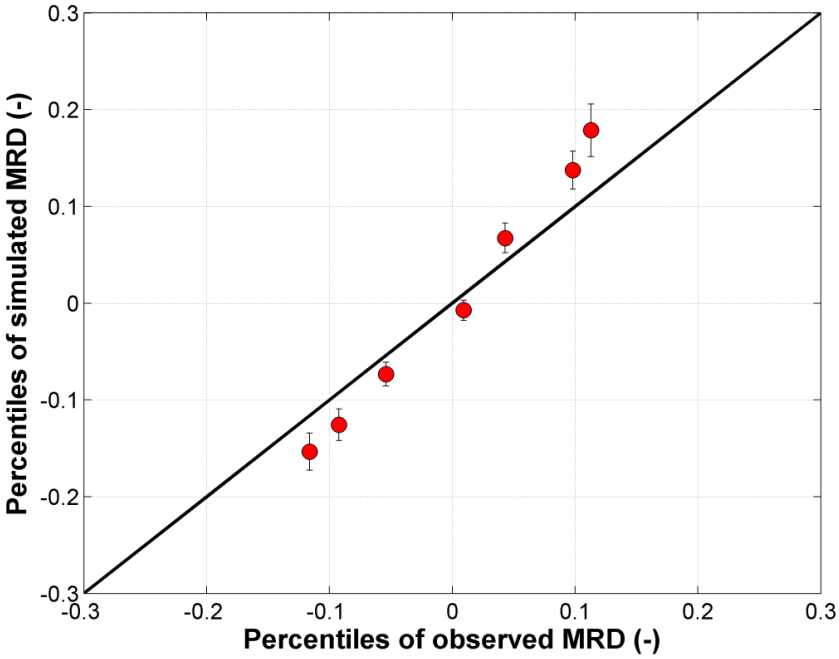

Fig. 6.5.5. Relation between percentiles (i.e., 5th, 10th, 25th, 50th, 75th, 90th and 95th) of the observed and the simulated MRD distributions of post rainfall event soil moisture at 0-7 cm. The simulated values shown in the plot are the averages obtained from 200 simulations, while the error bars represent the standard deviations. The black solid line represents the 1:1 line. The vegetation was simulated as spatially heterogeneous and correlated with k_s, the mean k_s was 400 mm/d and σ_{k_s} was 0.8.

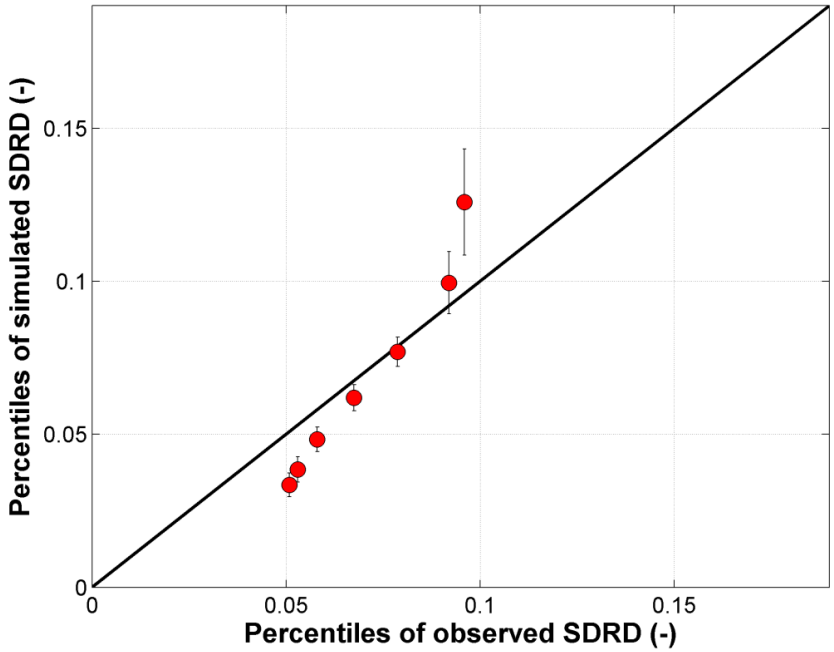

Fig. 6.5.6. Relation between percentiles (i.e., 5th, 10th, 25th, 50th, 75th, 90th and 95th) of the observed and the simulated SDRD distributions of post rainfall event soil moisture at 0-7 cm. The simulated values shown in the plot are the averages obtained from 200 simulations, while the error bars represent the standard deviations. The black solid line represents the 1:1 line. The vegetation was simulated as spatially heterogeneous and correlated with k_s, the mean k_s was 400 mm/d and σ_{k_s} was 0.8.

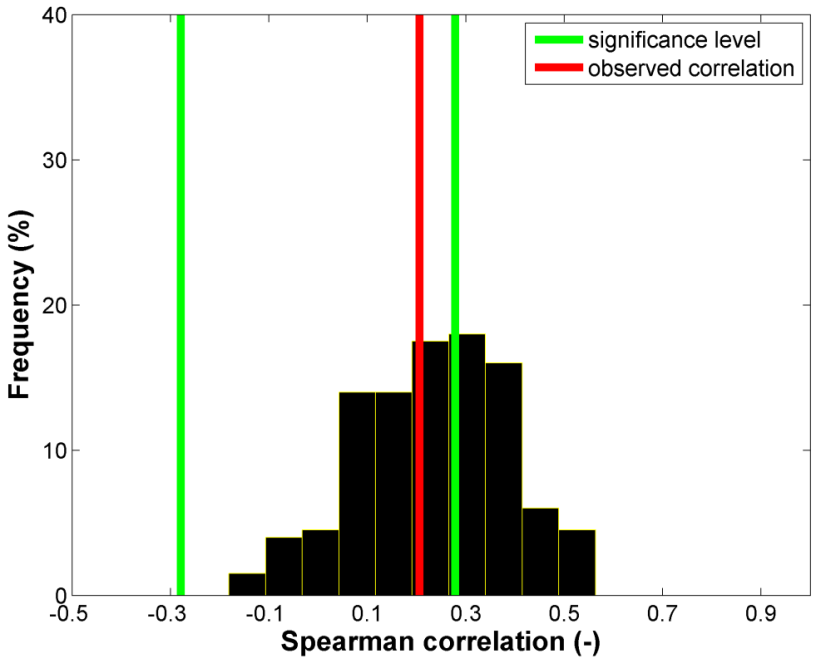

Fig. 6.5.7. Frequency of the Spearman correlation coefficients computed between the simulated MRD distributions of throughfall and post rainfall event soil moisture measured at 0-7 cm depth. The red vertical line represents the observed correlation. The vegetation was simulated as spatially heterogeneous and correlated with k_s, the mean k_s was 400 mm/d and σ_{k_s} was 0.8.

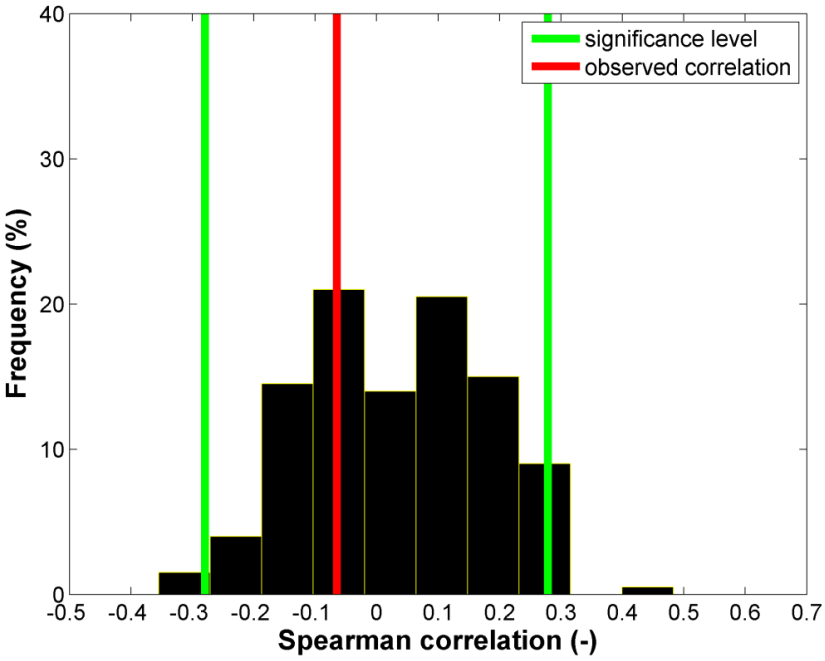

Fig. 6.5.8. Frequency of the Spearman correlation coefficients computed between the simulated MRD distributions of throughfall and post rainfall event soil moisture measured at 0-7 cm depth. The red vertical line represents the observed correlation. The vegetation was simulated as spatially heterogeneous and correlated with k_s, the mean k_s was 400 mm/d and σ_{k_s} was 0.8.

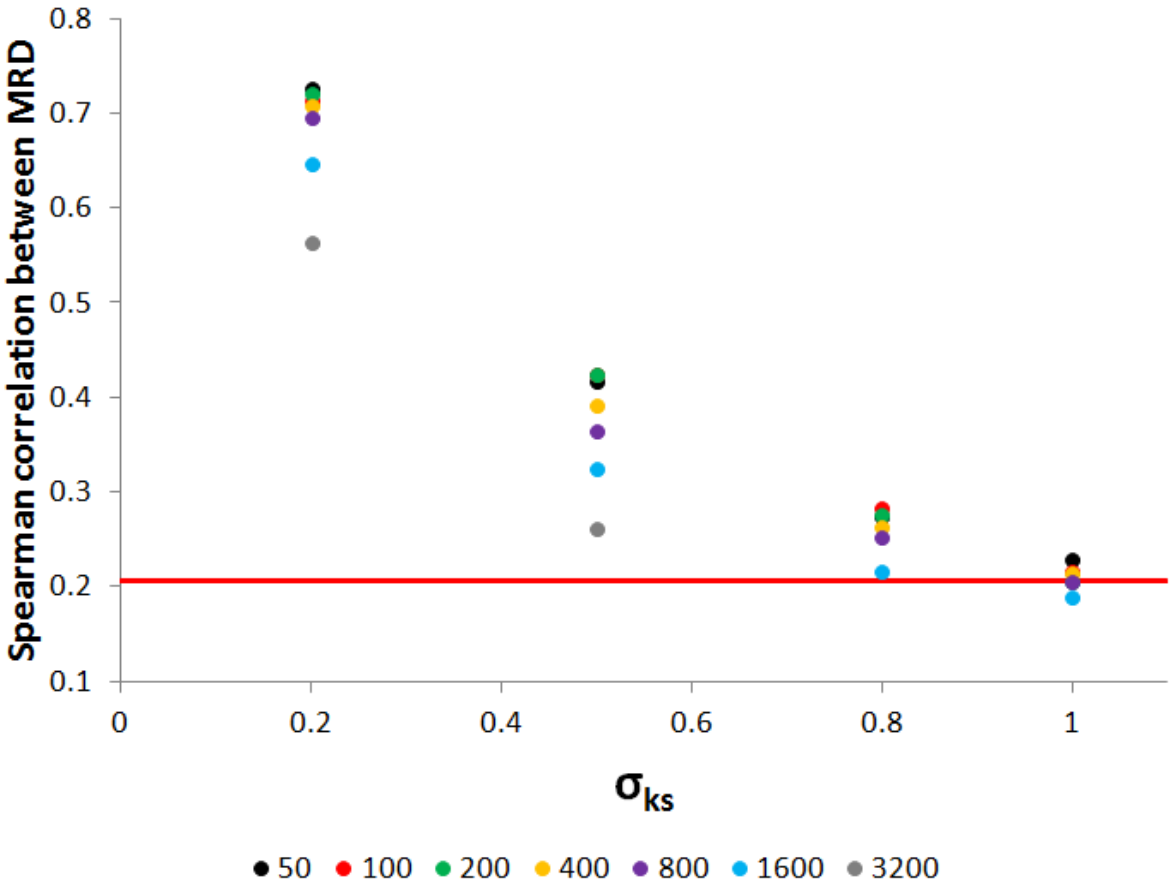

Fig. 6.5.9. Relation between the median of 200 Spearman correlation coefficients, computed between the simulated MRD of throughfall and soil moisture at 0-7 cm depth, and the standard deviation of k_s (σ_{k_s}). Colors of the dots were grouped by the mean k_s. The red solid line represents the value of the observed Spearman correlation coefficient computed between the MRD of throughfall and soil moisture at 0-7 cm depth. The vegetation was simulated as spatially homogeneous.

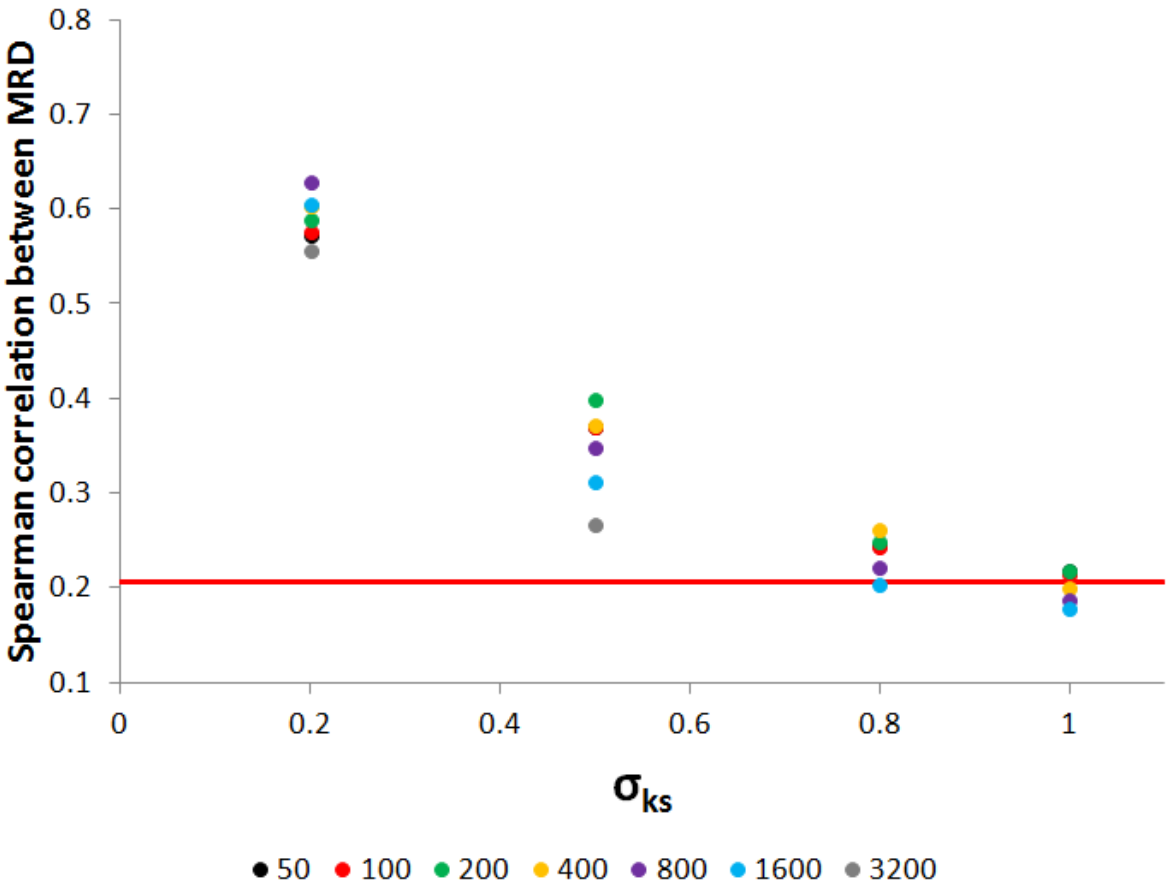

Fig. 6.5.10. Relation between the median of 200 Spearman correlation coefficients, computed between the simulated MRD of throughfall and soil moisture at 0-7 cm depth, and the standard deviation of k_s (σ_{k_s}). Colors of the dots were grouped by the mean k_s. The red solid line represents the value of the observed Spearman correlation coefficient computed between the MRD of throughfall and soil moisture at 0-7 cm depth. The vegetation was simulated as spatially heterogeneous.

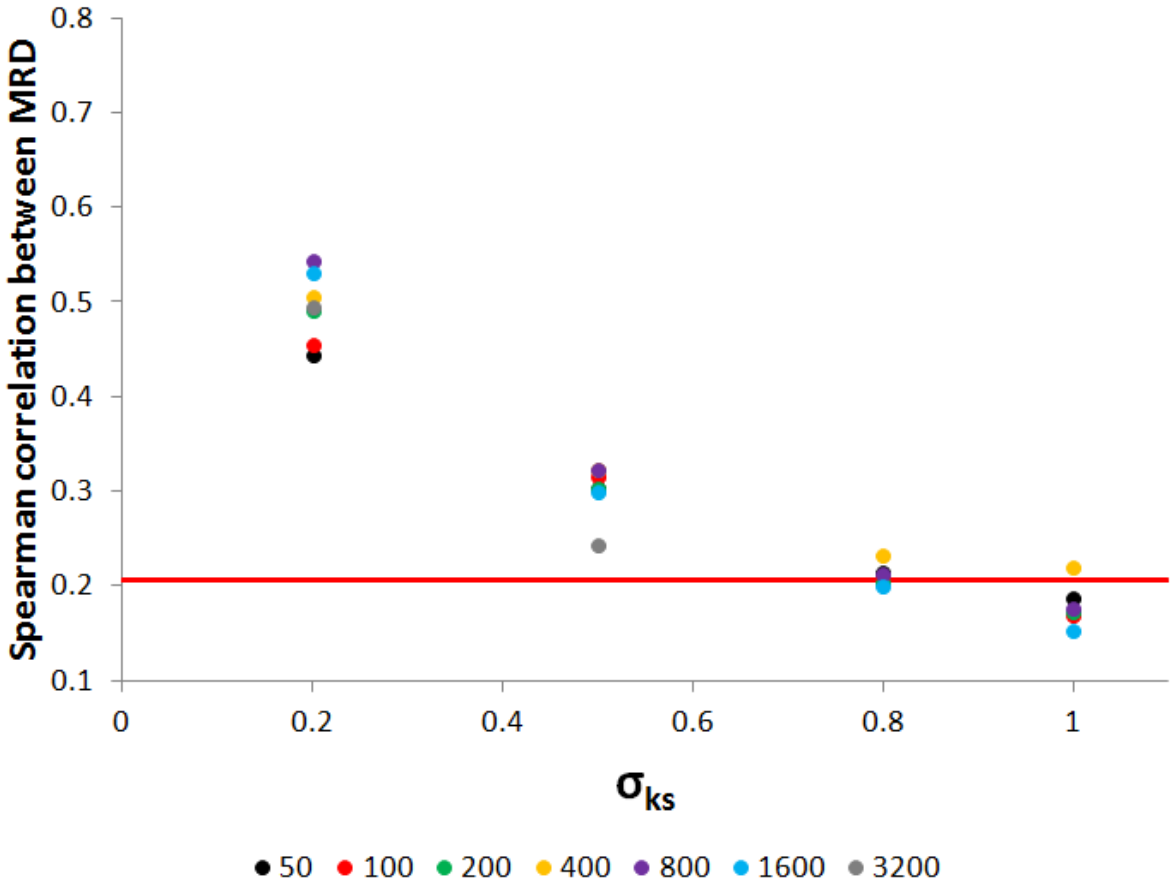

Fig. 6.5.11. Relation between the median of 200 Spearman correlation coefficients, computed between the simulated MRD of throughfall and soil moisture at 0-7 cm depth, and the standard deviation of k_s (σ_{k_s}). Colors of the dots were grouped by the mean k_s. The red solid line represents the value of the observed Spearman correlation coefficient computed between the MRD of throughfall and soil moisture at 0-7 cm depth. The vegetation was simulated as spatially heterogeneous and correlated with k_s.

Figures 6.5.9, 6.5.10 and 6.5.11 show the median value of the 200 Spearman correlation coefficients computed between the simulated MRD of throughfall and soil moisture at 0-7 cm depth. The simulated correlation coefficients were more similar to the observed when the spatial variability of the saturated hydraulic conductivity (σ_{k_s}) was very large. This was found for all the three combinations of parameter values used for the vegetation. Simulations of a spatially heterogeneous vegetation (Fig. 6.5.10) yielded better results compared to the homogeneous vegetation, especially when the spatial variability of k_s was small (σ_{k_s}= 0.2). However, the combination of a large spatial variability of k_s with a spatially heterogeneous vegetation had the stronger effect in weakening the correlation between the MRD of throughfall and soil moisture. Positively correlated spatial patterns of saturated hydraulic conductivity and LAI and root fraction in the soil layer imply a larger presence of more permeable soil layers and/or macropores close to the roots.

7. COMPARING SUBSURFACE CONNECTIVITY IN FIVE HEADWATER CATCHMENTS

Subsurface connectivity increased and decreased reflecting the dynamics of streamflow (Fig. 7.1). For all the five headwater catchments, subsurface connectivity increased rapidly during the rising limb of the hydrographs, reached a maximum and then declined slowly during the falling limb of the hydrographs. However, connectivity was characterized by a lower variability compared to the streamflow, especially during low flow conditions and small rainfall events. This implies differences in the synchronicity between runoff and subsurface connectivity and consequently in the areas getting connected to the stream network.

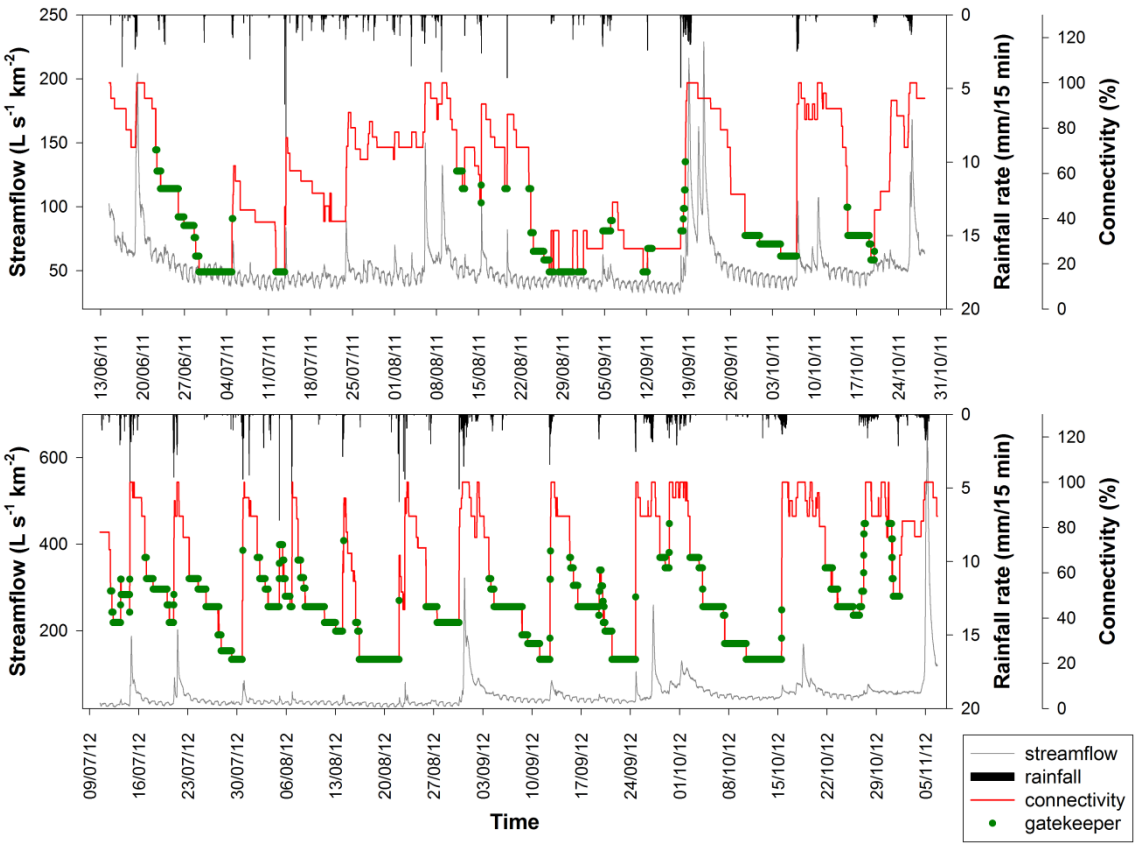

Fig. 7.1. Time series of rainfall, streamflow and subsurface connectivity (area-weighted) for BCC. Green dots represent time steps during which gatekeepers control connectivity.

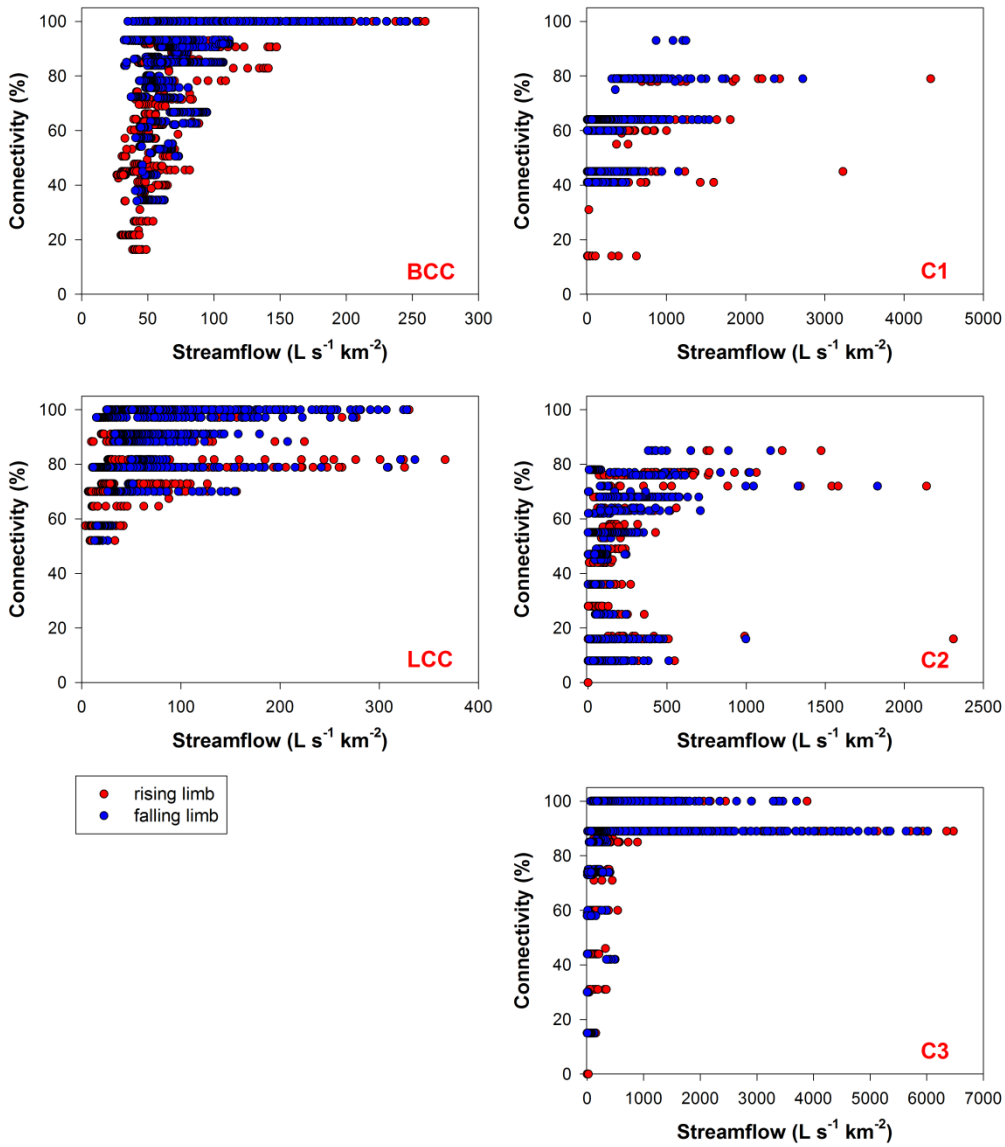

Fig. 7.2. Relation between connectivity (area-weighted) and streamflow during rainfall-runoff events (red dots: rising limb of the hydrograph; blue dots: falling limb of the hydrograph).

The analysis of rainfall-runoff events highlighted the different synchronicity in the peaks of streamflow and maximum connectivity. Hysteretic relations between streamflow and subsurface connectivity were found for all the five catchments. The hysteresis index (Section 3.4; Zuecco et al., 2015) was used to quantify and classify the loops (Fig. 7.3). Eight-shaped hysteresis with a main anti-clockwise loop (class III) and anti-clockwise hysteresis (class IV) were the most common. Class III had the largest frequency in BCC, C1 and C3, while linear relations and class II (eight-shaped hysteresis with a main clockwise loop) were the most common in LCC and C2, respectively. The dominating anti-clockwise loops suggest a delayed response of connectivity compared to the streamflow.

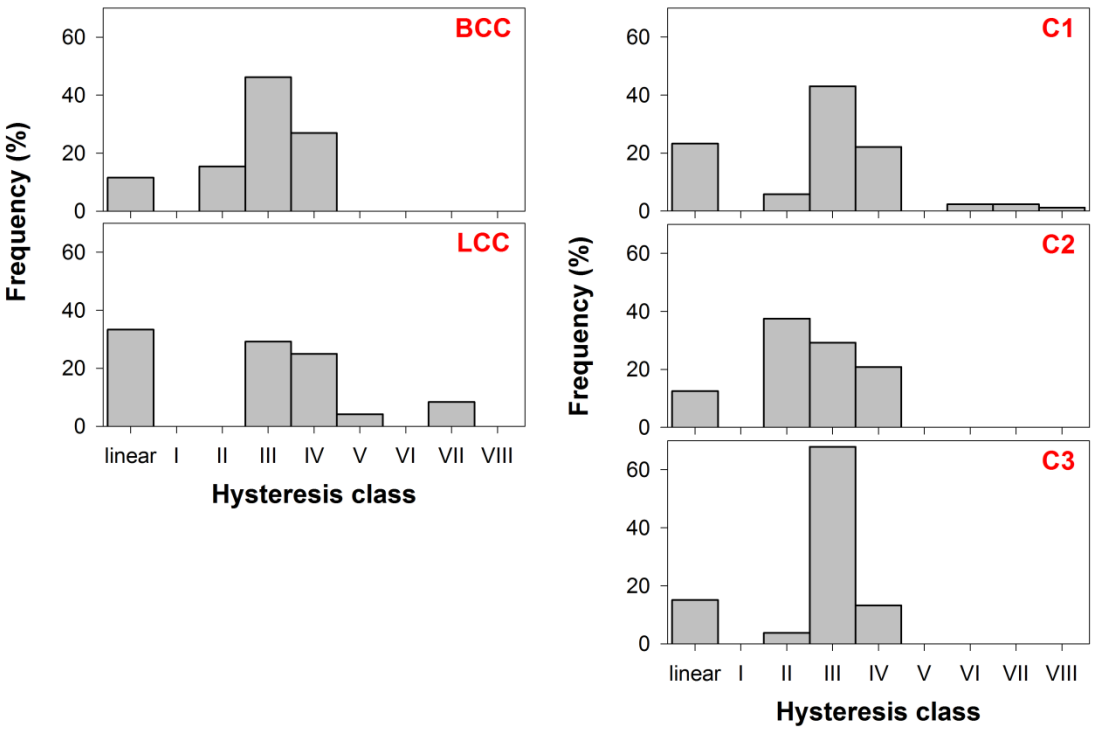

Fig. 7.3. Frequency distribution of the hysteresis classes for the five catchments.

The five headwater catchments had different hydrological responses to rainfall-runoff events. While BCC and LCC were characterized by a constant baseflow and small stormflow amounts, C1, C2 and C3 displayed quick responses to rainfall events and large stormflow amounts (Fig. 7.4). Total rainfall amounts (P) combined to antecedent precipitation in the two days prior to the event (AP2) explained most of the variation in the maximum connectivity in BCC and LCC (Table 7.1. and Fig. 7.4). In particular, thresholds could be identified in the relation between maximum connectivity and P+AP2 and between maximum connectivity and stormflow in BCC and LCC catchments (Fig. 7.5). On the contrary, maximum connectivity increased more linearly with increasing P+AP2 in C1 and C2. This is likely due to a more variable activation of the piezometers during a rainfall-runoff event in C1 and C2 and to specific areas of the catchments which became connected only during very wet conditions.

	Stormflow					Max connectivity				
	BCC	**LCC**	**C1**	**C2**	**C3**	**BCC**	**LCC**	**C1**	**C2**	**C3**
Total rainfall (P)	0.79	0.91	0.90	0.75	0.93	0.60	0.61	0.66	-	0.46
Pre-event streamflow	-	-	0.30	-	-	-	-	0.29	-	-
Pre-event connectivity	-	-	-	-	-	-	0.61	0.29	-	-
Max 1-hour intensity	-	0.55	0.69	-	0.56	0.41	-	0.57	-	0.33
Mean 1-hour intensity	-	-	0.54	-	0.41	-	-	0.34	-0.45	-
Max streamflow	0.90	0.91	0.81	0.75	0.93	0.71	0.77	0.63	-	0.47
Max connectivity	0.77	0.74	0.69	0.53	0.46					
Duration	0.94	0.67	0.54	0.85	0.28	0.64	-	0.40	0.62	-
AP1	-	-	-	-	-	-	-	-	0.47	-
AP2	-	-	-	-	-	0.44	-	0.25	0.58	-
AP3	-	-	-	-	-	-	-	-	0.55	-
AP4	-	-	-	-	-	-	-	-	0.46	-
P+AP1	0.85	0.89	0.86	0.71	0.90	0.69	0.71	0.69	0.48	0.41
P+AP2	0.84	0.77	0.79	0.68	0.81	0.73	0.81	0.69	0.49	0.42
P+AP3	0.75	0.60	0.71	0.62	0.66	0.69	0.77	0.64	0.56	0.32
P+AP4	0.71	0.56	0.67	0.58	0.67	0.70	0.76	0.59	0.55	0.34
Hysteresis index	-	-0.56	-	0.47	0.60	0.40	-	-	-	-
Hysteresis area	-	0.45	-	-	-0.62	-	-	-	-	-

Table 7.1. Significant Spearman rank correlation coefficients ($p < 0.05$) computed between stormflow and maximum connectivity and characteristics of the rainfall-runoff events.

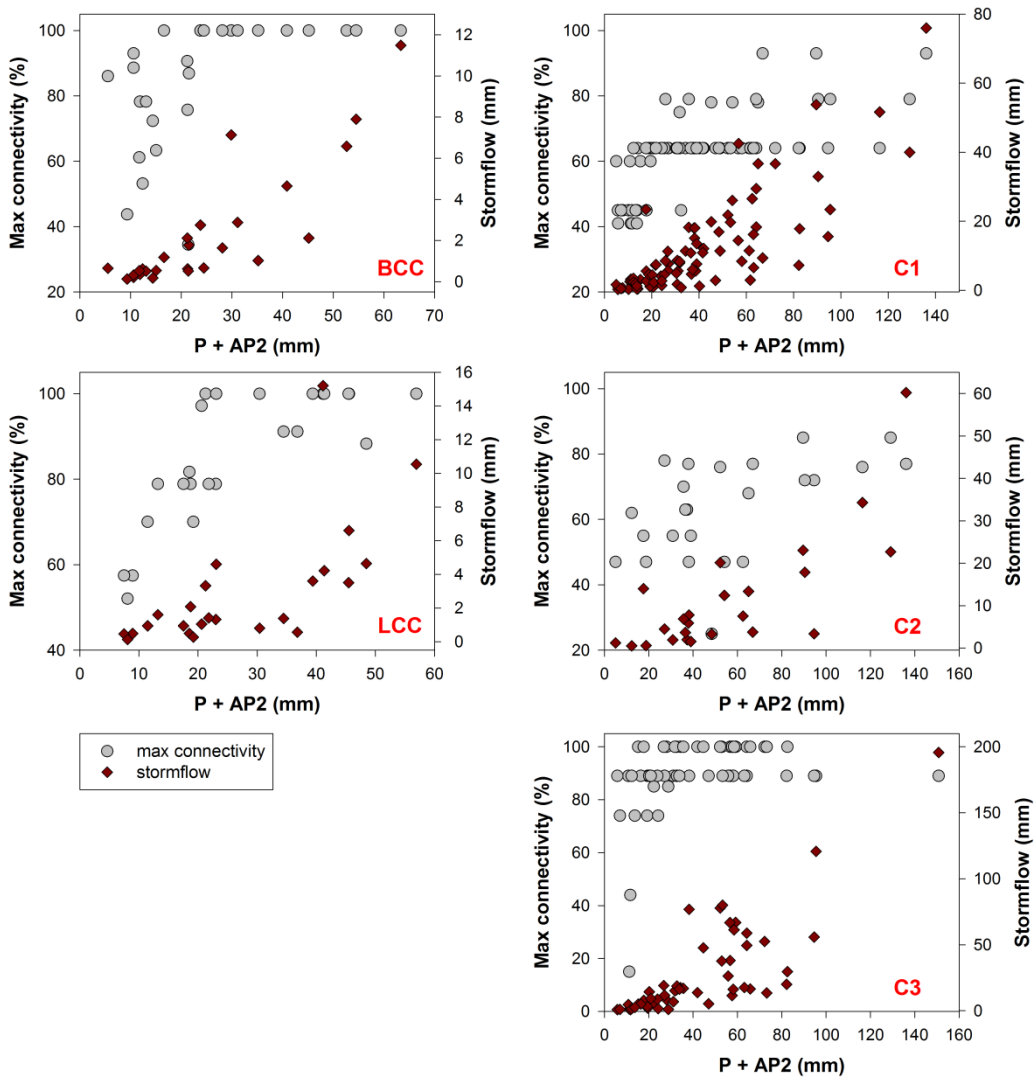

Fig. 7.4. Relation between sum of rainfall amount and antecedent precipitation in the previous two days (P+AP2) and maximum connectivity and between P+AP2 and stormflow of rainfall-runoff events.

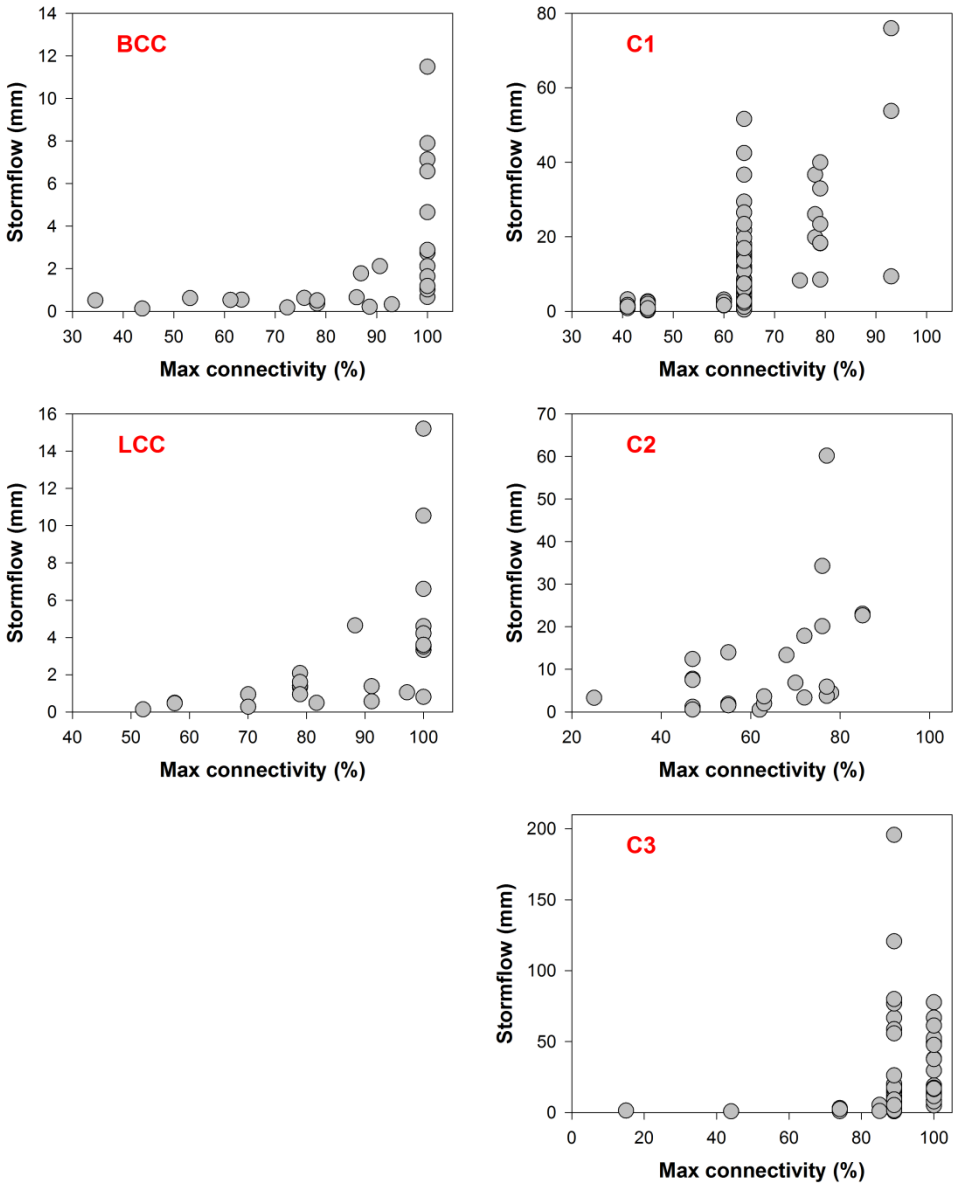

Fig. 7.5. Relation between maximum connectivity and stormflow of rainfall-runoff events.

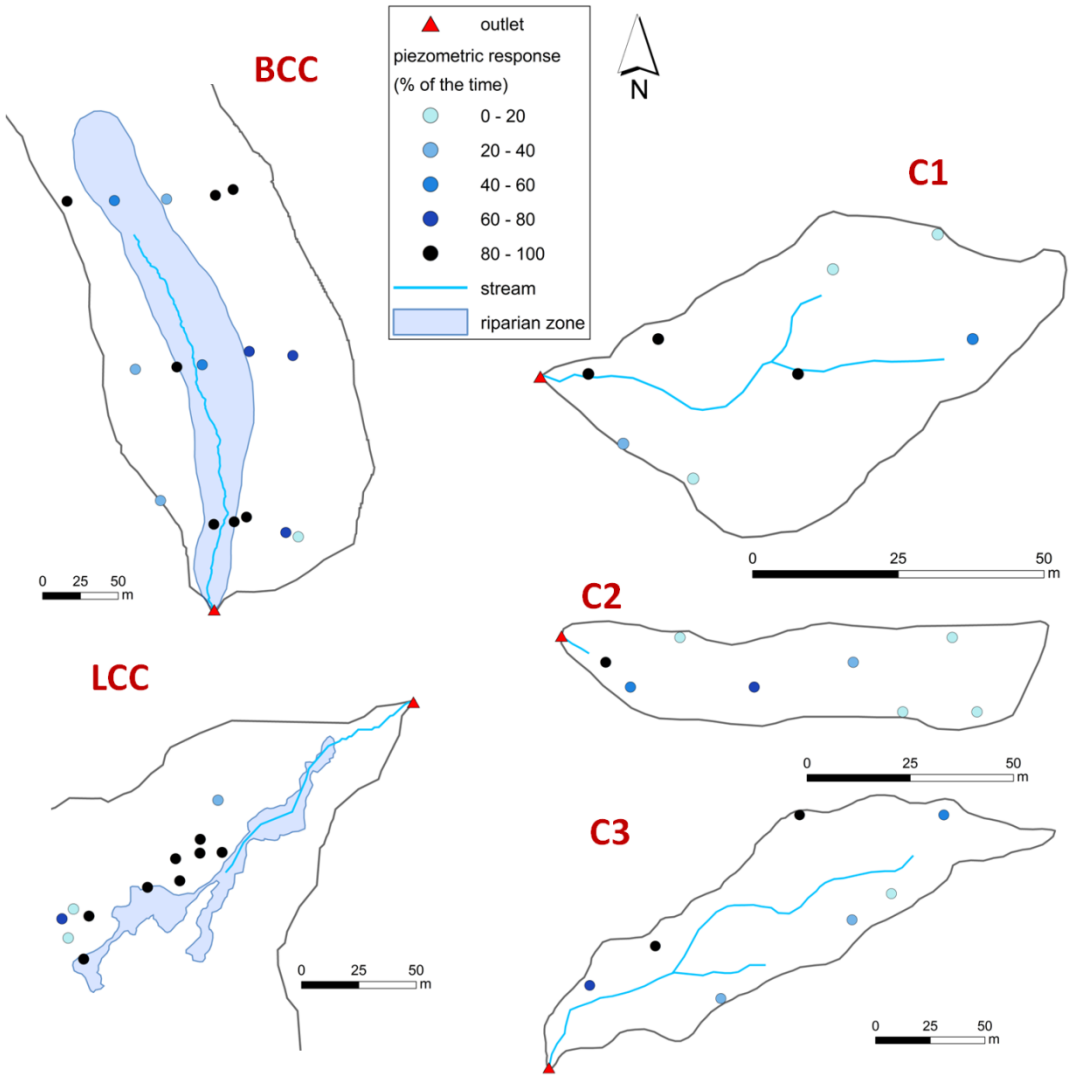

Fig. 7.6. Frequency of total time that a piezometer was active in BCC, LCC, C1, C2 and C3 catchment.

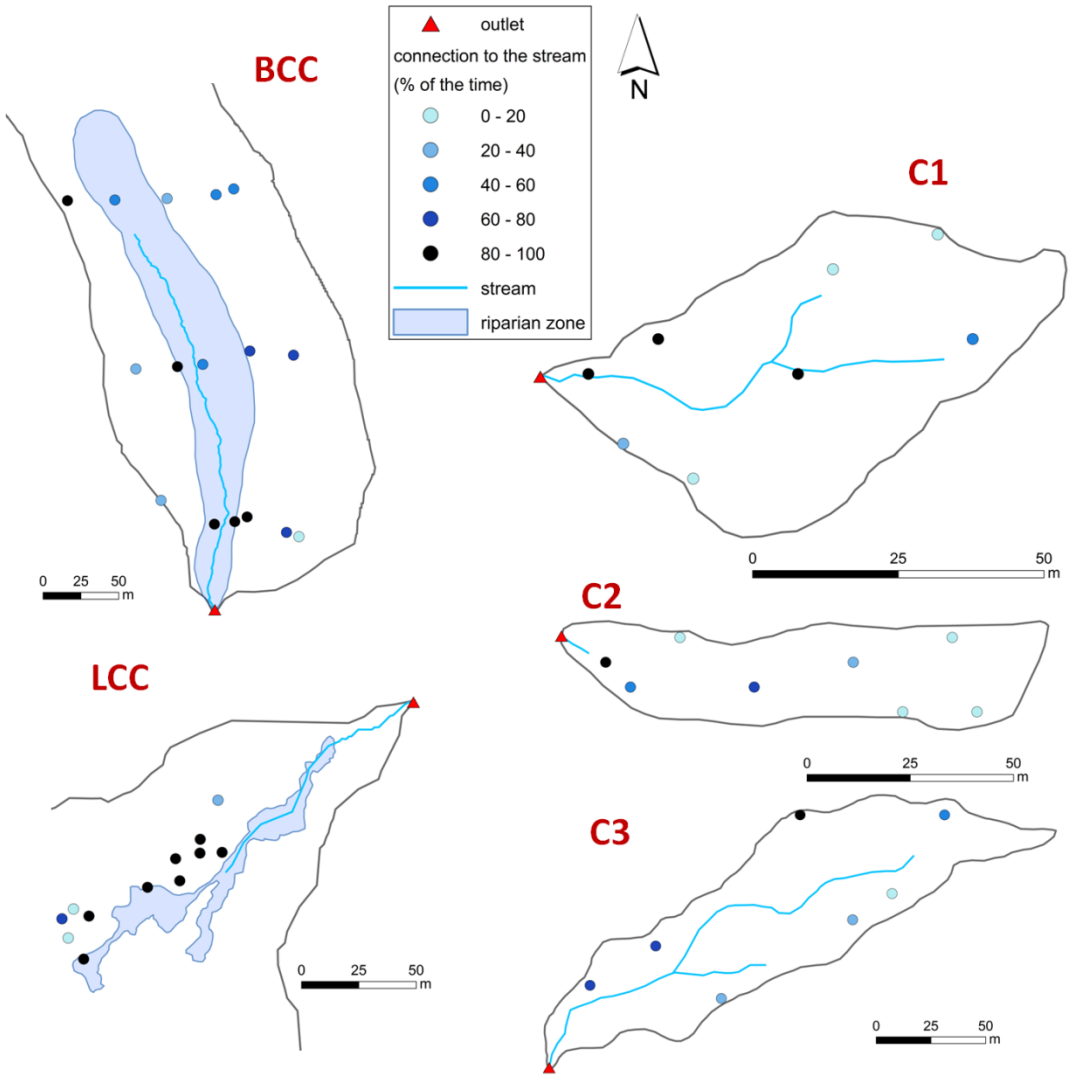

Fig. 7.7. Frequency of total time that a piezometer was connected to the stream in BCC, LCC, C1, C2 and C3 catchment.

	Piezometric response (% of the time)					Connection to the stream (% of the time)				
	BCC	**LCC**	**C1**	**C2**	**C3**	**BCC**	**LCC**	**C1**	**C2**	**C3**
Flow accumulation (D8)	0.61	-	-	-	-	0.54	-	-	-	-
Flow accumulation (based on multi triangular flow directions)	-	-	0.90	0.76	-	-	-	0.90	0.76	-
Max slope (%)	-	-	-0.79	-	-	-	-	-0.79	-	-
Max slope (°)	-	-	-0.79	-	-	-	-	-0.79	-	-
Curvature	-	-	-	-	-	-	-	-	-	-
Plan curvature	-	-	-	-0.74	-	-	-	-	-0.74	-
Profile curvature	-	-	-	-	-	-	-	-	-	-
TWI	-	-	0.93	0.81	-	-	-	0.93	0.81	-
Aspect	-	-	-	-	-	-	-	-	-	-
Overland flow distance to the nearest stream	-	-	-	-	-	-0.65	-	-	-	-
Horizontal component of the overland flow distance to the nearest stream	-	-	-	-	-	-0.66	-	-	-	-
Vertical component of the overland flow distance to the nearest stream	-	-	-	-	-	-0.68	-	-	-	-

Table 7.2. Significant Spearman rank correlation coefficients ($p < 0.05$) computed between the frequency of total time during which piezometers were responding and topographic characteristics of piezometers and significant Spearman rank correlation coefficients computed between the frequency of total time during which piezometers were connected to the stream and topographic characteristics of piezometers.

Table 7.2 shows that for two Swiss pre-alpine catchments (C1 and C2) the duration that piezometers were connected to the stream was significantly correlated to the local and upslope site characteristics, such as the topographic wetness index, local slope and curvature. For the

dolomitic catchment with the largest riparian zone (BCC), the time that piezometers were connected to the stream was correlated with downslope site characteristics, such as the vertical distance to the nearest stream.

8. APPLICATION AND TESTING OF THE HYSTERESIS INDEX FOR HYDROLOGICAL VARIABLES AT THE RUNOFF EVENT TIMESCALE

8.1. Application to synthetic data

We used synthetic loops to test the ability of the hysteresis index h, ΔA_{min} and ΔA_{max} to quantify the direction and the size of the loops. We also compared the index to *i)* the H index developed by Langlois et al. (2005), *ii)* HI_{mid} computed according to Lawler et al. (2006) and *iii)* its modified version, HI_{mean}, where instead of using the ratio of the dependent variable at the mid-point of x, the ratio is averaged for multiple pairs, and *iv)* the HI index developed by Aich et al. (2014) (Tables 8.1.1 and 8.1.2). We set equal-width intervals of 0.05, from $u = 0$ to $u = 1$, for the computation of h. The selected independent variable points for the computation of HI_{mean} were similarly set from 0.05 to 0.95 in equal intervals of 0.05. The results show that h, Langlois et al. (2005)'s H index, Aich et al. (2014)'s HI index and Lawler et al. (2006)'s HI_{mid} were able to detect the direction of the loops correctly (clockwise or anti-clockwise) (Table 8.1.1). h, HI_{mid} (Lawler et al., 2006) and HI (Aich et al., 2014) also provided symmetry across the range of clockwise and anti-clockwise hysteretic loops. HI_{mean} (Lawler et al., 2006) was also able to detect the direction correctly but the index was affected by the presence of at least one value of zero in the ratio (either in the numerator or denominator) (Table 8.1.1). In hydrological applications the dependent variable can be equal to zero (e.g., water table and isotopic composition or tracer concentration) or not change from its initial value, therefore methods that are not sensitive to this are preferable.

Hysteretic loop		h this study	H Langlois et al., 2005	HI_{mid} Lawler et al., 2006	HI_{mean} Lawler et al., 2006	HI Aich et al., 2014
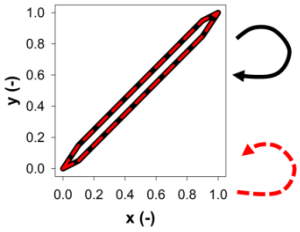	**A1**	**0.09**	**1.20**	**0.22**	**0.47**	**0.07**
	A2	**-0.09**	**0.83**	**-0.22**	**-0.47**	**-0.07**
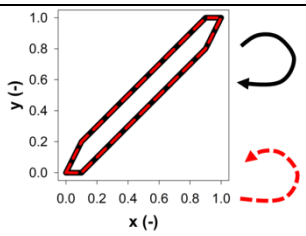	**B1**	**0.18**	**1.44**	**0.50**	*	**0.14**
	B2	**-0.18**	**0.69**	**-0.50**	*	**-0.14**
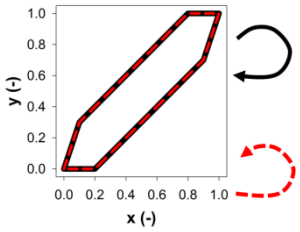	**C1**	**0.34**	**2.03**	**1.33**	*	**0.28**
	C2	**-0.34**	**0.49**	**-1.33**	*	**-0.28**

* the index was affected by a division that included a zero (either in the numerator or the denominator)

Table 8.1.1. Synthetic loops with a different area (A, B, C) and direction (clockwise: black solid line and loop name in black; anti-clockwise: red dashed line and loop name in red) used for testing the hysteresis indices and the corresponding values of h (equation 3.4.6), the H index developed by Langlois et al. (2005), the HI_{mid} and HI_{mean} indices of Lawler et al. (2006), and the HI index of Aich et al. (2014).

We also tested the indices for synthetic eight-shaped loops (Table 8.1.2). The methods for the computation of H (Langlois et al., 2005), HI_{mid} (Lawler et al., 2006) and HI (Aich et al., 2014) do not give information about complex loops but the indices were able to detect the perfect symmetry ($H = 1$, $HI_{mid} = 0$ and $HI = 0$) for the symmetric loops (B1 and B2 in Table 8.1.2). The index h and the associated values of ΔA_{min} and ΔA_{max} can characterise the direction correctly for the eight-shaped loops with an identifiable main direction (A1, A2, C1, C2, D1, D2, E1, E2 in Table 8.1.2) and identify the symmetry of the shape (B1 and B2). The values of HI_{mean} were different for B1 and B2 because the computation is based on ratios, which do not perfectly identify the symmetry of the shape. A comparison of the loops with the same area and main direction but with a different location of the largest loop (i.e., A1 and C2, and A2 and C1) shows that the value of HI_{mean} depends on the position of the largest portion of the loop (i.e., close or far from the peak of x) and the skewness of the distribution of the ratios (D1 and D2 in Table 8.1.2). The values of h, H, HI_{mid} and HI_{mean} reflected the different areas of the

loops (e.g., C2, D2 and E2 and C1, D1 and E1 in Table 8.1.2) and thus the differences in the extent of hysteresis. On the contrary, HI (Aich et al., 2014) did not detect differences in the shape or the extent of the loops.

Hysteretic loop		h	H	HI_{mid}	HI_{mean}	HI
		this study	Langlois et al., 2005	Lawler et al., 2006	Lawler et al., 2006	Aich et al., 2014
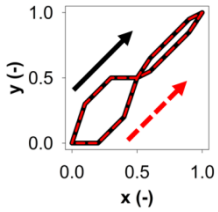	**A1**	**0.10**	**1.22****	**0.00****	*****	**0.28****
	A2	**-0.10**	**0.82****	**0.00****	*****	**-0.28****
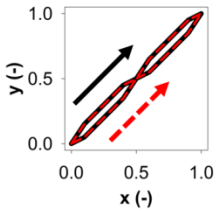	**B1**	**0.00**	**1.00****	**0.00****	**0.32**	**0.00****
	B2	**0.00**	**1.00****	**0.00****	**-0.32**	**0.00****
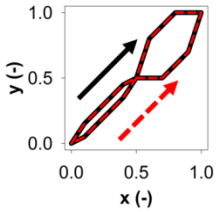	**C1**	**-0.10**	**0.82****	**0.00****	**0.13**	**-0.28****
	C2	**0.10**	**1.22****	**0.00****	**-0.13**	**0.28****
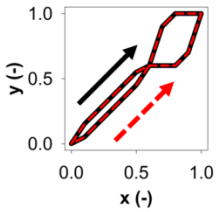	**D1**	**-0.05**	**0.90****	**0.22****	**0.24**	**-0.28****
	D2	**0.05**	**1.11****	**-0.22****	**-0.24**	**0.28****
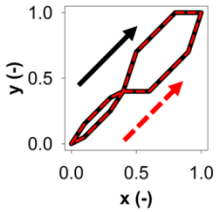	**E1**	**-0.15**	**0.74****	**-0.75****	**-0.03**	**-0.28****
	E2	**0.15**	**1.35****	**0.75****	**0.03**	**0.28****

* the index was affected by a division that included a zero (either in the numerator or the denominator)
** the index did not identify the eight-shaped loop

Table 8.1.2. The synthetic eight-shaped loops used for testing the hysteresis indices with the values of h, the index developed by Langlois et al. (2005), H, the indices developed by Lawler et al. (2006), HI_{mid}, and its modified version HI_{mean}, and the index of Aich et al. (2014), HI. The arrows indicate the starting points of the loops: for values of x close to 0 on the rising limb, the black solid loops have larger values of y compared to the red dashed loops.

8.2. Application to field data: identification of the different hysteretic relations

The hysteresis index correctly represented the type of hysteretic loop: the clockwise loop (Fig. 3.4.3a) had $h > 0$ and the anti-clockwise loops (Fig. 3.4.3b, d and f) had $h < 0$ (Table 8.2.1). The range of $\Delta A_{[i,j]}$ confirmed that the clockwise loop had all $\Delta A_{[i,j]} > 0$ (Fig. 3.4.3a), the anti-clockwise loops had all $\Delta A_{[i,j]} < 0$ (Fig. 3.4.3b, d and f) and the eight-shaped hysteretic patterns were characterized by $\Delta A_{min} < 0$ and $\Delta A_{max} > 0$ (Fig. 3.4.3c and e) (Table 8.2.1). In particular, the values of ΔA_{min} and ΔA_{max} were useful to identify the eight-shaped loops (Fig. 3.4.3c and e), where a small change in the hysteretic pattern occurred near the streamflow peak.

Examples in Fig. 3.4.3	Variables (x; y)	Sign of dependent variable	Hysteresis class	ΔA_{min} (-)	ΔA_{max}(-)	h (-)
a)	streamflow; soil moisture	+	I	0.001	0.018	0.128
b)	streamflow; soil moisture	+	IV	-0.049	-0.003	-0.634
c)	streamflow; water table	-	II	-0.015	0.009	0.021
d)	streamflow; water table	-	IV	-0.044	-0.006	-0.567
e)	streamflow; δ^2H	-	II	-0.003	0.038	0.383
f)	streamflow; EC	+	VIII	-0.026	-0.004	-0.360

Table 8.2.1. Independent and dependent variables, sign of the dependent variable, hysteresis classes (see Table 3.4.1), and values of ΔA_{min}, ΔA_{max} and h for the examples shown in Fig. 3.4.3.

We also computed the indices developed by Langlois et al. (2005), Lawler et al. (2006) and Aich et al. (2014) for the six examples (Table 8.2.2). The three indices captured the direction of the loops correctly when the dependent variables were expressed by positive signs. The direction of the loops with dependent variables with a negative sign (Fig. 3.4.3c-e) were not correctly identified without any additional normalization or conditional statements: H, HI_{mid} and HI_{mean} gave a wrong interpretation of the direction, while HI gave a correct interpretation of the direction but the normalization procedure reversed the loop. Eight-shaped hysteretic loops (Fig. 3.4.3c and e) could not be correctly detected by any of these previous indices.

Examples in Fig. 3.4.3	Hysteresis class	H - Langlois et al. (2005) (notes)	HI_{mid} - Lawler et al. (2006) (notes)	HI - Aich et al. (2014) (notes)
a)	I	1.040 (correct)	0.050 (correct)	0.051 (correct)
b)	IV	0.843 (correct)	-0.277 (correct)	-0.227 (correct)
c)	II	1.011 (theoretically incorrect because of the negative sign of the dependent variable; difficult interpretation because it is an eight-shaped loop)	-0.101 (theoretically incorrect because of the negative sign of the dependent variable; no information about the eight shape)	-0.136 (correct for the normalized loop, but the normalization reverses the original loop; no information about the eight shape)
d)	IV	1.475 (incorrect because of the negative sign of the dependent variable)	0.407 (incorrect because of the negative sign of the dependent variable)	0.734 (correct for the normalized loop, but the normalization reverses the direction of the original loop)
e)	II	0.900 (incorrect because of the negative sign of the dependent variable; also correlation coefficient < 0.90)	-0.111 (incorrect because of the negative sign of the dependent variable)	-0.269 (correct for the normalized loop, but the normalization reverses the direction of the original loop)
f)	VIII	0.983 (correct)	-0.026 (correct)	-0.029 (correct)

Table 8.2.2. Values for H (Langlois et al., 2005), HI_{mid} (Lawler et al. (2006) and HI (Aich et al., 2014) with notes about the interpretation of the direction of hysteretic loops for the examples shown in Fig. 3.4.3. The indices were applied without additional conditional statements or normalizations of the data. The values for ΔA_{min}, ΔA_{max} and h are shown in Table 8.2.1.

8.3. Temporal variability in the hysteretic relation between soil moisture and streamflow

The application of the hysteresis index to soil moisture and streamflow data for 30 events in the Ressi catchment showed that hysteretic loops between streamflow and riparian soil moisture (SM1 and SM2, Fig. 8.3.1) were generally clockwise, with a few anti-clockwise loops for events in May and June 2013. Conversely, hysteretic relations between streamflow and hillslope soil moisture (SM3 and SM4, Fig. 8.3.1) followed a seasonal pattern, with clockwise loops during large events in autumn and anti-clockwise loops occurring more commonly in spring and summer. Differences in the type of hysteretic loop for the hillslope and the riparian zone were most pronounced in late summer and late spring and smaller during the wet periods (autumn 2012 and early spring 2013) and at the start of the dry season (end of May 2013) (Fig. 8.3.2). Because previous studies showed a threshold relation between streamflow and the sum of antecedent wetness conditions and total rainfall (ASI+P) at the Ressi catchment (Penna et al.,

2015b), we investigated the relation between ASI+P and h for the four soil moisture measurement locations. The hysteresis index h for the hillslope sites was significantly correlated with ASI+P (ρ_s= 0.69 and 0.73 for SM3 and SM4, respectively, p < 0.01, n = 30) and also with event rainfall amount (ρ_s = 0.72 and 0.73 for SM3 and SM4, respectively, p < 0.01, n = 30). The hysteretic relation between hillslope soil moisture and streamflow tended to be clockwise for high values of ASI+P and anti-clockwise hysteresis for dry conditions and small events (Fig. 8.3.3). These seasonal changes in the direction of the hysteresis suggest that streamflow generally peaked before hillslope soil moisture during dry periods and small rainfall events, while hillslope soil moisture peaked earlier than streamflow during the wet period. Runoff coefficients were also positively correlated with h, with stronger correlations for the hillslope than for the riparian zone (ρ_s = 0.50, 0.33, 0.67 and 0.86 for SM1 (p < 0.01), SM2 (p < 0.10), SM3 (p < 0.01) and SM4 (p < 0.01), respectively, n = 30).

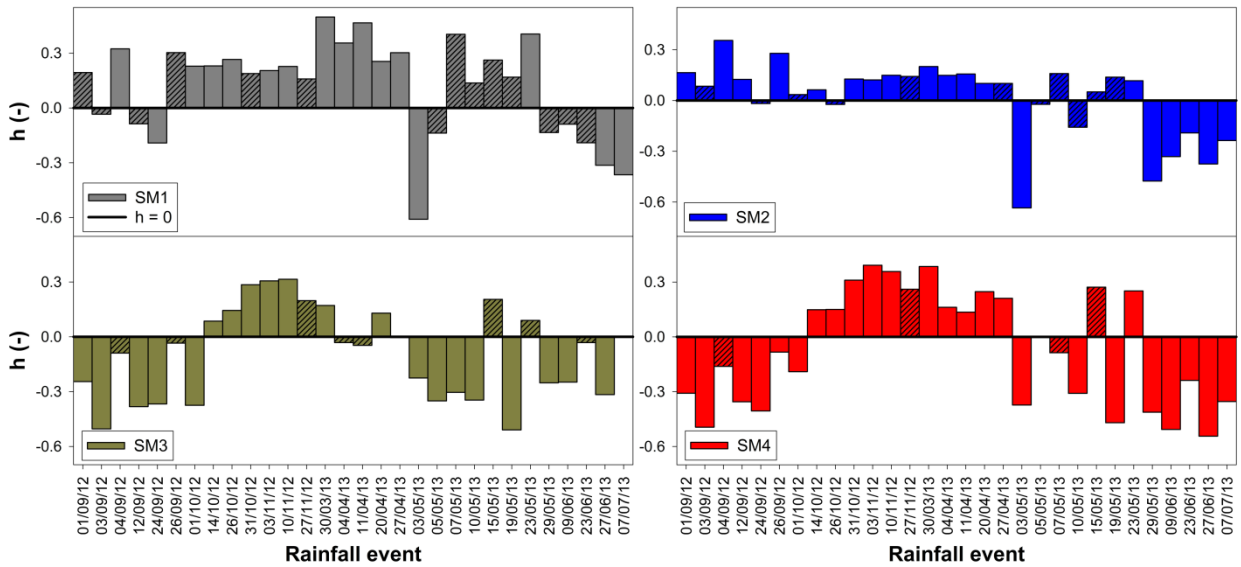

Fig. 8.3.1. Values of the hysteresis index (h) computed for the streamflow-soil moisture relations at four different locations (SM1: riparian zone; SM2: footslope; SM3: midslope; SM4: upper hillslope) in the Ressi catchment. The horizontal black line represents the threshold between mainly clockwise (> 0) and anti-clockwise (< 0) loops. Shaded bars indicate eight-shaped or complex loops.

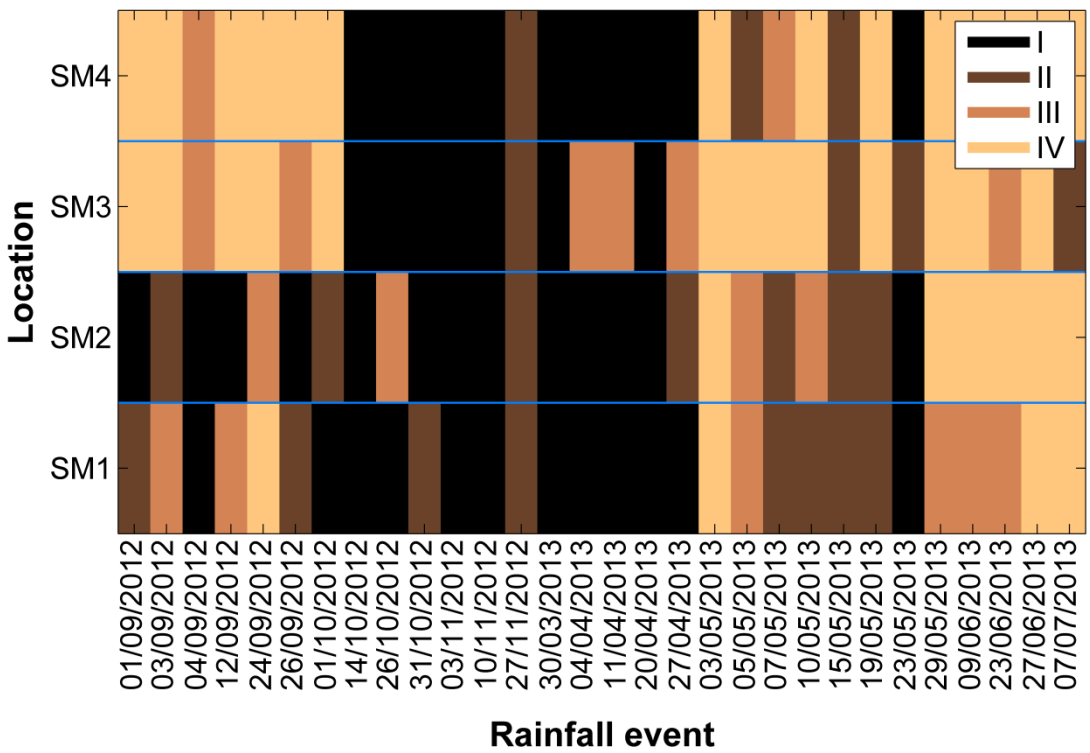

Fig. 8.3.2. The hysteresis classes for the 30 rainfall-runoff events for the relation between streamflow and soil moisture at four different locations along the riparian-hillslope transect in Ressi (SM1: riparian zone; SM2: footslope; SM3: midslope; SM4: upper hillslope; I = clockwise loop; II = eight-shaped or complex loop with a predominant clockwise loop; III = eight-shaped or complex loop with a predominant anti-clockwise loop; IV = anti-clockwise loop).

The relation between h and ASI+P for the riparian sites was more scattered than for the hillslope sites (ρ_s= 0.43 and 0.16 for SM1 ($p < 0.05$) and SM2 ($p > 0.10$), respectively, n = 30), suggesting that hysteresis between streamflow and riparian soil moisture was not predominantly related to antecedent wetness conditions and rainfall amount. Instead, the hysteresis index for the relation between streamflow and riparian soil moisture at SM1 was negatively correlated with the average (ρ_s= -0.52, $p < 0.01$, n = 30) and maximum rainfall intensity (ρ_s= -0.55, $p < 0.01$, n = 30), implying that the time lag between streamflow and soil moisture decreased during high rainfall intensity events.

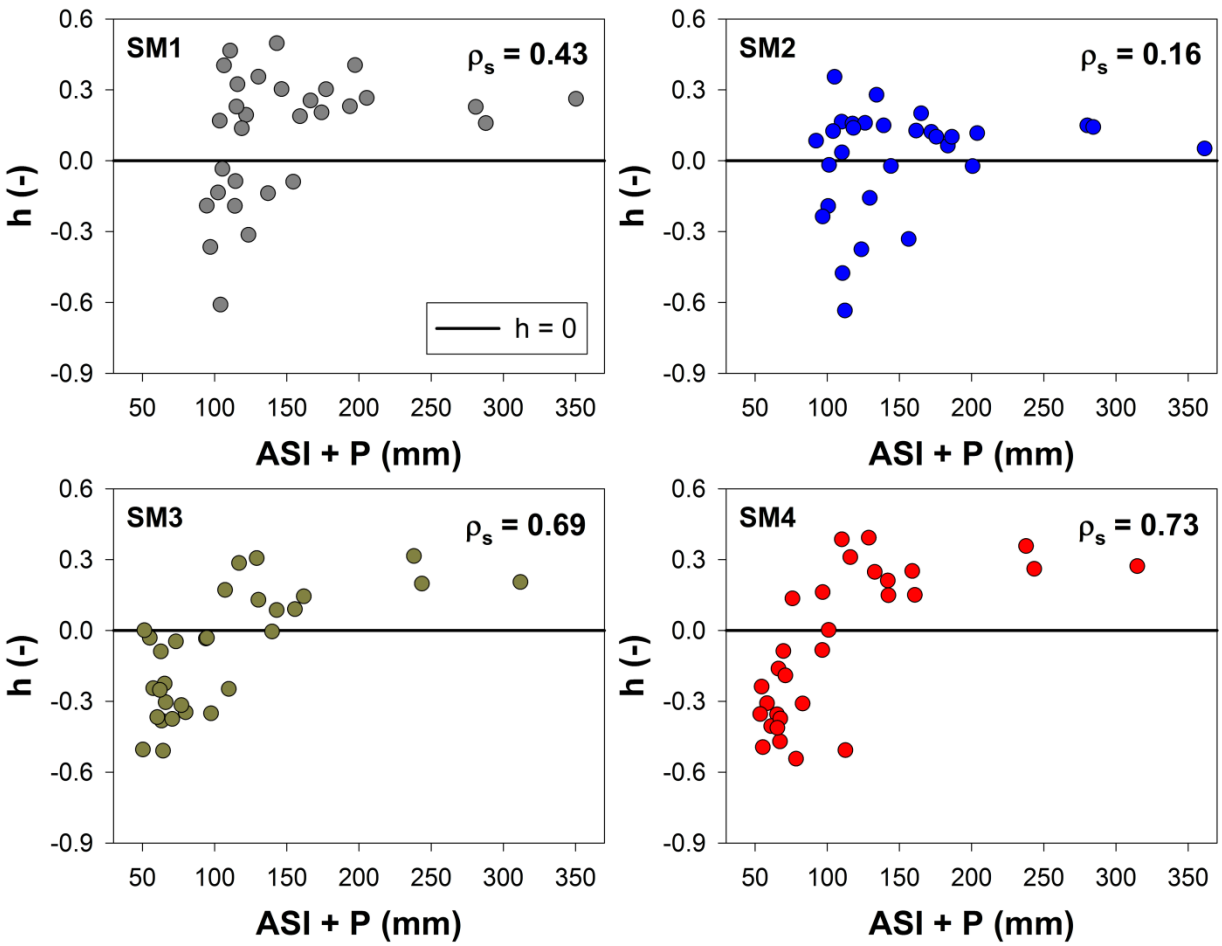

Fig. 8.3.3. Relation between the value of the hysteresis index (h) for the relation between streamflow and soil moisture and ASI+P for the different locations along the riparian-hillslope transect at the Ressi catchment. The horizontal black line represents the threshold between the mainly clockwise (> 0) and anti-clockwise (< 0) loops.

8.4. Sensitivity to the temporal resolution of the data

The sensitivity of the hysteresis index h and the determination of the hysteresis classes based on h and the associated values of ΔA_{min} and ΔA_{max} to the temporal resolution of the data was analysed for the hysteretic relation between streamflow and soil moisture at the mid-hillslope (SM3) location at Ressi. To determine the sensitivity of the hysteresis index to the temporal resolution of the data, data points from the streamflow and soil moisture datasets were systematically removed to simulate measurement intervals of 10-, 15-, 20- and 30-mins, and h, ΔA_{min} and ΔA_{max} were computed for the events with both the original data (5-min) and the simulated lower temporal resolution data. Cohen's kappa, κ (Cohen, 1960), was used to assess the agreement between the classifications of the hysteretic loops with the original and the simulated data:

$$\kappa = \frac{p_o - p_e}{1 - p_e} \quad (8.4.1)$$

where p_o is the relative observed agreement among the classifications with the original and the simulated data and p_e is the relative agreement due to chance. Cohen's kappa varies between 0 (there is no agreement other than what would be expected by chance) and 1 (perfect agreement between the classifications).

Overall, the analysis reveals a very good agreement between the classification with the original and the simulated data at a different temporal resolution (κ = 0.86, 0.86, 0.86 and 0.85 for the agreement between the classification with the original 5-min data and the 10-, 15-, 20- and 30-min interval data, respectively). Most loops were still classified similarly as for the original data (66.7% to 100% of loops identified using 10-, 15-, 20- or 30-minute data were classified similar as the loops based on the original data; Table 8.4.1). Only four hysteretic loops were classified differently after decreasing the temporal resolution of the data (i.e., rainfall-runoff events on 26/09/2012, 05/05/2013, 23/06/2013 and 07/07/2013). Two of these events (23/06/2013 and 07/07/2013) were characterized by a small change in soil moisture (only 0.25 and 0.29% for 23/06/2013 and 07/07/2013, respectively), one had a very steep rising limb (05/05/2013) with few data points on the rising limb, while the fourth event (26/09/2012) had a loop with a very complex shape. Decreasing the temporal resolution of the data for these events significantly influenced the number of data points on the rising limb and, not surprisingly, significantly affected the shape of the hysteretic loops and the calculated values of h, ΔA_{min} and ΔA_{max}. Therefore, caution should be used when applying the index to events with only a few measurements on the rising (and the falling) limb.

a 10 min temporal resolution			Frequency (%)				b 15 min temporal resolution			Frequency (%)			
			I	II	III	IV				I	II	III	IV
			23.3	**13.3**	**20.0**	**43.3**				**23.3**	**13.3**	**20.0**	**43.3**
Frequency (%)	I	**23.3**	100.0	0.0	0.0	0.0	Frequency (%)	I	**23.3**	100.0	0.0	0.0	0.0
	II	**13.3**	0.0	75.0	16.7	0.0		II	**13.3**	0.0	75.0	16.7	0.0
	III	**23.3**	0.0	25.0	83.3	7.7		III	**23.3**	0.0	25.0	83.3	7.7
	IV	**40.0**	0.0	0.0	0.0	92.3		IV	**40.0**	0.0	0.0	0.0	92.3
c 20 min temporal resolution			Frequency (%)				d 30 min temporal resolution *			Frequency (%)			
			I	II	III	IV				I	II	III	IV
			23.3	**13.3**	**20.0**	**43.3**				**23.3**	**13.3**	**20.0**	**43.3**
Frequency (%)	I	**23.3**	100.0	0.0	0.0	0.0	Frequency (%)	I	**26.7**	100.0	0.0	16.7	0.0
	II	**13.3**	0.0	75.0	16.7	0.0		II	**10.0**	0.0	75.0	0.0	0.0
	III	**20.0**	0.0	0.0	83.3	7.7		III	**16.7**	0.0	25.0	66.7	0.0
	IV	**43.3**	0.0	25.0	0.0	92.3		IV	**40.0**	0.0	0.0	16.7	84.6

* the hysteresis index h was computed for 28 instead of 30 rainfall-runoff events because the application of the different temporal resolution resulted in the removal of the data point on the falling limb that corresponded to $u = 0.15$.

Table 8.4.1. Frequency of the 30 rainfall-runoff events belonging to the four hysteresis classes (I-IV) for the observed data (columns) and for data with a 10- (*a*), 15- (*b*), 20- (*c*) and 30-min (*d*) temporal resolution (rows). The inner squares show the percentage of loops from a certain class that were reclassified to that class when the temporal resolution of the data was changed. For instance, 83.3% of the type III loops based on the original 5-minute data were still characterized as a type III loop when using 10-minute, 15-minute or 20-minute data (panel a, b and c, respectively), while 16.7% of the type III loops were reclassified as a type II loop using 10-minute, 15-minute or 20-minute data (panel a, b and c, respectively). See Table 3.4.1 for the definition of hysteresis classes.

8.5. Sensitivity to noise in the data

We also studied the sensitivity of the hysteresis index to instrumental error or noise in the input data. Gaussian noise was simulated independently for streamflow and soil moisture by generating arrays of pseudo-random numbers whose elements were normally distributed (mean ≈ 0 and variance ≈ 1). The random numbers were scaled by 1% and 5%, multiplied by the original data and then added to the original values to generate a disturbed (noisy) signal.

We iterated the process 1000 times for each event and determined the hysteresis class and the value of h. The median and the interquartile ranges of h were compared to the value calculated for the original data.

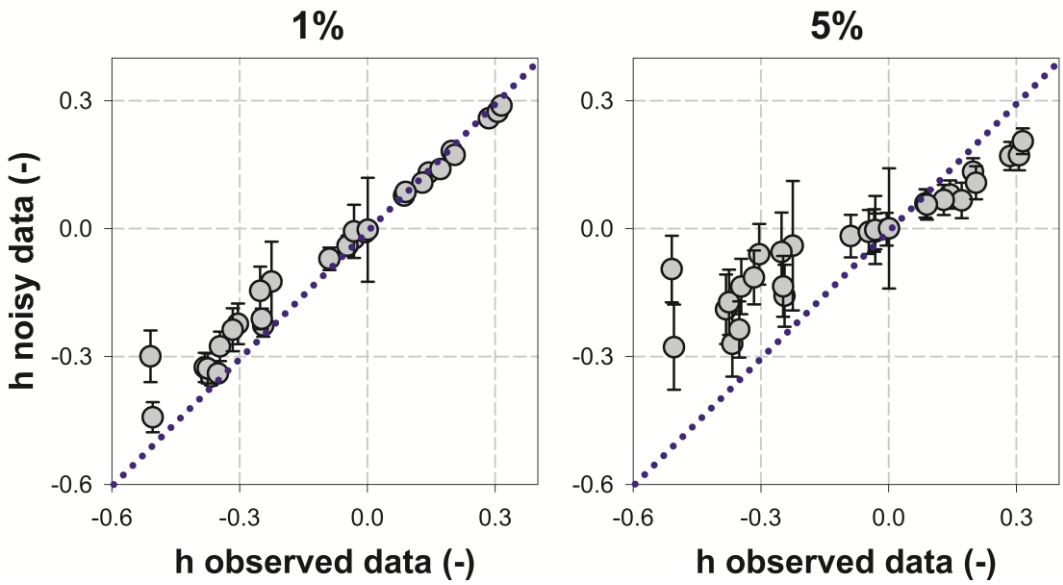

Fig. 8.5.1. Simulated and observed values of h for the relation between streamflow and soil moisture at the midslope (SM3 location) at Ressi catchment for the 30 studied rainfall-runoff events. Random instrumental noise was simulated 1000 times with a scaling factor of 1% (left) and 5% (right). The dots represent the median of the 1000 simulations, the error bars the interquartile range.

Cohen's kappa results suggest that there was a good (κ = 0.72) and a fair (κ = 0.29) agreement between the classifications with the original and the 1%- and 5%-scaled noisy data, respectively. The medians of h for the 1%-scaled noisy data were similar to h for the original data, but the interquartile ranges were large for some rainfall-runoff events (Fig. 8.5.1). For 27 out of the 30 events the most common hysteresis class for the simulations with 1% noise was similar to the hysteresis class obtained based on the original data (79.6% of agreement between the classifications) (Table 8.5.1). Conversely, the medians of h for the 5%-scaled noisy data and the value computed for the original data were similar for some events but different for other events (Fig. 8.5.1). The agreement of the classification of the hysteretic loops was also poorer than for the 1%-scaled noisy loops: the majority of the simulated loops corresponded to the classification obtained using the original data for only 16 events (44.4% of agreement between the classifications) (Table 8.5.1). The interquartile ranges of h were particularly large for rainfall-runoff events with small changes in streamflow and soil moisture and short events. These results suggest that the hysteresis index can be considered quite robust when

measurements errors occur for large and long rainfall events but that the index should be used with caution when noise or errors affect the two measurements during small events.

Rainfall event		Frequency (%)					Frequency (%)			
		I	II	III	IV		I	II	III	IV
01/09/12	1% scaling factor	0.0	0.0	0.0	**100.0**	5% scaling factor	0.0	0.1	35.7	**64.2**
03/09/12		0.0	0.0	0.0	**100.0**		0.0	0.0	13.9	**86.1**
04/09/12		0.0	0.1	**99.8**	0.1		0.0	33.3	**66.5**	0.2
12/09/12		0.0	0.0	0.7	**99.3**		0.0	0.0	**51.4**	48.6
24/09/12		0.0	0.0	0.0	**100.0**		0.0	0.0	4.5	**95.5**
26/09/12		0.0	3.2	**96.8**	0.0		0.1	44.0	**55.9**	0.0
01/10/12		0.0	0.0	0.0	**100.0**		0.0	0.3	**51.2**	48.5
14/10/12		**91.4**	8.6	0.0	0.0		9.6	**89.7**	0.7	0.0
26/10/12		**74.7**	25.3	0.0	0.0		10.0	**89.8**	0.2	0.0
31/10/12		**100.0**	0.0	0.0	0.0		**52.9**	47.1	0.0	0.0
03/11/12		**99.8**	0.2	0.0	0.0		46.8	**53.2**	0.0	0.0
10/11/12		**95.5**	4.5	0.0	0.0		**52.2**	47.8	0.0	0.0
27/11/12		5.9	**94.1**	0.0	0.0		16.7	**83.3**	0.0	0.0
30/03/13		**75.4**	24.6	0.0	0.0		3.0	**94.7**	2.3	0.0
04/04/13		0.0	2.5	**96.5**	1.0		0.0	41.8	**58.2**	0.0
11/04/13		0.0	1.6	**97.1**	1.3		0.0	40.8	**59.1**	0.1
20/04/13		**70.0**	30.0	0.0	0.0		5.2	**94.7**	0.1	0.0
27/04/13		0.0	21.0	**79.0**	0.0		0.1	48.2	**51.7**	0.0
03/05/13		0.0	4.0	**53.7**	42.3		2.8	32.9	**51.5**	12.8
05/05/13		0.0	0.0	0.0	**100.0**		0.0	0.0	23.7	**76.3**
07/05/13		0.0	0.0	38.4	**61.6**		0.0	12.9	**85.1**	2.0
10/05/13		0.0	0.0	46.9	**53.1**		0.0	0.3	**80.2**	19.5
15/05/13		6.2	**93.8**	0.0	0.0		10.3	**89.7**	0.0	0.0
19/05/13		0.0	0.0	34.2	**65.8**		0.0	5.7	**88.8**	5.5
23/05/13		0.0	**100.0**	0.0	0.0		0.7	**97.3**	2.0	0.0
29/05/13		0.0	0.3	**85.0**	14.7		0.0	21.0	**74.7**	4.3
09/06/13		0.0	0.0	22.2	**77.8**		0.0	0.1	**67.3**	32.6
23/06/13		0.0	44.4	**55.5**	0.1		0.8	47.1	**51.7**	0.4
27/06/13		0.0	0.0	**82.7**	17.3		0.0	0.9	**92.5**	6.6
07/07/13		13.4	**35.5**	34.7	16.4		14.0	**36.7**	34.8	14.5

Table 8.5.1. Frequency of the hysteresis classes (I-IV) for the 1000 simulations with noisy data for each rainfall event (left: 1% scaling factor; right: 5% scaling factor). Gray squares represent the hysteresis class for the observed data, bold values indicate the most frequently assigned hysteresis class with the noisy data for each rainfall event. See Table 3.4.1 for the definition of the hysteresis classes.

8.6. Comparison with previous indices

Several quantitative indices have been developed to characterize hysteresis in the past. Most of these indices were tested for the relation between streamflow and suspended sediment concentrations (e.g., Aich et al., 2014; Lawler et al., 2006; Langlois et al., 2005) or streamflow and solute concentrations (e.g., Butturini et al., 2006). The hysteresis index presented in this

study can be used for a wide range of (hydrological) variables, making it more versatile than most of the previously developed indices. The hysteresis index is consistent with the theoretical interpretation of the direction of the loops when using dependent variables that have positive (e.g., soil moisture, water level and EC) and negative values (e.g., isotopic composition and depth to water table) that increase (e.g., soil moisture or water table level) or decrease (e.g., EC, depth to water table) during a runoff event. There are a few similarities and substantial differences between the new index and the previous indices. The h index shares a common background with H (Langlois et al., 2005), since both methods are based on the computation of definite integrals. However, our method is more robust because it does not rely on the fitted regression lines for the rising and falling limb of the hydrograph in the hysteretic plot (Langlois et al., 2005). Noise in the data and some loop shapes (e.g., Fig. 3.4.3e) can result in a poor fit of the best regression equation to the observed data, influencing the value of H. Conversely, the application of the h index is less constrained by noise in the data and can be applied to complex hysteretic loops. The interpretation of the new versatile index is also similar to the index developed by Lawler et al. (2006). Both indices are positive for mainly clockwise loops and negative for anti-clockwise loops, providing symmetry across the range of clockwise and anti-clockwise hysteretic loops. Compared to HI_{mid} and HI_{mean} (Lawler et al., 2006), h solves the possible issue of initially non-changing dependent variables and is not affected by values that are equal to zero.

The first step for the computation of *HI* index of Aich et al. (2014) is a normalization of the data series, which is similar to the computation of our index. However, we use a minimum-maximum normalization that allows us to narrow the range of values to $[0,1]$, even for variables with a negative sign. Furthermore, the *HI* index of Aich et al. (2014) relies on data at the end of the runoff event, implying a degree of subjectivity because the length and the slope of the line connecting the last point to the peak of the independent variable changes depending on when the last data point is collected. This is particularly important when hysteretic relations are examined for non-continuous data, such as water quality samples, or a new event occurs shortly after the previous event. Because multiple values of $\Delta A_{[i,j]}$ are used for the calculation of h (i.e., h is a metric that summarises the shape of the loops), the computation does not depend on only two observed values, especially the last sample or the end of the event.

The *ΔR* index developed by Butturini et al. (2006) has been demonstrated to be efficient in its applications (e.g., Bieroza and Heathwaite, 2015; Butturini et al., 2006) because it relies on the direct measurement of the extent of the loops (i.e., the computation of the area) and on the

rotational parameter, R, which describes the direction of the hysteresis. However, R has to be determined by visual inspection of each loop (Bieroza and Heathwaite, 2015), which limits the automatic application of the index for large datasets. Conversely, the new hysteresis index and the indices developed by Langlois et al. (2005), Lawler et al. (2006) and Aich et al. (2014) can easily be implemented to automatically detect the direction of hysteresis and can thus be used to analyze large datasets or to compare measurements and model results.

The tests with synthetic data (Table 2 and 3) were useful to compare the index we presented here to the indices developed by Langlois et al. (2005), Lawler et al. (2006) and Aich et al. (2014). Although the indices are based on different methods to assess the 'fatness' of the loops (i.e., h and H on integrals computed for the rising and the falling limb, HI_{mid} and HI_{mean} on ratios, HI on the maximum distance between the rising and the falling limb of the hysteretic loop and the line that links the maximum value of the independent variable to the last data point), all of them captured the change in the extent of hysteresis for simple loops (Table 8.1.1). The comparison of the synthetic eight-shaped loops (Table 8.1.2) showed that HI_{mid} and HI are less useful to detect differences in the shape and the extent of eight-shaped loops because they characterize hysteresis at only one point of the independent variable (HI_{mid}) or by just two distances (HI).

The application of the different indices to different datasets from experimental catchments (Fig. 3.4.3) showed that unlike the previously developed indices, our index, h, and the associated values of ΔA_{min} and ΔA_{max}, can correctly identify all major hysteresis classes, including the eight-shaped loops, and is applicable to negative data and datasets where the dependent variable decreases during an event. It can even be applied when the dependent variable remains constant at the start of the event or has a value of zero. Additional conditional statements for HI_{mid} and HI_{mean} (Lawler et al., 2006) and H (Langlois et al., 2005), and a different normalization for HI (Aich et al., 2014) could allow these indices to also correctly identify the direction of the hysteresis for dependent variables with negative values. However, the additional conditional statements would make the outcome of the indices less intuitive.

8.7. Potential use and limits of the hysteresis index

The hysteresis index presented in this study provides objective and concise information on the direction and the shape of the hysteretic loops. Clockwise, anti-clockwise and eight-shaped loops are easily determined by four computational steps. The normalization of the two variables (step 1) is needed to compare different hysteretic loops and allows for the correct

interpretation of the direction of the hysteresis for different dependent variables. The computation of the definite integrals on the rising and the falling curve (step 2) and the differences between them ($\Delta A_{[i,j]}$; step 3) enables the determination of the direction and the shape of the loops, while the sum of the differences (step 4) summarizes the hysteretic loop and ensures that the index is not significantly influenced by outliers. The metrics introduced in steps 3 and 4 ($\Delta A_{[i,j]}$ and h) can easily be related to the characteristics of the runoff event, providing insight into the factors that lead to different hysteretic loops. These metrics can thus be used to assess changes in hysteresis in long data series with multiple events or to assess model performance. The computation of the index does not require a loop to be closed and h can be calculated for different independent-variable intervals. The index is therefore versatile and can be applied to a wide range of datasets.

The sensitivity analysis showed a high level of agreement between the classification based on the original data and the classifications obtained for data with a lower temporal resolution, suggesting that the sensitivity of the index to the temporal resolution of the measurements is low. However, caution should be used if the index is applied when only one or two measurements are available for the rising (or falling) limb. Application of the index to very noisy data (e.g., data that show large measurement errors and relatively small responses) should be done with caution as well.

Application of the versatile index to synthetic data highlighted the ability of the index to predict the direction of hysteresis and also showed that h becomes larger with an increasing extent of the loop.

Previous studies did not test the sensitivity of the various hysteresis indices to the temporal resolution of the data or noise in the measurements. However, this is important when indices are applied to many events or different catchments to study differences in runoff responses, or when indices are used for model calibration or validation. The results obtained from the application on field data and the sensitivity analyses revealed that the index introduced here is a powerful tool for the study of long-time series and comparative analyses of different runoff events because it was not very sensitive to noisy data or the temporal resolution of the data as long as the response was large relative to the noise and there were several data points on the rising and falling limb of the hydrograph. Consequently, the index can be used to study the seasonal variations in the hysteretic patterns (Bieroza and Heathwaite, 2015; Aich et al., 2014) or to compare hysteresis at different spatial scales or for different catchments (Smith and Dragovich, 2009). The hysteresis index can also be used in the assessment of models in their

ability to reproduce the internal behavior of catchments (e.g., Fovet et al., 2015). The only condition for a correct application of the index is that the independent variable has to increase from its starting value to the peak (i.e., the normalized data vary from 0 to 1). The index can therefore be used for a wide range of hydrological studies and in other fields across the earth system sciences.

Complex events characterized by multiple peaks are approximated by one overall hysteretic pattern because the computation of the index is based on the highest peak of the independent variable. The index therefore does not quantify the hysteretic loop of each individual runoff response that interrupts the recession curve of the first event. These multiple peak events will instead be classified as complex loops. However, the user can choose to analyze the different peaks of the independent variable as separate events and the corresponding hysteretic loops separately. This allows for the analysis of changes in hysteresis with each individual rainfall pulse or sub-event.

We used the index to detect seasonal changes in the direction of hysteresis between streamflow and soil moisture for 30 rainfall-runoff events in the Ressi catchment. The results showed seasonal changes in the direction of the hysteretic relation between hillslope soil moisture and streamflow, with the streamflow peak generally occurring before peak hillslope soil moisture during dry periods and small rainfall events, and after peak soil moisture during the wet period. These observations on the hysteretic relations between hillslope soil moisture and streamflow agree with previous studies on the role of hillslopes in generating runoff during wet conditions and large rainfall events (McGlynn et al., 2004; Wenninger et al., 2004; Ocampo et al., 2006; Penna et al., 2011, 2015b; von Freyberg et al., 2014) and show the value of analyzing hysteretic patterns to study (changes in) hydrological processes.

CONCLUSIONS

The comprehension of the hydrological response of a catchment is closely related to the observations of spatial and temporal patterns and the assessment of the underlying hydrological processes. Improving the knowledge of how structural characteristics of the landscape (e.g., topography, geology, soils and vegetation) interact in relation with the driving forces (precipitation and evapotranspiration) and the antecedent wetness conditions is fundamental for the prediction of floods, erosion and sedimentation processes and dispersion of pollutants. This thesis presents the results of the analysis of spatial and temporal variability of water content in the unsaturated and saturated zone in relation to streamflow dynamics to improve the understanding of the hydrological behavior of small catchments.

Understanding and characterizing the soil moisture spatial and temporal variability and its relevant physical controls is a main challenge in hydrological sciences. In this thesis the spatial variability was analyzed for soil moisture data at 0-30 and 0-60 cm depth collected over three years on a plot in Grugliasco (Po Plain, Northern Italy). The plot was divided into two subplots: one covered by grapevine plants, the other covered homogeneously by grass. Examination of the data showed higher soil moisture values in the vineyard than in the meadow, implying the influence of vegetation cover during the growing season; correspondingly, the spatial soil moisture variability was lower in the vineyard than in the meadow at 0-30 cm depth. Evaluation of the main physical controls on the spatial mean and the variability of soil moisture was carried out by using a simple bucket model, forced by using local rainfall and evapotranspiration data. The model was calibrated by using mean soil moisture daily time series over one year for the two sites at 0-30 cm depth. The model accuracy was verified for the other two years, showing a relatively good prediction capability. The model was also shown to be able to capture the main differences between the two sites in terms of spatial variability of soil moisture.

The spatial and temporal variability of soil moisture was also analyzed in relation to throughfall spatial patterns in a 500 m^2 plot on a forested hillslope dominated by beech and chestnut trees in the Italian pre-Alps. Throughfall was measured using two types of throughfall collectors: buckets and rain gauges. The collectors differed in size, number and spatial arrangement. The results from this experimental study on the representativeness of different collectors for monitoring throughfall amount and spatial variability showed that buckets and rain gauges measured similar throughfall amounts during rainfall events, except during the fall. However, findings indicate that different collectors and their spatial arrangement can lead to differences

in the quantified spatial variability of throughfall and presence of local clusters and outliers. These differences should be considered when planning throughfall monitoring strategies to determine the effects of throughfall on soil moisture and soil water chemistry, but need to be confirmed at other study sites as well.

Near-surface soil moisture was measured upslope of each bucket, at two depths (0-7 and 0-12 cm) before and after rainfall events. For the measured events throughfall and soil moisture spatial patterns were not significantly or only weakly correlated, likely due to the lateral and vertical redistribution of water in the soil profile during the 2-36 hour period between the end of the rainfall event and the start of the soil moisture measurements. The temporal stability of soil moisture was larger than the temporal stability of throughfall and they were also not significantly correlated. The patterns of temporal stability were also not related to canopy characteristics (openness and leaf area index), suggesting that the spatial variability in throughfall is probably linked to small scale characteristics of the canopy. The simple bucket model was used to test which combination of soil properties and vegetation characteristics leads to uncorrelated patterns of temporal stability of throughfall and soil moisture. The application of the model revealed that a large spatial variability in saturated hydraulic conductivity that is correlated with the spatial variability in leaf area index and root fraction weaken the correlation between throughfall and soil moisture patterns. The analysis of field data combined with the model application suggests that in this specific forested hillslope the spatial organization of soil moisture is dominated by a combination of soil properties and vegetation characteristics, rather than by the throughfall spatial patterns.

Saturation at the soil-bedrock interface or the rise of shallow groundwater into more permeable soil layers results in subsurface stormflow and can lead to hillslope-stream connectivity. Despite the importance of subsurface connectivity for streamflow and streamwater chemistry, the factors controlling its spatial and temporal variability are still poorly understood. Networks of spatially-distributed piezometers in five small (< 14 ha) headwater catchments in the Italian Dolomites and the Swiss pre-Alps were used to quantify and compare the spatial and temporal variability of subsurface connectivity and its relation to streamflow dynamics. Results showed that for two Swiss pre-alpine catchments the duration that piezometers were connected to the stream was significantly correlated to the local and upslope site characteristics, such as the topographic wetness index, local slope and curvature. For the dolomitic catchment with the largest riparian zone, the time that piezometers were connected

to the stream was correlated with downslope site characteristics, such as the vertical distance to the nearest stream. The temporal changes in the area of the catchment that was connected to the stream reflected the streamflow dynamics for all catchments. Subsurface connectivity increased during rainfall events but there was a short delay compared to streamflow, suggesting that other processes (e.g., direct channel precipitation, runoff from near stream saturated areas) contributed to streamflow at the beginning of the event. Groundwater levels declined later and slower than streamflow, resulting in complex but mainly anti-clockwise hysteretic relations between streamflow and the area that was connected to the stream. Threshold-like relations between maximum connectivity and total stormflow and between maximum connectivity and the sum of total rainfall plus antecedent rainfall were more evident for the dolomitic catchments, where the riparian zone is characterized by a groundwater table near the soil surface. A sudden increase in connectivity for these catchments could represent the connection of hillslopes to the stream. These preliminary results suggest that the delayed increase in subsurface connectivity relative to streamflow is likely not affected by the presence of a riparian zone. However, further analyses are needed to determine if the climate and/or morphology of the catchments affect the observed relations between subsurface connectivity and total stormflow.

Finally, this thesis attempted to develop an index for the quantification of hysteretic loops between hydrological variables at the runoff event timescale. The index provides information on the direction, the shape and the extent of the loop. The index was tested with synthetic data and field data from experimental catchments in Northern Italy. Hysteretic relations between streamflow (the independent variable) and soil moisture, depth to water table, isotopic composition and electrical conductivity of stream water (dependent variables) were correctly identified and quantified by the index. The objective quantification of hysteresis by the index allows for the automatic classification of hysteretic loops and thus the determination of differences in hydrological responses during different events. The index was used to examine the seasonal dynamics in the relation between streamflow and soil moisture and captured the switch in the direction of the loop with changes in event size and antecedent wetness conditions. The sensitivity of the index to the temporal resolution of the measurements and measurement errors was also tested. The index can successfully quantify hysteresis, except for very noisy data or when the temporal resolution of the measurements is not well suited to study hysteresis between the variables. Overall, this metric can be used to test if models

reproduce a similar seasonal variability in hysteresis between streamflow and soil moisture or to compare hydrological responses in different catchments or at different spatial scales.

REFERENCES

Aich V., Zimmermann A., Elsenbeer H., 2014. Quantification and interpretation of suspended-sediment discharge hysteresis patterns: how much data do we need? Catena, 122, 120-129. DOI: 10.1016/j.catena.2014.06.020

Albertson J.D., Montaldo N., 2003. Temporal dynamics of soil moisture variability: 1. Theoretical basis. Water Resources Research, 39, 1274. DOI: 10.1029/2002WR001616

Al-Kaisi M., Brun L., Enz J., 1989. Transpiration and evapotranspiration from maize as related to leaf area index. Agricultural and Forest Meteorology, 48, 111-116.

Ali G.A., Roy A.G., 2009. Revisiting hydrologic sampling strategies for an accurate assessment of hydrologic connectivity in humid temperate systems. Geography Compass, 3, 350-374. DOI: 10.1111/j.1749-8198.2008.00180.x

Allen D.M., Whitfield P.H., Werner A., 2010. Groundwater level responses in temperate mountainous terrain: regime classification, and linkages to climate and streamflow. Hydrological Processes, 24, 3392-3412. DOI: 10.1002/hyp.7757

Ambroise B., 2004. Variable 'active' versus 'contributing' areas or periods: a necessary distinction. Hydrological Processes, 18, 1149-1155. DOI: 10.1002/hyp.5536

Andermann C., Longuevergne L., Bonnet S., Crave A., Davy P., Gloaguen R., 2012. Impact of transient groundwater storage on the discharge of Himalayan rivers. Nature Geoscience, 5, 127-132. DOI: 10.1038/NGEO1356

Anselin L., 1995. Local indicators of spatial association-LISA. Geographical Analysis, 27, 93–115.

ARPAV, 2005. Carta dei suoli del Veneto. ARPAV – Osservatorio Regionale Suolo, Castelfranco Veneto (TV).

Aubert A.H., Gascuel-Odoux C., Merot P., 2013. Annual hysteresis of water quality: a method to analyse the effect of intra- and inter-annual climatic conditions. Journal of Hydrology, 478, 29-39. DOI: 10.1016/j.jhydrol.2012.11.027

Baudena M., Bevilacqua I., Canone D., Ferraris S., Previati M., Provenzale A., 2012. Soil water dynamics at a midlatitude test site: Field measurements and box modeling approaches. Journal of Hydrology, 414-415, 329-340. DOI: 10.1016/j.jhydrol.2011.11.009

Bieroza M.Z., Heathwaite A.L., 2015. Seasonal variation in phosphorous concentration-discharge hysteresis inferred from high-frequency in situ monitoring. Journal of Hydrology, 524, 333-347. DOI: 10.1016/j.jhydrol.2015.02.036

Blaen P.J., Hannah D.M., Brown L.E., Milner A.M., 2013. Water temperature dynamics in High Arctic river basins. Hydrological Processes, 27, 2958-2972. DOI: 10.1002/hyp.9431

Blume T., van Meerveld H.J., 2015. From hillslope to stream: methods to investigate subsurface connectivity. Wiley Interdisciplinary Reviews: Water, 2, 177-198. DOI: 10.1002/wat2.1071

Borga M., Boscolo P., Zanon F., Sangati M., 2007. Hydrometeorological analysis of the August 29, 2003 flash flood in the eastern Italian Alps. Journal of Hydrometeorology, 8, 1049-1067. DOI: 10.1175/JHM593.1

Bouten W., Heimovaara T.J., Tiktak A., 1992. Spatial patterns of throughfall and soil-water dynamics in a Douglas-fir stand. Water Resources Research, 28, 3227-3233.

Bracken L.J., Croke J., 2007. The concept of hydrological connectivity and its contribution to understanding runoff-dominated geomorphic systems. Hydrological Processes, 21, 1749-1763. DOI: 10.1002/hyp.6313

Bracken L.J., Wainwright J., Ali G.A., Tetzlaff D., Smith M.W., Reaney S.M., Roy A.G., 2013. Concepts of hydrological connectivity: Research approaches, pathways and future agendas. Earth-Science Reviews, 119, 17-34. DOI: 10.1016/j.earscirev.2013.02.001

Brevik E.C., Batten R.A., 2012. Evaluation of the FieldScout TDR300 for determining volumetric water content in sandy South Georgia soils. Soil Horizons, 53, 27-30. DOI: 10.2136/sh12-05-0018

Brierley G.J., Fryirs K., Jain V., 2006. Landscape connectivity: the geographic basis of geomorphic applications. Area, 38, 165-174. DOI: 10.1111/j.1475-4762.2006.00671.x

Briggs M.A., Day-Lewis F.D., Ong J.B., Harvey J.W., Lane J.W., 2014. Dual-domain mass-transfer parameters from electrical hysteresis: Theory and analytical approach applied to laboratory, synthetic streambed, and groundwater experiments. Water Resources Research, 50, 8281-8299. DOI: 10.1002/2014WR015880

Brocca L., Melone F., Moramarco T., Morbidelli R., 2009. Soil moisture temporal stability over experimental areas in Central Italy. Geoderma, 148, 364-374. DOI: 10.1016/j.geoderma.2008.11.004

Brocca L., Melone F., Moramarco T., Morbidelli R., 2010. Spatial-temporal variability of soil moisture and its estimation across scales. Water Resources Research, 46. DOI: 10.1029/2009WR008016

Brocca L., Morbidelli R., Melone F., Moramarco T., 2007. Soil moisture spatial variability in experimental areas of central Italy. Journal of Hydrology, 333, 356-373. DOI: 10.1016/j.jhydrol.2006.09.004

Bronstert A., Bárdossy A., 1999. The role of spatial variability of soil moisture for modelling surface runoff generation at the small catchment scale. Hydrology and Earth System Sciences, 3, 505-516.

Burt T.P., Worrall F., Howden N.J.K., Anderson M.G., 2014. Shifts in discharge-concentration relationships as a small catchment recovers from severe drought. Hydrological Processes, Early View. DOI: 10.1002/hyp.10169

Butturini A., Gallart F., Latron J., Vazquez E., Sabater F., 2006. Cross-site comparison of variability of DOC and nitrate c-q hysteresis during the autumn-winter period in three Mediterranean headwater streams: a synthetic approach. Biogeochemistry, 77, 327-349. DOI: 10.1007/s10533-005-0711-7

Campbell G., 1974. A simple method for determining unsaturated conductivity from moisture retention data. Soil Science, 117 (6), 311-314.

Camporese M., Penna D., Borga M., Paniconi C., 2014. A field and modeling study of nonlinear storage-discharge dynamics for an Alpine headwater catchment. Water Resources Research, 50, 806-822. DOI: 10.1002/2013WR013604

Carlyle-Moses D.E., Lishman C.E., 2015. Temporal persistence of throughfall heterogeneity below and between the canopies of juvenile lodgepole pine (*Pinus contorta*). Hydrological Processes, 29, 4051-4067. DOI: 10.1002/hyp.10494

Carturan L., Cazorzi F., Dalla Fontana G., 2012. Distributed mass-balance modelling on two neighbouring glaciers in Ortles-Cevedale, Italy, from 2004 to 2009. Journal of Glaciology, 58, 467-486. DOI: 10.3189/2012JoG11J111

Cartwright I., Gilfedder B., Hofmann H., 2014. Contrasts between estimates of baseflow help discern multiple sources of water contributing to rivers. Hydrology and Earth System Sciences, 18, 15-30. DOI: 10.5194/hess-18-15-2014

Ciccarelli N., von Hardenberg J., Provenzale A., Ronchi C., Vargiu A., Pelosini R., 2008. Climate variability in north-western Italy during the second half of the 20th century. Global and Planetary Change, 63, 185-195. DOI: 10.1016/j.gloplacha.2008.03.006

Coenders-Gerrits A.M.J., Hopp L., Savenije H.H.G., Pfister L., 2013. The effect of spatial throughfall patterns on soil moisture patterns at the hillslope scale. Hydrology and Earth System Sciences, 17, 1749–1763. DOI:10.5194/hess-17-1749-2013

Cohen J., 1960. A coefficient of agreement for nominal scales. Educational and Psychological Measurement, 20, 37-46. DOI: 10.1177/001316446002000104

Cosh M.H., Jackson T.J., Bindlish R., Prueger J.H., 2004. Watershed scale temporal and spatial stability of soil moisture and its role in validating satellites estimates. Remote Sensing of Environment, 92, 427-435. DOI: 10.1016/j.rse.2004.02.016

Cotler H., Ortega-Larrocea M.P., 2006. Effects of land use on soil erosion in a tropical dry forest ecosystem, Chamela watershed, Mexico. Catena, 65, 107-117. DOI: 10.1016/j.catena.2005.11.004

Davies J.A.C., Beven K., 2015. Hysteresis and scale in catchment storage, flow, and transport. Hydrological Processes. DOI: 10.1002/hyp.10511

Detty J.M., McGuire K.J., 2010a. Topographic controls on shallow groundwater dynamics: implications of hydrologic connectivity between hillslopes and riparian zones in a till mantled catchment. Hydrological Processes, 24, 2222-2236. DOI: 10.1002/hyp.7656

Detty J.M., McGuire K.J., 2010b. Threshold changes in storm runoff generation at a till-mantled headwater catchment. Water Resources Research, 46, W07525. DOI: 10.1029/2009WR008102

Dooge, J.C.I., 1986. Looking for hydrologic laws. Water Resource Research, 22, 46-58.

Efron B., 1979. Bootstrap methods: another look at the jackknife. The Annals of Statistics, 7, 1-26.

Entin J.K., Robock A., Vinnikov K.Y., Hollinger S.E., Liu S., Namkhai A., 2000. Temporal and spatial scales of observed soil moisture variations in the extratropics. Journal of Geophysical Research, 105, 11865-11877. DOI: 10.1029/2000JD900051

Evans C., Davies T.D., 1998. Causes of concentration/discharge hysteresis and its potential as a tool for analysis of episode geochemistry. Water Resources Research, 34, 129-137.

Famiglietti J.S., Ryu D., Berg A.A., Rodell M., Jackson T.J., 2008. Field observations of soil moisture variability across scale. Water Resources Research, 44. W01423. DOI: 10.1029/2006WR005804.

Fatichi S., Katul G.G., Ivanov V.Y., Pappas C., Paschalis A., Consolo A., Kim J., Burlando P., 2015. Abiotic and biotic controls of soil moisture spatio-temporal variability and the occurrence of hysteresis. Water Resources Research. DOI: 10.1002/2014WR016102

Fovet O., Ruiz L., Hrachowitz M., Faucheux M., Gascuel-Odoux C., 2015. Hydrological hysteresis and its value for assessing process consistency in catchment conceptual models. Hydrology and Earth System Sciences, 19, 105-123. DOI: 10.5194/hess-19-105-2015

Freer J., McDonnell J., Beven K.J., Brammer D., Hooper R.P., Kendall C., 1997. Topographic controls on subsurface storm flow at the hillslope scale for two hydrologically distinct small catchments. Hydrological Processes, 11, 1347-1352. DOI: 10.1002/(SICI)1099-1085(199707)11:9<1347::AID-HYP592>3.0.CO;2-R

Frei S., Lischeid G., Fleckenstein J.H., 2010. Effects of micro-topography on surface-subsurface exchange and runoff generation in a virtual riparian wetland – A modeling study. Advances in Water Resources, 33, 1388-1401. DOI: 10.1016/j.advwatres.2010.07.006

von Freyberg J., Radny D., Gall H.E., Schirmer M., 2014. Implications of hydrologic connectivity between hillslopes and riparian zones on streamflow composition. Journal of Contaminant Hydrology, 169, 62-74. DOI: 10.1016/j.jconhyd.2014.07.005

Graham C.B., Woods R.A., McDonnell J.J., 2010. Hillslope threshold response to rainfall: 1. A field based forensic approach. Journal of Hydrology, 393, 65-76. DOI: 10.1016/j.jhydrol.2009.12.015

Grayson R., Blöschl G., 2000. Spatial processes, organisation and patterns. In Grayson R., Blöschl G. (eds). Spatial patterns in catchment hydrology: observations and modelling. Cambridge University Press, Cambridge, 2000, pp. 416. ISBN: 9780521633161.

Grayson R.B., Western A.W., 1998. Towards areal estimation of soil water content from point measurements: time and space stability. Journal of Hydrology, 207, 68-82. DOI: 10.1016/S0022-1694(98)00096-1

Guber A.K., Gish T.J., Pachepsky Y.A., van Genuchten M.T., Daughtry C.S.T., Nicholson T.J., Cady R.E., 2008. Temporal stability in soil water content patterns across agricultural fields. Catena, 73, 125-133. DOI: 10.1016/j.catena.2007.09.010

Haga H., Matsumoto Y., Matsutani J., Fujita M., Nishida K., Sakamoto Y., 2005. Flow paths, rainfall properties, and antecedent soil moisture controlling lags to peak discharge in a granitic unchanneled catchment. Water Resources Research, 41, W12410. DOI: 10.1029/2005WR004236

Haught D.R.W., van Meerveld H.J., 2011. Spatial variation in transient water table responses: differences between an upper and lower hillslope zone. Hydrological Processes, 25, 3866-3877. DOI: 10.1002/hyp.8354

Heckmann T., Schwanghart W., Phillips J.D., 2015. Graph theory – Recent developments of its application in geomorphology. Geomorphology, 243, 130-146. DOI: 10.1016/j.geomorph.2014.12.024

Herbst M., Prolingheuer N., Graf A., Huisman J.A., Weihermüller L., Vanderborght J., 2009. Characterization and understanding of bare soil respiration spatial variability at plot scale. Vadose Zone Journal, 8, 762-771. DOI: 10.2136/vzj2008.0068

Holwerda F., Scatena F.N., Bruijnzeel L.A., 2006. Throughfall in a Puerto Rican lower montane rain forest: A comparison of sampling strategies. Journal of Hydrology, 327, 592–602. DOI:10.1016/j.jhydrol.2005.12.014

Hopp L., McDonnell J.J., 2011. Examining the role of throughfall patterns on subsurface stormflow generation. Journal of Hydrology, 409, 460–471. DOI:10.1016/j.jhydrol.2011.08.044

Hornberger, G.M., Scanlon T.M., Raffensperger J.P., 2001. Modelling transport of dissolved silica in a forested headwater catchment: the effect of hydrological and chemical time scales on hysteresis in the concentration-discharge relationship. Hydrological Processes, 15, 2029-2038. DOI: 10.1002/hyp.254

Hornberger G.M., Bencala K.E., McKnight D.M., 1994. Hydrological controls on the temporal variation of dissolved organic carbon in the Snake River near Montezuma, Colorado. Biogeochemistry, 25, 147-165. DOI: 10.1007/BF00024390

Hu W., Shao M., Han F., Reichardt K., Tan J., 2010. Watershed scale temporal stability of soil water content. Geoderma, 158, 181-198. DOI: 10.1016/j.geoderma.2010.04.030

Hupet F., Vanclooster M., 2004. Sampling strategies to estimate field areal evapotranspiration fluxes with a soil water balance approach. Journal of Hydrology, 292, 262-280. DOI: 10.1016/j.jhydrol.2004.01.006

Ivanov V.Y., Fatichi S., Jenerette G.D., Espeleta J.F., Troch P.A., Huxman T.E., 2010. Hysteresis of soil moisture spatial heterogeneity and the “homogenizing” effect of vegetation. Water Resources Research, 46, W09521. DOI: 10.1029/2009WR008611

Jackson I.J., 1975. Relationships between rainfall parameters and interception by tropical rainforest. Journal of Hydrology, 24, 215-238.

Jacobs J.M., Mohanty B.P., Hsu E., Miller D., 2004. SMEX02: field scale variability, time stability and similarity of soil moisture. Remote Sensing of Environment, 92, 436-446. DOI: 10.1016/j.rse.2004.02.017

James A.L., Roulet N.T., 2007. Investigating hydrologic connectivity and its association with threshold change in runoff response in a temperate forested watershed. Hydrological Processes, 21, 3391-3408. DOI: 10.1002/hyp.6554

Jencso K.J., McGlynn B.L., Gooseff M.N., Wondzell S.M., Bencala K.E., Marshall L.A., 2009. Hydrologic connectivity between landscapes and streams: Transferring reach- and plot-scale understanding to the catchment scale. Water Resources Research, 45, W04428. DOI: 10.1029/2008WR007225

Kachanoski R.G., de Jong E., 1988. Scale dependence and the temporal persistence of spatial patterns of soil water storage. Water Resources Research, 24, 85-91. DOI: 10.1029/WR024i001p00085

Keim R.F., Skaugset A.E., Weiler M., 2005. Temporal persistence of spatial patterns in throughfall. Journal of Hydrology, 314, 263–274. DOI:10.1016/j.jhydrol.2005.03.021

Kimmins J.P., 1973. Some statistical aspects of sampling throughfall precipitation in nutrient cycling studies in British Columbian coastal forests. Ecology, 54, 1008-1019.

Klos P.Z., Chain-Guadarrama A., Link T.E., Finegan B., Vierling L.A., Chazdon R., 2014. Throughfall heterogeneity in tropical forested landscapes as a focal mechanism for deep percolation. Journal of Hydrology, 519, 2180-2188. DOI: 10.1016/j.jhydrol.2014.10.004.

Knudby C., Carrera J., 2005. On the relationship between indicators of geostatistical, flow and transport connectivity. Advances in Water Resources, 28, 405-421. DOI: 10.1016/j.advwatres.2004.09.001

Kohlpaintner M., Huber C., Weis W., Göttlein A., 2009. Spatial and temporal variability of nitrate concentration in seepage water under a mature Norway spruce [Picea abies (L.) Karst] stand before and after clear cut. Plant and Soil, 314, 285-301. DOI:10.1007/s11104-008-9729-7

Konishi S., Tani M., Kosugi Y., Takanashi S., Sahat M.M., Nik A.R., Niiyama K., Okuda T., 2006. Characteristics of spatial distribution of throughfall in a lowland tropical rainforest, Peninsular Malaysia. Forest Ecology and Management, 224, 19-25. DOI: 10.1016/j.foreco.2005.12.005

Koster R.D., Dirmeyer P.A., Guo Z., Bonan G., Chan E., Cox P., Gordon C.T., Kanae S., Kowalczyk E., Lawrence D., Liu P., Lu C.-H., Malyshev S., McAvaney B., Mitchell K., Mocko D., Oki T., Oleson K., Pitman A., Sud Y.C., Taylor C.M., Verseghy D., Vasic R., Xue Y., Yamada T., 2004. Regions of strong coupling between soil moisture and precipitation. Science, 305, 1138–1140. DOI: 10.1126/science.1100217

Kuppel S., Houspanossian J., Nosetto M.D., Jobbágy E.G., 2015. What does it take to flood the Pampas?: Lessons from a decade of strong hydrological fluctuations. Water Resources Research, 51. DOI: 10.1002/2015WR016966

Laio F., Porporato A., Ridolfi L., Rodriguez-Iturbe I., 2001. Plants in water-controlled ecosystems: active role in hydrologic processes and response to water stress: II. Probabilistic soil moisture dynamics. Advances in Water Resources, 24, 707-723. DOI: 10.1016/S0309-1708(01)00005-7

Landers M.N., Sturm T.W., 2013. Hysteresis in suspended sediment to turbidity relations due to changing particle size distributions. Water Resources Research, 49, 5487-5500. DOI: 10.1002/wrcr.20394

Lane S.N., Brookes C.J., Kirkby M.J., Holden J., 2004. A network-index-based version of TOPMODEL for use with high-resolution digital topographic data. Hydrological Processes, 18, 191-201. DOI: 10.1002/hyp.5208

Langlois J.L., Johnson D.W., Mehuys G.R., 2005. Suspended sediment dynamics associated with snowmelt runoff in a small mountain stream of Lake Tahoe (Nevada). Hydrological Processes, 19, 3569-3580. DOI: 10.1002/hyp.5844

Lawler D.M., Petts G.E., Foster I.D.L., Harper S., 2006. Turbidity dynamics during spring storm events in an urban headwater river system: The Upper Tame, West Midlands, UK. Science of the Total Environment, 360, 109-126. DOI: 10.1016/j.scitotenv.2005.08.032

Lawrence J. E., Hornberger G. M., 2007. Soil moisture variability across climate zones. Geophysical Research Letters, 34, L20402. DOI: 10.1029/2007GL031382

Levia D.F., Frost E.E., 2006. Variability of throughfall volume and solute inputs in wooded ecosystems. Progress in Physical Geography, 30, 605–632. DOI:10.1177/0309133306071145

Lexartza-Artza I., Wainwright J., 2009. Hydrological connectivity: Linking concepts with practical implications. Catena, 79, 146-152. DOI: 10.1016/j.catena.2009.07.001

Lin H., 2006. Temporal stability and soil moisture patterns and subsurface preferential flow pathways in the Shale hills catchment. Vadose Zone Journal, 5, 317-340. DOI: 10.2136/vzj2005.0058

Mano V., Nemery J., Belleudy P., Poirel A., 2009. Assessment of suspended sediment transport in four alpine watersheds (France): influence of the climatic regime. Hydrological Processes, 23, 777-792. DOI: 10.1002/hyp.7178

Mao L., Dell'Agnese A., Huincache C., Penna D., Engel M., Niedrist G., Comiti F., 2014. Bedload hysteresis in a glacier-fed mountain river. Earth Surface Processes and Landforms, 39, 964-976. DOI: 10.1002/esp.3563

Martinez G., Pachepsky Y.A., Vereecken H., Hardelauf H., Herbst M., Vanderlinden K., 2013. Modeling local control effects on the temporal stability of soil water content. Journal of Hydrology, 481, 106-118. DOI: 10.1016/j.jhydrol.2012.12.024

Martínez-Fernández J., Ceballos A., 2003. Temporal stability in a large-field experiment in Spain. Soil Science Society of America Journal, 67, 1647-1656.

McDonnell J.J., Sivapalan M., Vaché K., Dunn S., Grant G., Haggerty R., Hinz C., Hooper R., Kirchner J., Roderick M.L., Selker J., Weiler M., 2007. Moving beyond heterogeneity and process complexity: A new vision for watershed hydrology. Water Resources Research, 43, W07301. DOI: 10.1029/2006WR005467

McGlynn B.L., McDonnell J.J., Seibert J., Kendall C., 2004. Scale effects on headwater catchment runoff timing, flow sources, and groundwater-streamflow relations. Water Resources Research, 40, W07504. DOI: 10.1029/2003WR002494

McGuire K.J., McDonnell J.J., 2010. Hydrological connectivity of hillslope and streams: characteristic time scales and nonlinearities. Water Resources Research, 46, W10543. DOI: 10.1029/2010WR009341

Michaelides K., Chappell A., 2009. Connectivity as a concept for characterising hydrological behaviour. Hydrological Processes, 23, 517-522. DOI: 10.1002/hyp.7214

Mittelbach H., Seneviratne S.I., 2012. A new perspective on the spatio-temporal variability of soil moisture: temporal dynamics versus time-invariant contributions. Hydrology and Earth System Sciences, 16, 2169-2179. DOI: 10.5194/hess-16-2169-2012

Mohanty B.P., Skaggs T.H., 2001. Spatio-temporal evolution and time-stable characteristics of soil moisture within remote sensing footprints with varying soil, slope, and vegetation. Advances in Water Resources, 24, 1051-1067. DOI: 10.1016/S0309-1708(01)00034-3

Murphy J.C., Hornberger G.M., Liddle R.G., 2014. Concentration-discharge relationships in the coal mined region of the New River basin and Indian Fork sub-basin, Tennessee, USA. Hydrological Processes, 28, 718-728. DOI: 10.1002/hyp.9603

Niedzialek J.M., Ogden F.L., 2004. Numerical investigation of saturated source area behavior at the small catchment scale. Advances in Water Resources, 27, 925-936. DOI: 10.1016/j.advwatres.2004.06.005

Norbiato D., Borga M., 2008. Analysis of hysteretic behaviour of a hillslope-storage kinematic wave model for subsurface flow. Advances in Water Resources, 31, 118-131. DOI: 10.1016/j.advwatres.2007.07.001

Norbiato D., Borga M., Merz R., Blöschl G., Carton A., 2009. Controls on event runoff coefficients in the eastern Italian Alps. Journal of Hydrology, 375, 312-325. DOI: 10.1016/j.jhydrol.2009.06.044

Ocampo C.J., Sivapalan M., Oldham C., 2006. Hydrological connectivity of upland-riparian zones in agricultural catchments: implications for runoff generation and nitrate transport. Journal of Hydrology, 331, 643-658. DOI: 10.1016/j.jhydrol.2006.06.010

O'Kane J.P., 2005. Hysteresis in hydrology. Acta Geophysica Polonica, 53, 373-383.

Outram F.N., Lloyd C.E.M., Jonczyk J., Benskin C.McW.H., Grant F., Perks M.T., Deasy C., Burke S.P., Collins A.L., Freer J., Haygarth P.M., Hiscock K.M., Johnes P.J., Lovett A.L., 2014. High-frequency monitoring of nitrogen and phosphorous response in three rural catchments to the end of the 2011-2012 drought in England. Hydrology and Earth System Sciences, 18, 3429-3448. DOI: 10.5194/hess-18-3429-2014

Pachepsky Y., Guber A., Jacques D., 2005. Temporal persistence in vertical distributions of soil moisture contents. Soil Science Society of America Journal, 69, 347-352. DOI: 10.2136/sssaj2005.0347

Pan F., Pachepsky Y., Jacques D., Guber A., Hill R., 2012. Data assimilation with soil water content sensors and pedotransfer functions in soil water flow modeling. Soil Science Society of America Journal, 76, 829-844. DOI: 10.2136/sssaj2011.0090

Parajka J., Naeimi V., Blöschl G., Wagner W., Merz R., Scipal K., 2006. Assimilating scatterometer soil moisture data into conceptual hydrologic models at the regional scale. Hydrology and Earth Systems Sciences, 10, 353-368. DOI: 10.5194/hess-10-353-2006

Penna D., Borga M., Norbiato D., Dalla Fontana G., 2009. Hillslope scale soil moisture variability in a steep alpine terrain. Journal of Hydrology, 364, 311-327. DOI: 10.1016/j.jhydrol.2008.11.009

Penna D., Brocca L., Borga M., Dalla Fontana G., 2013. Soil moisture temporal stability at different depths on two alpine hillslopes during wet and dry periods. Journal of Hydrology, 477, 55-71. DOI: 10.1016/j.jhydrol.2012.10.052

Penna D., Mantese N., Hopp L., Dalla Fontana G., Borga M., 2015a. Spatio-temporal variability of piezometric response on two steep alpine hillslopes. Hydrological Processes, 29, 198-211. DOI: 10.1002/hyp.10140

Penna D., van Meerveld H.J., Oliviero O., Zuecco G., Assendelft R.S., Dalla Fontana G., Borga M., 2015b. Seasonal changes in runoff generation in a small forested mountain catchment. Hydrological Processes, 29, 2027-2042. DOI: 10.1002/hyp.10347.

Penna D., Tromp-van Meerveld H.J., Gobbi A., Borga M., Dalla Fontana G., 2011. The influence of soil moisture on threshold runoff generation processes in an alpine headwater catchment. Hydrology and Earth System Sciences, 15, 689-702. DOI: 10.5194/hess-15-689-2011

Perry M., Niemann J., 2007. Analysis and estimation of soil moisture at the catchment scale using EOFs. Journal of Hydrology, 334, 388-404. DOI: 10.1016/j.jhydrol.2006.10.014

Phillips J.D., 2003. Sources of nonlinearity and complexity in geomorphic systems. Progress in Physical Geography, 27, 1-23. DOI: 10.1191/0309133303pp340ra

Phillips J.D., Scwanghart W., Heckmann T., 2015. Graph theory in the geosciences. Earth-Science Reviews, 143, 147-160. DOI: 10.1016/j.earscirev.2015.02.002

Phillips R.W., Spence C., Pomeroy J.W., 2011. Connectivity and runoff dynamics in heterogeneous basins. Hydrological Processes, 25, 3061-3075. DOI: 10.1002/hyp.8123

Poggi-Varaldo H.M., Rinderknecht-Seijas N., 2003. A differential availability enhancement factor for the evaluation of pollutant availability in soil treatments. Acta Biotechnologica, 23, 271-280. DOI: 10.1002/abio.200390034

Porporato A., Daly E., Rodríguez-Iturbe I., 2004. Soil water balance and ecosystem response to climate change. The American Naturalist, 164, 625-632. DOI: 10.1086/424970

Pringle C., 2003. What is hydrologic connectivity and why is it ecologically important? Hydrological Processes, 17, 2685-2689. DOI: 10.1002/hyp.5145

Prowse C.W., 1984. Some thoughts on lag and hysteresis. Area, 16, 17-23.

Raat K.J., Draaijers G.P.J., Schaap M.G., Tietema A., Verstraten J.M., 2002. Spatial variability of throughfall water and chemistry and forest floor water content in a Douglas fir forest stand. Hydrology and Earth System Sciences, 6, 363-374.

Raats P.A.C., 2001. Developments in soil-water physics since the mid 1960s. Geoderma, 100, 355-387. DOI: 10.1016/S0016-7061(01)00028-3

Rinderer, van Meerveld H.J., Seibert J., 2014. Topographic controls on shallow groundwater levels in a steep, prealpine catchment: When are the TWI assumptions valid? Water Resources Research, 50, 6067-6080. DOI: 10.1002/2013WR015009

Rinderer M., van Meerveld H.J., Stähli M., Seibert J., 2015. Is groundwater response timing in a pre-alpine catchment controlled more by topography or by rainfall? Hydrological Processes, in press. DOI: 10.1002/hyp.10634

Ritter A., Regalado C.M., 2014. Roving revisited, towards an optimum throughfall sampling design. Hydrological Processes, 28, 123-133. DOI:10.1002/hyp.9561

Robinson D.A., Campbell C.S., Hopmans J.W., Hornbuckle B.K., Jones S.B., Knight R., Ogden F., Selker J., Wendroth O., 2008. Soil moisture measurements for ecological and hydrological watershed-scale observatories: A review. Vadose Zone Journal, 7, 358-389. DOI: 10.2136/vzj2007.0143

Rodriguez-Iturbe I., Porporato A., Laio F., Ridolfi L., 2001. Plants in water-controlled ecosystems: active role in hydrologic processes and response to water stress: I. Scope and general outline. Advances in Water Resources, 24, 695-705. DOI: 10.1016/S0309-1708(01)00004-5

Rodríguez-Iturbe I., Porporato, A., 2004. Ecohydrology of water-controlled ecosystems: Soil Moisture and plant dynamics. Cambridge University Press, Cambridge, pp. 450.

Romano N., Palladino M., Chirico G.B., 2011. Parameterization of a bucket model for soil-vegetation-atmosphere modeling under seasonal climatic regimes. Hydrology and Earth System Sciences, 15, 3877-3893. DOI: 10.5194/hess-15-3877-2011

Sander G.C., Zheng T., Heng P., Zhong Y., Barry D.A., 2011. Sustainable soil and water resources: modeling soil erosion and its impact on the environment. In Chan F., Marinova D. and Anderssen R.S. (eds) MODSIM2011, 19th International Congress on Modelling and Simulation. Modelling and Simulation Society of Australia and New Zealand, December 2011, pp. 1652-1658. ISBN: 978-0-9872143-1-7.

Sedea R. Di Lallo E., De Vecchi G., 1986. Carta Geologica dell'area di Valli del Pasubio – Posina – Laghi. 1:20000. Consiglio Nazionale delle Ricerche e Università di Padova, Italy.

Shachnovich Y., Berliner P.R., Bar P., 2008. Rainfall interception and spatial distribution of throughfall in a pine forest planted in an arid zone. Journal of Hydrology, 349, 168-177. DOI: 10.1016/j.jhydrol.2007.10.051

Shanley J.B., Sebestyen S.D., McDonnell J.J., McGlynn B.L., Dunne T., 2015. Water's Way at Sleepers River watershed – revisiting flow generation in a post-glacial landscape, Vermont USA. Hydrological Processes, 29, 3447–3459. DOI: 10.1002/hyp.10377

Shook K.R., Pomeroy J.W., 2011. Memory effects of depressional storage in Northern Prairie hydrology. Hydrological Processes, 25, 3890-3898. DOI: 10.1002/hyp.8381

Sidle R.C., Noguchi S., Tsuboyama Y., Laursen K., 2001. A conceptual model of preferential flow systems in forested hillslopes: evidence of self organization. Hydrological Processes, 14, 1675-1692. DOI: 10.1002/hyp.233

Sivapalan M., 2005. Pattern, process and function: elements of a unified theory of hydrology at the catchment scale. In Anderson M.G. and McDonnell J.J. (eds). Encyclopedia of Hydrological Sciences. Wiley, Chichester, 2005, pp. 193-220. DOI: 10.1002/0470848944.hsa012

Smith H.G., Dragovich D., 2009. Interpreting sediment delivery processes using suspended sediment-discharge hysteresis patterns from nested upland catchments, south-eastern Australia. Hydrological Processes, 23, 2415-2426. DOI: 10.1002/hyp.7357

Spence C., 2010. A paradigm shift in hydrology: storage thresholds across scales influence catchment runoff generation. Geography Compass, 4, 819-833. DOI: 10.1111/j.1749-8198.2010.00341.x

Staelens J., De Schrijver A., Verheyen K., Verhoest N.E.C., 2006. Spatial variability and temporal stability of throughfall water under a dominant beech (*Fagus sylvatica* L.) tree in relationship to canopy cover. Journal of Hydrology, 330, 651-662. DOI: 10.1016/j.jhydrol.2006.04.032

Starr G.C., 2005. Assessing temporal stability and spatial variability of soil water patterns with implications for precision water management. Agriculture Water Management, 72, 223-243. DOI: 10.1016/j.agwat.2004.09.020

Stieglitz M., Shaman J., McNamara J., Engel V., Shanley J., Kling G.W., 2003. An approach to understanding hydrologic connectivity on the hillslope and the implications for nutrient transport. Global Biogeochemical Cycles, 17, 16.1-16.15. DOI: 10.1029/2003GB002041

Subehi L., Fukushima T., Onda Y., Mizugaki S., Gomi T., Kosugi K., Hiramatsu S., Kitahara H., Kuraji K., Terajima T., 2010. Analysis of stream water temperature changes during rainfall events in forested watersheds. Limnology, 11, 115-124. DOI: 10.1007/s10201-009-0296-2

Tetzlaff D., McDonnell J.J., Uhlenbrook S., McGuire K.J., Bogaart P.W., Naef F., Baird A.J., Dunn S.M., Soulsby C., 2008. Conceptualizing catchment processes: simply too complex? Hydrological Processes, 22, 1727-1730. DOI: 10.1002/hyp.7069

Tetzlaff D., Soulsby C., Bacon P.J., Youngson A.F., Gibbins C., Malcolm I.A., 2007. Connectivity between landscapes and riverscapes – a unifying theme in integrating hydrology and ecology in catchment science? Hydrological Processes, 21, 1385-1389. DOI: 10.1002/hyp.6701

Teuling A. J., Troch P. A., 2005. Improved understanding of soil moisture variability dynamics. Geophysical Research Letters, 32, L05404. DOI: 10.1029/2004GL021935

Tromp-van Meerveld H.J., McDonnell J.J., 2006a. Threshold relations in subsurface stormflow: 1. A 147-storm analysis of the Panola hillslope. Water Resources Research, 42, W02410. DOI: 10.1029/2004WR003778

Tromp-van Meerveld H.J., McDonnell J.J., 2006b. Threshold relations in subsurface stormflow: 2. The fill and spill hypothesis. Water Resources Research, 42, W02411. DOI: 10.1029/2004WR003800

Tromp-van Meerveld H.J., McDonnell J.J., 2006c. On the interrelations between topography, soil depth, soil moisture, transpiration rates and species distribution at the hillslope scale. Advances in Water Resources, 29, 293-310. DOI: 10.1016/j.advwatres.2005.02.016

Tromp-van Meerveld I., McDonnell J.J., 2005. Comment to “Spatial correlation of soil moisture in small catchments and its relationship to dominant spatial hydrological processes, Journal of Hydrology 286: 113-134”. Journal of Hydrology, 303, 307-312. DOI: 10.1016/j.jhydrol.2004.09.002

Turnbull L., Wainwright J., Brazier R.E., 2008. A conceptual framework for understanding semi-arid land degradation: ecohydrological interactions across multiple-space and time scales. Ecohydrology, 1, 23-24. DOI: 10.1002/eco.4

Uchida T., Kosugi K., Mizuyama T., 2001. Effects of pipeflow on hydrological process and its relation to landslide: a review of pipeflow studies in forested headwater catchments. Hydrological Processes, 15, 2151-2174. DOI: 10.1002/hyp.281

Vachaud G., Passerat De Silans A., Balabanis P., Vauclin M., 1985. Temporal stability of spatially measured soil water probability density function. Soil Science Society of America Journal, 49(4), 822-828.

Vanderlinden K., Vereecken H., Hardelauf H., Herbst M., Martínez G., Cosh M.H., Pachepsky Y.A., 2012. Temporal stability of soil water contents: A review of data and analyses. Vadose Zone Journal, 11. DOI: 10.2136/vzj2011.0178

Vereecken H., Huisman J. A., Bogena H., Vanderborght J., Vrugt J. A., Hopmans J. W., 2008. On the value of soil moisture measurements in vadose zone hydrology: A review. Water Resources Research, 44. DOI: 10.1029/2008WR006829

Vidon P.G.F., Hill A.R., 2004. Landscape controls on nitrate removal in stream riparian zones. Water Resources Research, 40, W03201. DOI: 10.1029/2003WR002473.

Visintin A., 2006. Quasilinear parabolic P.D.E.s with discontinuous hysteresis. Annali di Matematica, 185, 487-519. DOI: 10.1007/s10231-005-0164-6

Wainwright J., Bracken L.J., 2011. Runoff generation, overland flow and erosion on hillslopes. In Thomas D.S.G. (eds). Arid Zone Geomorphology, Chichester. DOI: 10.1002/9780470710777.ch11

Wenninger J., Uhlenbrook S., Tilch N., Leibundgut C., 2004. Experimental evidence of fast groundwater responses in a hillslope/floodplain area in the Black Forest Mountains, Germany. Hydrological Processes, 18, 3305-3322. DOI: 10.1002/hyp.5686

Western A.W., Blöschl G., Grayson R.B., 2001. Toward capturing hydrologically significant connectivity in spatial patterns. Water Resources Research, 37, 83-97.

Western A.W., Zhou S.-L., Grayson R.B., McMahon T.A., Blöschl G., Wilson D.J., 2005. Reply to comment by Tromp van Meerveld and McDonnell on Spatial correlation of soil moisture in small catchments and its relationship to dominant spatial hydrological processes. Journal of Hydrology, 303, 313-315. DOI: 10.1016/j.jhydrol.2004.09.001

Wetzel K., 2003. Runoff production processes in small alpine catchments within the unconsolidated Pleistocene sediments of the Lainbach area (Upper Bavaria). Hydrological Processes, 17, 2463-2483. DOI: 10.1002/hyp.1254

Wilby R.L., Johnson M.F., Toone J.A., 2014. Nocturnal river water temperatures: spatial and temporal variations. Science of the Total Environment, 482-483, 157-173. DOI: 10.1016/j.scitotenv.2014.02.123

Zhang Q., Manzoni S., Katul G., Porporato A., Yang D., 2014. The hysteretic evapotranspiration-vapor pressure deficit relation. Journal of Geophysical Research: Biogeosciences, 119, 125-140. DOI: 10.1002/2013JG002484

Zhao Y., Peth S., Wang X.Y., Lin H., Horn R., 2010. Controls of surface soil moisture spatial patterns and their temporal stability in a semi-arid steppe. Hydrological Processes, 24, 2507-2519. DOI: 10.1002/hyp.7665

Zheng H., Wang Q., Zhu X., Li Y., Yu G., 2014. Hysteresis responses of evapotranspiration to meteorological factors at a diel timescale: patterns and causes. PLoS ONE, 9(6). DOI: 10.1371/journal.pone.0098857

Zimmermann A., Germer S., Neill C., Krusche A.V., Elsenbeer H., 2008. Spatio-temporal patterns of throughfall and solute deposition in an open tropical rain forest. Journal of Hydrology, 360, 87-102. DOI: 10.1016/j.jhydrol.2008.07.028

Zimmermann B., Zimmermann A., Lark R.M., Elsenbeer H., 2010. Sampling procedures for throughfall monitoring: A simulation study. Water Resources Research, 46. DOI:10.1029/2009WR007776

Zuecco G., Penna D., Borga M., van Meerveld H.J., 2015. A versatile index to characterise hysteresis between hydrological variables at the runoff event timescale. Hydrological Processes, in press. DOI: 10.1002/hyp.10681

List of publications

Penna D., Stenni B., Šanda M., Wrede S., Bogaard T.A., Michelini M., Fischer B.M.C., Gobbi A., Mantese N., Zuecco G., Borga M., Bonazza M., Sobotková M., Čejková B., Wassenaar L.I., 2012. Technical Note: Evaluation of between-sample memory effects in the analysis of δ^2H and δ^{18}O water samples measured by laser spectroscopes. Hydrology and Earth System Sciences, 16, 3925-3933. DOI: 10.5194/hess-16-3925-2012

Penna D., Oliviero O., Assendelft R., Zuecco G., van Meerveld I., Anfodillo T., Carraro V., Borga M., Dalla Fontana G., 2013. Tracing the water sources of trees and streams: isotopic analysis in a small pre-alpine catchment. Procedia Environmental Sciences, 19, 106-112. DOI: 10.1016/j.proenv.2013.06.012

Zuecco G., Borga M., Penna D., Canone D., Previati M., Ferraris S., 2013. Towards improved understanding of land use effect on soil moisture variability: analysis and modeling at the plot scale. Procedia Environmental Sciences, 19, 456-464. DOI: 10.1016/j.proenv.2013.06.052

Zuecco G., Penna D., van Meerveld H.J., Hopp L., Dalla Fontana G., Borga M., 2014. Comparison of two different types of throughfall collectors. Die Bodenkultur, 65 (3-4), 51-56.

Brocca L., Massari C., Ciabatta L., Moramarco T., Penna D., Zuecco G., Pianezzola L., Borga M., Matgen P., Martínez-Fernández J., 2015. Rainfall estimation from in situ soil moisture observations at several sites in Europe: an evaluation of the SM2RAIN algorithm. Journal of Hydrology and Hydromechanics, 63, 201-209. DOI: 10.1515/johh-2015-0016

Penna D., van Meerveld H.J., Oliviero O., Zuecco G., Assendelft R.S., Dalla Fontana G., Borga M., 2015. Seasonal changes in runoff generation in a small forested mountain catchment. Hydrological Processes, 29, 2027-2042. DOI: 10.1002/hyp.10347

Carturan L., Zuecco G., Seppi R., Zanoner T., Borga M., Carton A., Dalla Fontana G.. Catchment-scale permafrost mapping using spring water characteristics. Permafrost and Periglacial Processes, in press. DOI: 10.1002/ppp.1875

Zuecco G., Penna D., Borga M., van Meerveld H.J.. A versatile index to characterise hysteresis between hydrological variables at the runoff event timescale. Hydrological Processes, in press. DOI: 10.1002/hyp.10681

Carturan L., Baroni C., Brunetti M., Carton A., Dalla Fontana G., Salvatore M.C., Zanoner T., Zuecco G.. Analysis of the mass balance time series of glaciers in the Italian Alps. The Cryosphere, in review.

Penna D., van Meerveld H.J., Zuecco G., Dalla Fontana G., Borga M.. Hydrological response of an Alpine catchment to rainfall and snowmelt events. Journal of Hydrology, in review.

Author contributions and acknowledgements

I am responsible for data analysis, presentation and discussion of the results in this thesis.
I was responsible for collecting data (i.e., precipitation, soil moisture, groundwater, isotopic and electrical conductivity) in Bridge Creek and Ressi catchment from 2012 to 2015, together with Daniele Penna (2012-2013), Nicola Mantese (2012), Omar Oliviero (2012-2014) and Luisa Pianezzola (2013-2015). Furthermore, I collaborated with Luca Carturan for collecting hydrometric, isotopic and electrical conductivity data in Alta Val de La Mare catchment from 2012 to 2015.

Stefano Ferraris (Politecnico di Torino, Italy), Davide Canone (Politecnico di Torino, Italy) and Maurizio Previati (Politecnico di Torino, Italy) are thanked for sharing soil moisture data shown in Section 4 of the thesis and providing feedbacks on data analysis and modeling.

Daniele Penna, Omar Oliviero and I prepared the throughfall and soil moisture sampling design on a hillslope of the Ressi catchment in 2013. Omar Oliviero, Luisa Pianezzola and the students, Federica Basso, Matteo Catanese, Damiano Fioretto, Alberto Piccolotto and Marco Surian are thanked for helping during data collection. Daniele Penna, Ilja van Meerveld (University of Zurich, Switzerland) and Luisa Hopp (University of Bayreuth, Germany) are thanked for providing comments on data analysis.

Alberto Gobbi, Nicola Mantese and Daniele Penna are acknowledged for collecting data in Bridge Creek and Larch Creek catchment in 2008, 2009 and 2011 (data used for the analysis of subsurface connectivity in Section 7 of the thesis). Michael Rinderer (Duke University, North Carolina, USA) is thanked for sharing piezometric and streamflow data collected in three catchments in Alptal (Switzerland) during his PhD and for the ongoing collaboration on the comparison study between the Italian and the Swiss datasets.

Nicola Mantese and Daniele Penna had the initial idea of developing a hysteresis index for hydrological variables. The first application of a preliminary version of the index can be found in Nicola Mantese's PhD thesis. Afterwards, I developed the index throughout different stages, implemented the MATLAB scripts and tested the index with synthetic and field data under the supervision of Ilja van Meerveld and Daniele Penna. I also thank Marc Vis (University of Zurich, Switzerland) for converting the MATLAB scripts into a user-friendly application written in Java.

The Agency for Environmental Protection (ARPAV) of Veneto Region is acknowledged for sharing the meteorological data used for Bridge Creek and Ressi catchment.

The Hydrology and Climate group (H2K) of the Department of Geography, University of Zurich (Switzerland) is warmly thanked for hosting me as a visiting PhD student from December 2014 to May 2015.

Ilja van Meerveld, Marco Borga and Daniele Penna are acknowledged for their valuable feedbacks during the PhD.